

Two-photon Photoemission of Organic Semiconductor Molecules on Ag(111)

Aram Yang

Ph.D. Thesis

Department of Chemistry
University of California, Berkeley

and

Chemical Sciences Division
Ernest Orlando Lawrence Berkeley National Laboratory
University of California
Berkeley, CA 94720

May 2008

This work was supported by the Director, Office of Science, Office of Basic Energy Sciences, Chemical Sciences Division, of the U.S. Department of Energy under Contract No. DE-AC02-05CH11231.

Two-photon Photoemission of Organic Semiconductor Molecules on Ag(111)

Copyright © 2008

by

Aram Yang

Abstract

Two-photon Photoemission of Organic Semiconductor Molecules on Ag(111)

by

Aram Yang

Doctor of Philosophy in Chemistry

University of California, Berkeley

Professor Charles B. Harris, Chair

Angle- and time-resolved two-photon photoemission (2PPE) was used to study systems of organic semiconductors on Ag(111). The 2PPE studies focused on electronic behavior specific to interfaces and ultrathin films. Electron time dynamics and band dispersions were characterized for ultrathin films of a prototypical n-type planar aromatic hydrocarbon, PTCDA, and representatives from a family of p-type oligothiophenes.

In PTCDA, electronic behavior was correlated with film morphology and growth modes. Within a few monolayers of the interface, image potential states and a LUMO+1 state were detected. The degree to which the LUMO+1 state exhibited a band mass less than a free electron mass depended on the crystallinity of the layer. Similarly, image potential states were measured to have free electron-like effective masses on ordered surfaces, and the effective masses increased with disorder within the thin film. Electron lifetimes were correlated with film growth modes, such that the lifetimes of electrons excited into systems created by layer-by-layer, amorphous film growth increased by orders of magnitude by only a few monolayers from the surface. Conversely, the decay dynamics of electrons in Stranski-Krastanov systems were limited by interaction with the exposed wetting layer, which limited the barrier to decay back into the metal.

Oligothiophenes including monothiophene, quaterthiophene, and sexithiophene were deposited on Ag(111), and their electronic energy levels and effective masses were studied as a function of oligothiophene length. The energy gap between HOMO and LUMO decreased with increasing chain length, but effective mass was found to depend on domains

from high- or low-temperature growth conditions rather than chain length. In addition, the geometry of the molecule on the surface, e.g., tilted or planar, substantially affected the electronic structure.

Professor Charles B. Harris
Dissertation Committee Chair

*“Cui dono lepidum novum libellum
arida modo pumice expolitum?
Nancy, tibi: namque tu solebas
meas esse aliquid putare nugas.”*

—CATULLUS

Contents

List of Figures	iv
List of Tables	vii
1 Introduction	1
1.1 Overview	1
1.2 Two-photon Photoemission	2
1.3 Electronic structure	6
1.3.1 Image potential states	6
1.3.2 Excitons	7
1.4 Molecular thin films at interfaces	9
2 Experimental	11
2.1 Ultra-high vacuum chamber	13
2.2 Detection electronics	16
2.3 Lasers	18
2.4 Materials	19
3 PTCDA	20
3.1 Background	20
3.2 Materials	22
3.2.1 Dosing calibration	22
3.2.2 Growth modes	23
3.2.3 Morphology control	24
3.3 Workfunction and Vacuum Level Shifts	26
3.4 Effective Masses	36
3.5 Lifetimes	36
3.6 Implications for Charge Transport Measurements	41
3.7 Future work	44
3.8 Conclusion	45

4	Oligothiophenes	46
4.1	Overview	46
4.2	Monothiophene	48
4.3	Quaterthiophene	52
4.3.1	Material properties	52
4.3.2	LEED	62
4.3.3	Laser instability	64
4.3.4	Short lifetimes	64
4.4	Sexithiophene	67
4.4.1	Dosing survey	67
4.4.2	LEED	69
4.4.3	2PPE measurements	70
4.5	Current status	75
4.5.1	Experimental difficulties	75
4.5.2	Trends and future work	75
5	Conclusions	77
	Bibliography	79

List of Figures

1.1	2PPE	3
1.2	The appropriate photon energy to subtract for determining binding energies can be determined with a wavelength survey.	4
1.3	Angle-Resolved 2PPE	5
1.4	A photoelectron outside a metal surface can become bound to the surface via its self-induced polarization. The system of electron and its image charge is isomorphic with the hydrogen atom.	7
1.5	The ionization energy and electron affinity of a molecule in the gas phase will relax due to lattice polarizations in a crystal and become the valence and conduction bands, resp. An exciton exhibits additional relaxation energy from the bound electron-hole pair.	8
1.6	Exciton spatial extents.	9
2.1	Experimental set-up.	12
3.1	Angle-Resolved 2PPE	21
3.2	LEED	23
3.3	PTCDA exhibits different growth modes, depending on substrate temperature. At low temperature, layer-by-layer (± 1 ML) growth dominates, while higher substrate temperatures leads to Stranski-Krastanov growth. . .	25
3.4	dosing	26
3.5	2PPE spectrum.	27
3.6	Vacuum level shifts	28
3.7	Lambda survey	30
3.8	A stackplot comparison of 2PPE data for 1–4 ML of different PTCDA morphologies. The data have been normalized so that the maximum of each spectrum is unity. The $n = 1$ IPS is quickly extinguished in layer-by-layer growth at low T_D , and the LUMO+1 in crystalline layers is well-defined. The temperatures given are for the dosing temperatures, and data were collected at a substrate temperature of 140 K.	32
3.9	Room temperature vs. 140 K spectra.	33

3.10	Spectra of 3 ML, $T_D = 300$ K, and a visible photon energy of 1.94 eV. By lowering the photon energy to avoid photoemitting the LUMO+1 peak, electronic structure with a molecular orbital basis is visible.	34
3.11	Effective mass	35
3.12	Each vertical line in the contour plot is a time slice corresponding to a 2PPE spectrum at a given time delay. The time delay is plotted with positive time indicating the probe pulse ($h\nu_2$) at a positive delay with respect to the pump pulse ($h\nu_1$). For 2 ML annealed at $T_D = 450$ K, the LUMO+1 is best fit to a Lorentzian (b) with a full width at half maximum of 90 meV, which can be converted to a lifetime or scattering time of 46 fs. The fit is better as a Lorentzian than a Gaussian lineshape (c), which suggests that the lifetime broadening is homogeneous.	37
3.13	Low kinetic energy fit	40
3.14	The contour plots compare the time dynamics of 3 ML of PTCDA with $T_D = 450$ K. The bottom figure was obtained at 0° , and the top was obtained at 24° . The similarity in dynamics for both the LUMO+1 and the higher energy $n = 1$ IPS indicate that intraband relaxation is not observable at this time scale.	43
3.15	At 320 K, the LUMO+1 of a layer dosed at 450 K has a FWHM of 290 meV.	44
4.1	Energy level diagram of values for different thiophene interfaces. Energies are in eV and referenced to the Fermi level, $E - E_f$	48
4.2	TPD spectra of 1 ML thiophene. The saturated monolayer was dosed at 133 K, while the planar monolayer was dosed at 160 K.	49
4.3	(a) LEED of the tilted monolayer of monothiophene, at 22.1 eV, and (b) of the planar monolayer, at 16.2 eV.	50
4.4	(a) 2PPE spectrum of 1 ML thiophene in its dense phase. The planar phase (b) exhibits what are probably the $n = 1$ and $n = 2$ IPS and two molecular-orbital based states.	51
4.5	The conformer of quaterthiophene that was dosed on the surface is unclear.	53
4.6	Auger dosing survey of quaterthiophene. Each dosing increment was 10 seconds of quaterthiophene, with the substrate held at room temperature and the Knudsen cell at 150°C	54
4.7	(a) 2PPE stackplot of 10 second increments of 4T, with an effusion cell temperature of 150°C and substrate dosing temperature of 300 K. (b) Comparison of 10 second increments of 4T, with same conditions as above except a substrate dosing temperature of 400 K. After 40 seconds or so, which is about 1 ML, no more 4T should stick to the surface. The spectra were collected at room temperature.	56
4.8	Dispersion of layer with $T_{eff} = 160^\circ\text{C}$, 30 seconds of 4T.	57
4.9	Dispersions of a layer grown at $T_{Ag} = 210$ K and at $T_{Ag} = 400$ K.	58

4.10	In a comparison of uv-uv and uv-vis spectra, peak A has no analogue in the uv-uv spectrum that might result from a uv-probe if it were vis-probed in the uv-vis spectra. This suggests that peak A is always uv-probed. The visible photon energy was 1.96 eV.	59
4.11	Comparison of 2PPE spectra for different polymorphs; all spectra were collected at 140 K.	59
4.12	Dispersion of 150 °C layer, 30 seconds (top) and 630 seconds (bulk). The dashed line is a guide to the eye indicating the position of the localized shoulder.	61
4.13	LEED, 4T, 12.0 eV, $T_D = 300$ K.	62
4.14	LEED, 4T, 12.2 eV, $T_D = 210$ K.	63
4.15	LEED, 4T, 12.4 eV, $T_D = 400$ K.	63
4.16	Comparison of 0, 12, and 20 deg 2PPE scans, with data fits for the 20 deg spectrum, for the morphology of a room temperature-grown layer.	64
4.17	Fit of 2PPE spectrum at 0 degrees (top) and 20 degrees (bottom). The shoulder marked with (*) is consistently visible at high angles.	65
4.18	Over tens of minutes, exposure to laser light causes changes in the electronic structure of the layer.	66
4.19	Contour plot of 1 ML quaterthiophene, at zero degrees.	67
4.20	α -6T.	67
4.21	Auger peaks for Sulfur and Ag in a sexithiophene dosing survey with 10 second time steps, an effusion cell temperature of 270 °C, and at room temperature.	68
4.22	A dosing survey with 10 second increments; Ag crystal at 300 K; and effusion cell = 270 °C. The visible wavelength was 611 nm.	69
4.23	A comparison of the 20 second and 50 second films, where the elapsed time between the two was about 12 minutes.	70
4.24	LEED of 3–5 ML sexithiophene, at 8.6 eV (top) and 18.2 eV (bottom). . . .	71
4.25	Dispersion of a bulk (300 second) layer, with a wavelength of 611 nm. The effective mass of the uv-probed peak is $1.1 m_e$	72
4.26	200 seconds of 6T, with clear domain-separated energies.	73
4.27	Dispersion of 80 sec 6T (a), and of 80 sec 6T (b) grown on top of a polymerized surface.	74
4.28	Observing static and dynamic localization due to side chains would be an interesting project.	75

List of Tables

3.1	The evolution of the unoccupied states E_{VB} as more PTCDA is dosed. The rise in E_{VB} occurs more rapidly for low T_D amorphous layers than for high T_D crystalline layers.	29
3.2	Rise and decay constants for the LUMO+1 in a Stranski-Krastanov morphology were dominated by interaction with the wetting layer and stayed constant, but the decay constants for amorphous layer-by-layer growth increased dramatically. For all coverages, one monolayer dynamics could not be fit reliably due to weak dynamical signal.	38
3.3	The lifetimes of the low kinetic energy manifold at $T_D = 200$ K exhibit bi-exponential behavior from 4 – 8 ML.	39
4.1	Effective masses in units of m_e for quaterthiophene.	62

Acknowledgments

I hope to convey at least a small sense of my tremendous gratitude toward those who have helped, supported, prodded, and/or pulled me along my six year journey.

I wish to thank my adviser, Professor Charles Harris, for maintaining a challenging and stimulating environment in his group, where I had the freedom to grow as an independent scientist. Meanwhile, Vijaya Narasimhan provided crucial administrative support (and occasional sage advice) to maintain the group's daily operation.

I joined the Harris group because of the supportive and collegial atmosphere the graduate students provided. On the surface side, Paul Szymanski was an excellent sounding board, and his attention to detail in running experiments remains a model of how to do things properly. While providing training and mentorship, Sean Garrett-Roe also willingly answered my many questions, no matter how trivial. Steve Shipman, a creative and entertaining comrade-in-arms in our fight for data, motivated me with his infectious enthusiasm for science. The aforementioned alumni have greatly influenced my perspective on research and problem-solving, especially in the context of the Harris group. Matt Strader, my fellow sixth-year, stayed grounded no matter how dire the events in lab. The addition of James Johns to the surface side provided much-needed energy both in the abstract and caffeinated senses. Eric Muller's mechanical aptitude has made noticeable improvements to our experiment, while his barrage of questions have forced me to re-think assumptions I have long taken for granted.

The liquid side has also contributed much to my experience here at Berkeley. Christine Payne, Jason van Zanten, Jennifer Shanoski, and Libby Glascoe all welcomed me into the group. I interacted with Christine and Jason only briefly, but Christine's composure and Jason's basketball coaching skills made different but positive impressions. Jennifer provided expert tips in motorcycle maintenance, while Libby's friendliness (and, later on, her thesis advice) were duly appreciated. The arrivals of Karma Sawyer, James Cahoon, and Jacob Schlegel, followed by Matt Zoerb and Dan Lucas, have helped foster the nurturing and friendly atmosphere that colors my impression of my six years. Karma was an entertaining officemate for the past year or two, and James is certain to be a rising star in academia. Jacob is easily the most talented amateur chef I know, and I have enjoyed discussing epi-

curean topics with him. Dan is remembered, and mourned, for his genuine enthusiasm for science. I am grateful for countless trips to coffee shops and to the Bear's Lair with the group members above, not to mention the daily and friendly interactions in lab.

I would like to thank Bryan Jackson, our softball team *Team Terror*, and the other graduate students who have reminded me on a daily basis that this chemistry department was the right choice for me. The technical support of the machine, vacuum, glass, and electrical shops has been instrumental to the functioning of the Harris group, with a special note of appreciation for the electrical shop's Henry Chan and Steve Hoagland.

Finally, I thank Halla, Liz, and my parents for their support. Our irrationally exuberant dog Sammy provided, and occasionally forced, thesis breaks even at odd hours of the night. Most importantly, I thank my wife Nancy, who, for the last five years, has consistently sustained me through my lows and celebrated my highs.

This work was supported by the Director, Office of Energy Research, Office of Basic Energy Sciences, Chemical Sciences Division of the U.S. Department of Energy, under Contract No. DE-AC02-05CH11231. The author acknowledges the National Science Foundation support for specialized equipment used in the experiments described herein.

Chapter 1

Introduction

1.1 Overview

The surging interest in devices manipulated or assembled on a molecular length scale results from three key scientific developments of the twentieth century. Fifty years after its invention, the transistor permeates the trappings of modern society, and envisioning life without devices like computers increasingly requires a creative imagination or elephantine memory. The driving force of related industrial research is currently to increase the density of transistors on a chip, thereby improving computing power. Secondly, in the early 1970s [1, 2], scientists discovered that air pollution from human activity was contributing to global warming, with uncertain and probably dire consequences. The burning of fossil fuels for energy comprises a major component of global warming, and the need for sustainable energy sources has entered the collective consciousness of the general public. Finally, and with a more nebulous future, the realization that materials on nanometer length scales have different physical properties than bulk materials has inspired research directions on the nanoscale either for creating molecular electronic devices or engineering solutions to the renewable energy problem [3]. The possibility also exists that research in nanotechnology will yield new inventions that affect our society in ways that we cannot yet imagine.

By no means does this dissertation claim to solve these issues. The research enclosed in these pages has focused on a fundamental element of an interface of dissimilar materials: charge injection at an interface between a metal and a molecular layer. While my

research has attempted to place interfacial electron transfer in the same context as thin-film transistors, plastic solar cells, and quantum dots (or nano-islands), the category is much more general and has generated fruitful research for this group for over a decade. Although bulk electronic properties of molecular crystals and liquids are generally well-understood, electron behavior is inherently different and merits its own investigation in the reduced dimensionality of interfaces [4], where rotational barriers relative to crystals and diffusional motion relative to liquids are decreased.

Investigating electronic processes at these interfaces requires a technique capable of dynamic and energetic resolution. Most of my research was conducted with two-photon photoemission (2PPE), a pump-probe spectroscopy that measures both initially occupied and unoccupied electronic states over femtosecond timescales. The addition of angular resolution to 2PPE enables the study of electronic effective masses. Two-photon photoemission was applied to two archetypal molecular systems: ultrathin films of 3,4,9,10-perylene tetracarboxylic dianhydride (PTCDA), which is an organic n-type semiconductor, and layers of p-type thiophenes of varying oligomer lengths.

1.2 Two-photon Photoemission

Two-photon photo-emission is a pump-probe spectroscopy capable of obtaining dynamical information about excited states, and it offers the advantage over single photon photoemission of simultaneously probing initially occupied states and unoccupied states [5]. In a 2PPE experiment, an electron is injected from below the Fermi level of a metal into an intermediate state with a pump laser pulse ($h\nu_1$) which has less energy than the workfunction (Φ), and a second probe pulse ($h\nu_2$) photoemits the electron from the intermediate state (figure 1.1). The kinetic energy E_{kin} is measured, from which a binding energy relative to the vacuum level is determined by subtracting the probe photon energy. Our experimental set-up, described in further detail in the next chapter, is a two-color experiment, in which one color ($h\nu_1$) is doubled to create the second ($h\nu_2$). Ambiguity about which color photoemitted an electron is resolved by taking a wavelength survey. Changing $h\nu_1$ by a known amount of energy $\Delta h\nu$ changes $h\nu_2$ by twice that amount, $2\Delta h\nu$. The kinetic energy of

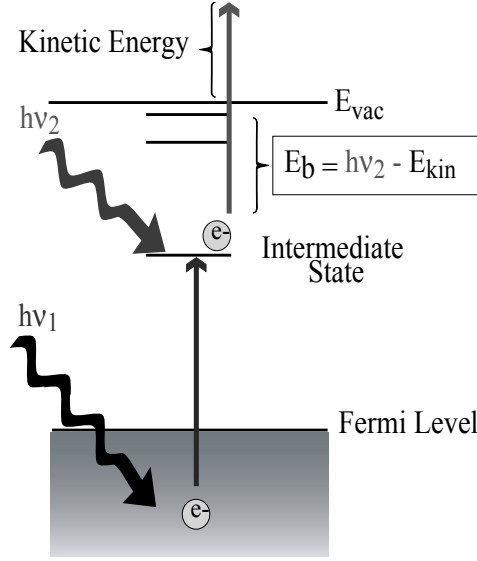


Figure 1.1: A pump laser pulse, $h\nu_1$, excites an electron from below the Fermi level into an intermediate state. A second probe laser pulse, $h\nu_2$, photo-emits the electron.

an intermediate state photoemitted by $h\nu_1$ will shift by $\Delta h\nu$, and a state photoemitted by $h\nu_2$ shifts by $2\Delta h\nu$. Similar arguments can be made for initially occupied states, which are photoemitted through a coherent two-photon process 1.2.

Device efficiency depends critically on charge injection and time dynamics. Charge injection, in turn, reflects the interfacial electronic structure, while the time dynamics are determined by the interaction of the injected charge with the molecular layer and/or the substrate. Generally, surface dynamics occur on femtosecond time scales. For these reasons, 2PPE is a useful technique for studying charges at an interface.

On the femtosecond time scale, relevant processes in the context of semiconductors that have been studied with 2PPE include quantum well formation [6], nuclear motion [7, 8], intraband scattering [9], and electron localization [10]. McNeill et al. [6] reported the transition of an excited electron at the xenon/Ag(111) interface from populating an image potential state (IPS) to populating a quantum well derived from the bulk xenon conduction band. Lifetimes of electrons at the interface were directly affected by the spatial distribution of the image potential states and quantum wells. In the context of xenon as a wide gap semiconductor, McNeill et al. [11] also studied the dispersion (k_z) of image potential states at the Xe/Ag(111) interface with increasing layer thickness. Ge et al. [7] observed that

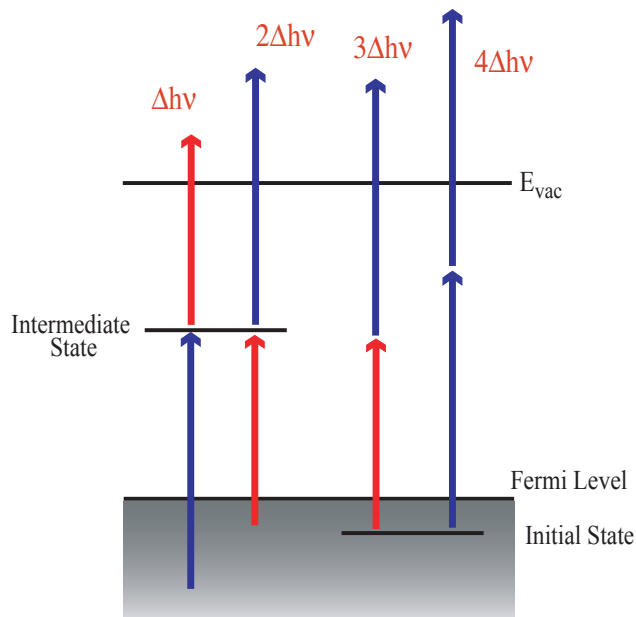


Figure 1.2: The appropriate photon energy to subtract for determining binding energies can be determined with a wavelength survey.

small polarons at alkane/Ag(111) interfaces localize within a few hundred femtoseconds, and they modelled the energy dependence of the self-trapping rate with electron transfer theory. Gaffney et al. [12] reported hybridized molecular/IPS states of naphthalene on Ag(111) and presented a systematic study of binding energy and lifetime trends with increasing coverages of linear acenes [10, 12]. A localized state in a benzene multilayer was attributed to structural disorder.

In contrast, a localized LUMO state in the parallel-band structure of a methanethiolate/Ag(111) interface [13] undergoes an abrupt change to an extremely dispersive state ($0.5 m_e$) as the layer undergoes a phase transition. Dutton et al. [14] measured the dispersions and lifetimes of C_{60} molecular states and substrate-derived IPS, with corroboration by Shipman et al. [15]. Additionally, Shipman et al. used calculations of orbital orientations with respect to nearest neighbor C_{60} molecules to predict effective masses of molecular states.

Another benefit of 2PPE is the ability to measure the effective mass of a surface electron, by taking spectra at different angles. The momentum of a photo-electron which reaches the detector is a sum of momentum in the surface normal direction (k_{\perp}), and of

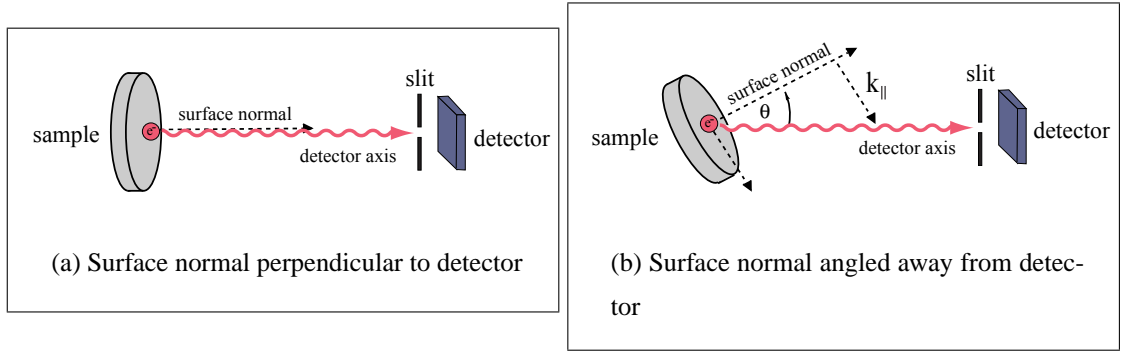


Figure 1.3: (a) The substrate and detector are parallel, and a photo-electron travels in the direction of the surface normal to reach the detector. (b) The substrate is at an angle, so that only photo-electrons with a parallel momentum component (k_{\parallel}) are capable of hitting the detector.

momentum parallel to the surface (k_{\parallel}). Any photo-electron which lacks the precise momentum to hit the detector will travel outside the detector's limited acceptance range. If the surface normal is pointed exactly toward the detector (Figure 1.3(a)), only photo-electrons travelling along the surface normal are detected. When the substrate is angled away from the detector, the surface normal is no longer perpendicular to the detector, and only a photo-electron with an additional, parallel momentum component reaches the detector (Figure 1.3(b)). The magnitude of the parallel momentum ($\hbar k_{\parallel}$) determines the band dispersion of the electronic structure along the surface according to the relation:

$$k_{\parallel} = \sqrt{\frac{2m_e E_{\text{kin}}}{\hbar^2}} \sin \theta, \quad (1.1)$$

where E_{kin} is measured with 2PPE, m_e is the free electron mass, and θ , which is controlled in the experiment, is the angle of the detector away from the surface normal. Near the $\bar{\Gamma}$ point—the center of the surface Brillouin zone—the energy as a function of k_{\parallel} can be approximated by the nearly free electron model and therefore a parabolic band dispersion. The dispersion is fit to a function composed of the binding energy at zero parallel momentum (E_b) and a kinetic energy term quadratic in k_{\parallel} :

$$E_{\text{kin}} = E_b + \frac{(\hbar k_{\parallel})^2}{2m^*}, \quad (1.2)$$

where m^* is an effective electron mass. Nearly free (delocalized within the plane) electronic states have values of $|m^*| \approx m_e$, while spatially-localized electronic states, which appear

non-dispersive, have values of $|m^*| \gg m_e$. For a localized state, k_{\parallel} is not conserved and is not a good quantum number. In the case of small k_{\parallel} , the effective mass of a delocalized state can be used to estimate the transfer integral (β). For the (approximately) rectangular lattice of PTCDA on Ag(111), the surface band structure can be modelled with a cosine band and has a minimum at the $\bar{\Gamma}$ point. The transfer integral (β) can then be estimated by:

$$\beta = \frac{\hbar^2}{4d^2m^*}, \quad (1.3)$$

where d is the nearest-neighbor distance.

1.3 Electronic structure

The excited states at an interface between a molecular layer and Ag(111) can be divided into two categories. The first comprises photoelectrons originating from the metal and includes the majority of 2PPE electronic measurements at the interface. Examples include image potential states, metal-to-molecule anionic charge transfer states, and surface states such as the Shockley state. The other category is constituted of molecular excitations, excitons. Excitons are independent of the substrate and in a thin film are generated mainly in the top-most layers. Compared to an excitation from a metal, for which a flat density of states can be assumed, an exciton should exhibit resonant 2PPE peak intensities highly dependent on pump photon energy.

1.3.1 Image potential states

At a surface, an electron may be photoemitted from below the Fermi level to outside the metal, but without the energy necessary to reach the vacuum. The photoelectron induces a polarization in the metal, which can be represented as a positive image charge within the metal (figure 1.4). The Coulombic system of a negative electron bound to its positive image is known as an image potential state (IPS) and can be treated quantum mechanically like the hydrogen atom [16]. Image potential states have a hydrogenic progression of energy levels, with a quantum number n and a quantum defect a , corresponding to a phase factor:

$$E_n = \frac{-0.85 \text{ eV}}{(n+a)^2}. \quad (1.4)$$

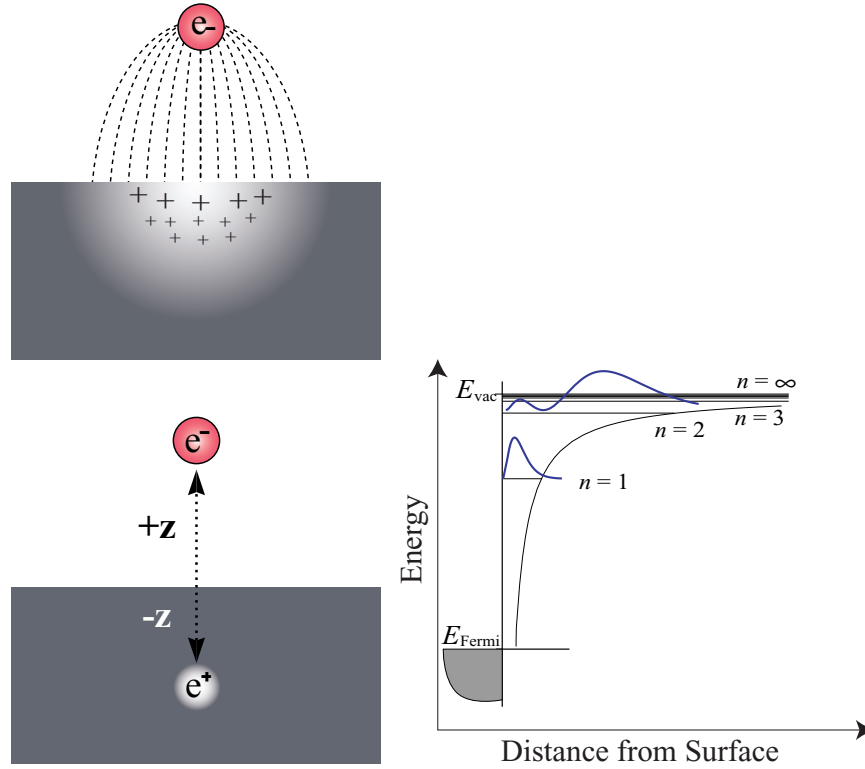


Figure 1.4: A photoelectron outside a metal surface can become bound to the surface via its self-induced polarization. The system of electron and its image charge is isomorphic with the hydrogen atom.

The expectation value of an $n = 1$ IPS electron's distance from the surface is 3.2 \AA , a distance that marks an IPS electron as a sensitive probe of adsorbed molecular layers via changes in its energy and lifetime [17]. Any change in photo-electron kinetic energy directly reflects a change in the layer itself. In the language of device materials, an IPS represents a free charge carrier at the interface, with the possibility of populating an anionic state of the molecular layer, including an electron affinity level or conduction band.

1.3.2 Excitons

The process of metal-to-molecule charge injection at an interface results in a net negative charge within the molecular layer, i.e., an anionic species is created. In contrast, for the case that an electron is excited from within the molecular layer, an exciton – a neu-

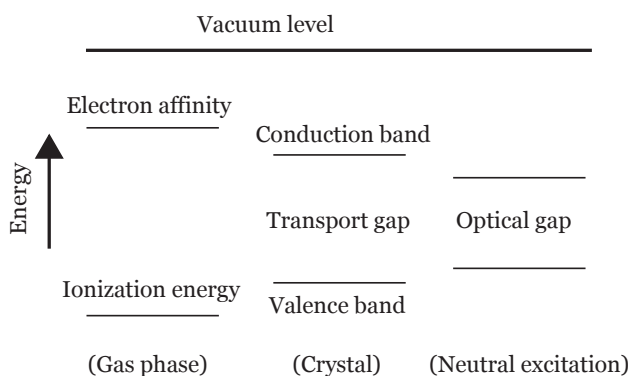


Figure 1.5: The ionization energy and electron affinity of a molecule in the gas phase will relax due to lattice polarizations in a crystal and become the valence and conduction bands, resp. An exciton exhibits additional relaxation energy from the bound electron-hole pair.

tral electron-hole pair – is created. The gas-phase analogue of an exciton is to populate a LUMO by exciting an electron from the HOMO of a molecule. In a molecular crystal, the energy levels are shifted from the gas phase due to a crystal relaxation energy as well as electron-hole stabilization (figure 1.5, *adapted from* Hill et al. [18]). Excitons are differentiated by their spatial extent. An on-molecule excitation is a Frenkel exciton, whose correlated electron-hole pair moves through a lattice as a unit. An electron-hole pair where one charge has migrated to a nearest neighbor is a charge transfer exciton. If the electron and hole are still correlated, but separated by length scales greater than a few molecules, the electron-hole pair is a Wannier(-Mott) exciton and can be modelled with a Coulombic potential that accounts for the molecules in-between the two charges as a dielectric medium. The binding energies of a Frenkel exciton are on the order of molecular electronic excitations, around 1 eV, while Wannier excitons are almost free and have binding energies on the order of 10 meV and electron masses around a free electron mass. Further information about charges in organic crystals may be found in Pope’s excellent reference text [19].

Distinguishing an exciton from anionic behavior usually involves increasing the thickness of a thin film to quench metal-to-molecule charge transfer, leaving behind only molecular excitations. Surface excitations can also be determined by adding another layer on top of an ultrathin film, such as xenon added to a D₂O surface to determine the location of solvated electrons [20]. Within recent Harris group studies C₆₀ has exhibited unambiguous

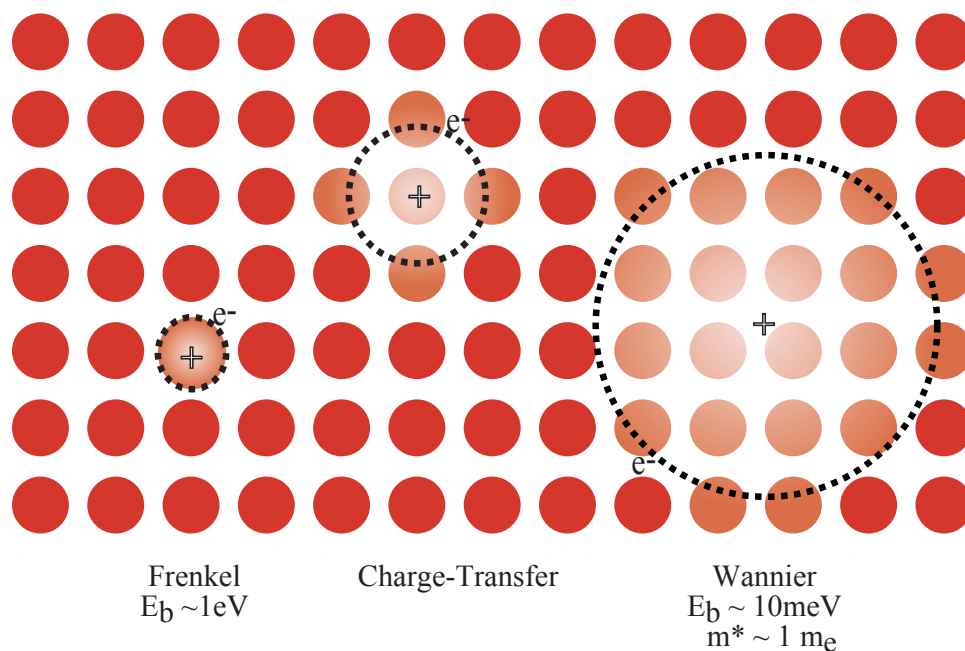


Figure 1.6: Exciton spatial extents.

excitonic behavior; tris-(8-hydroxyquinoline) aluminum (Alq_3), linear acenes, and functionalized fluorenes apparently feature only anionic charge transfer, although in the case of the fluorenes a low kinetic energy unidentified feature may be related to molecular transitions. If possible, matching the 2PPE binding energies to known values of interfacial intermediates states is preferable for identifying each peak in a 2PPE spectrum.

1.4 Molecular thin films at interfaces

The potential assembly of electronic and optoelectronic devices from organic semiconductors has driven considerable research into the behavior of electrons in molecular thin films. In an organic light-emitting diode (OLED), for example, the cathode/organic interface is integral to device efficiency, and the HOMO-LUMO alignment will affect charge injection into the layer. In ultrathin films, charge transport properties are affected by the structure of the adsorbate and the strength of adsorption, which often depend on the underlying substrate and its crystal face [21, 22]. The substrate may support interfacial states

(occupied or not) including image potential states, and the substrate may interact with the adsorbate to create substrate- and crystal face- specific electronic levels. The substrate also affects interfacial charge carrier properties through the energetic alignment of its Fermi level to the adsorbate. However, the chemical properties of the adsorbate molecule and interface do not solely account for the electronic properties at an interface.

Within the last few years, the study of molecular crystals has focused on the relationship between morphology and electronic properties. A positive correlation between crystallinity and electron mobility has created interest in monitoring deposition rates and substrate temperatures, which affect the quality of the deposited layer [23]. Crystal defects, grain boundaries, and molecular orientation can inhibit charge mobility by several orders of magnitude. Grain size has been demonstrated to affect mobility [24, 25]. Energetic disorder affects charge injection into an organic semiconductor [26], and islanding on top of a substrate can lead to electron confinement [27, 28]. The intermolecular crystal packing affects the degree of orbital overlap and, consequently, charge transport properties in organic semiconductors [29]. Identifying molecules suitable for use in devices thus relies on understanding the effects of morphology, geometry, and layer thickness on molecular electronic properties. The ultimate goal of cheap, easily manufactured, and stable organic solid state devices has focused attention on several classes of molecules, e.g., PTCDA and oligothiophenes. It should be noted that the systems of choice within our experimental capabilities are all effusively dosed, while device preparation usually involves spin-coating and/or depositing metal on top of the organic layer. In the case of the latter, the energy levels will be different than organic layers on a metal substrate. In chapter 3, a study of changes in electronic behavior in PTCDA thin films due to different layer morphologies is presented. An ongoing project on a family of oligothiophenes comprises chapter 4, including an analysis of chain length-dependent energy levels and polymorph-dependent charge localization.

Chapter 2

Experimental

Counting single electrons photo-emitted from an atomically clean surface requires specialized equipment, which can roughly be divided into an ultra-high vacuum (UHV) chamber, detection electronics, and a system of lasers (figure 2.1). The metal substrate is housed in an UHV chamber, and the layers are dosed either by molecular beam epitaxy (MBE) or by backfilling the chamber with a gas via a leak valve; the necessary method is determined by a material's vapor pressure. The detection electronics are capable of time-of-flight measurements of single electrons at repetition rates of 225 kHz, while the lasers provide low noise and high stability pulses. On average, a single 2PPE scan is collected over 20 sec – 60 sec with 20:1 signal-to-noise for the cleanest and most ordered surfaces, and the ratio decreases significantly with disordered surfaces. A typical data run lasts about a day, although overnight experiments are occasionally necessary. The upper limit on the length of an experiment is usually due to human fatigue and to laser instability over tens of hours, the former being mitigated with help from other members of Surface Side. The lower limit of a couple hours results from the finite time required to clean the crystal via sputtering and annealing, and to warm up and to tune the lasers. Running an experiment implies that the vital pieces of the apparatus are all functional, and to that end working in the Harris group engenders significant familiarity with repairing and/or maintaining all pieces of laboratory equipment.

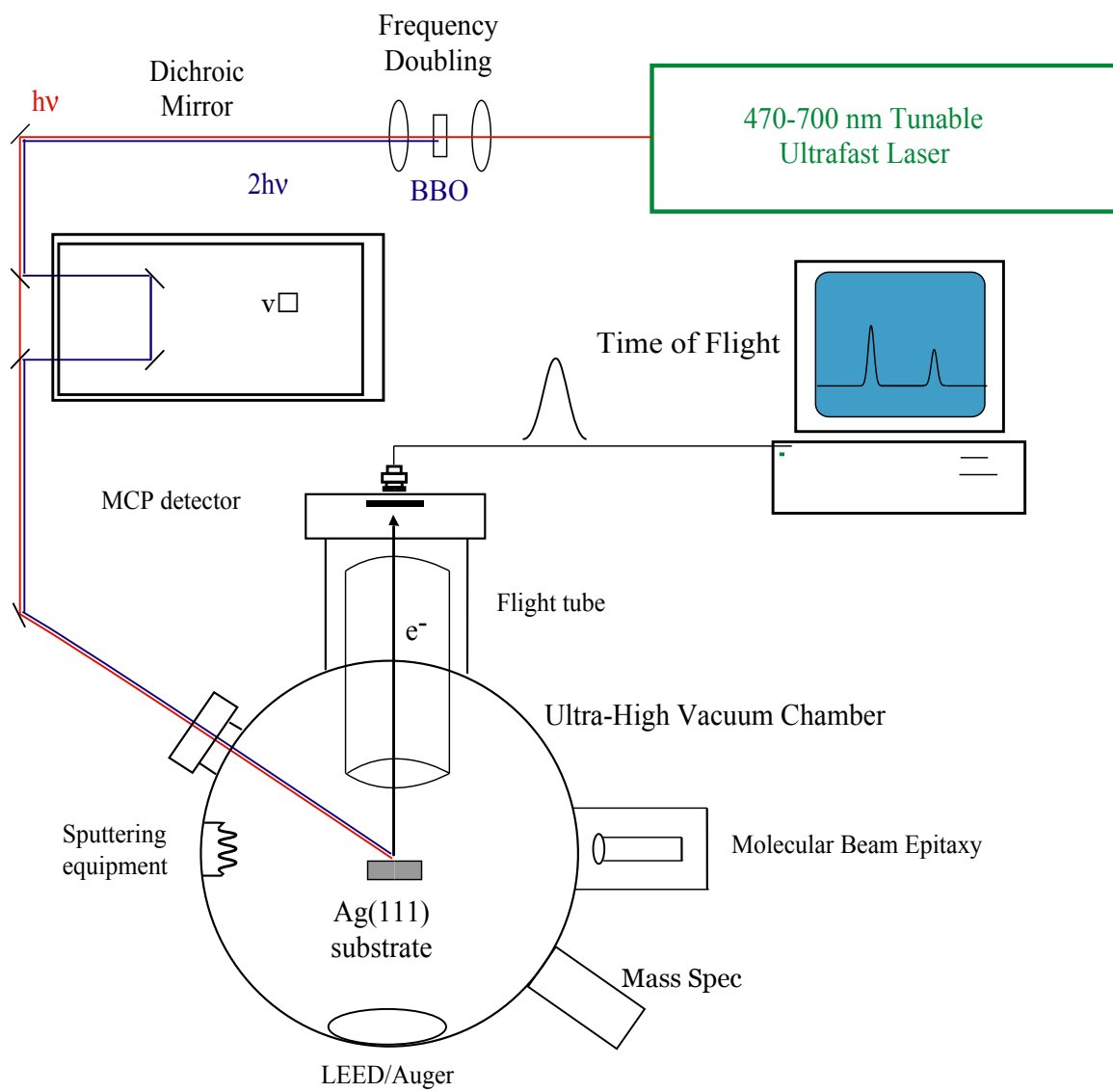


Figure 2.1: Experimental set-up.

2.1 Ultra-high vacuum chamber

The metal substrate is a Ag(111) crystal mounted on a manipulator arm in an ultra-high vacuum (UHV) chamber. Originally, the Ag(111) crystal was mounted such that angular dispersion measurements could be taken in the $\bar{\Gamma} - \bar{M}$ direction, i.e., to the midpoint of the surface Brillouin zone side, with 1° angular resolution. In the summer of 2007, the crystal was replaced by a new crystal oriented so that dispersions measured in the $\bar{\Gamma} - \bar{K}$ direction, which runs from the center to a hexagonal vertex of the surface Brillouin zone. Both crystals were obtained from MaTecK GMBH, and on both occasions the crystal was not manufactured according to specifications; further orders placed with MaTecK GMBH are strongly discouraged. The crystal is 99.999% pure and was cleaned with cycles of 20 minutes of Ar^+ sputtering at an argon pressure of 5×10^{-5} torr, an ion gun filament current of 20 meV, and an accelerating bias of 0.5 keV. The crystal was held at 500 K during its sputtering, which was followed by annealing the crystal at 725 K for 20 minutes. A Janis ST-500 cryostat was connected to the crystal with a copper braid, which enabled cooling the crystal to 130 K with liquid nitrogen. The base cryogenic temperature depended on the connection of the copper braid to the sample plate and on the cleanliness of the insulating sapphire beads behind the sample plate.

Contaminants with a unity sticking coefficient will cover a surface in 10^{-6} torr seconds, i.e., 1 torr exposure results in surface coverage in one microsecond and so on. Therefore, ultra-high vacuum pressures, on the order of 1×10^{-10} torr (1 torr = 1.33 Pa), are necessary to maintain sample purity throughout the course of an experiment, as well as to allow photo-emitted electrons to travel freely to a detector. All pressures reported herein are uncorrected for ion gauge sensitivity. The base pressure was maintained with a Perkin Elmer ion pump, while higher pumping loads from sputtering or from dosing via the leak valve were pumped with a BOC Edwards turbomolecular pump (EXT-250). The high voltage controller for the ion pump (Digitel 500) warranted servicing occasionally, but the usual culprit of the ion pump failing to hold voltage was a short in the (carbonized) feedthrough connector. If necessary, a standard high voltage supply can be used to pump the ion pump, although careful attention must be paid to matching the feedthroughs and cables, e.g., SHV to MHV. The ion pump gettering surfaces were occasionally refreshed with a filament in an attached

titanium sublimation pump. After venting to atmosphere for repair work, the chamber had to be baked at ~ 380 K to pump out adsorbed contaminants. Temperatures above 420 K would result in the failure of the windows, resulting in catastrophic, high temperature oxidation of multiple components of the chamber, e.g., filaments and multi-channel plates; care should be taken before a bakeout to double-check the thermocouple connection that measures the bakeout temperature and not to insulate the ion pump's poppet valve bellows. In addition, venting the chamber by filling it with clean N_2 when opening the chamber for repair reduces the bakeout length by a few days.

The chamber is equipped with a quadrupole mass spectrometer (SRS RGA-300), and a low-energy electron diffraction and Auger system (Omicron Spectaleed). Omicron's electrical feedthrough to the chamber is actually manufactured by Ceramic Seals Limited and can be obtained from Ceramic Seals at a fraction of the cost, although the delivery time may be longer since Ceramic Seals is located in the U.K. Auger data were recorded with Omicron's proprietary software, and LEED images were captured with an EHD KAMPro-02 CCD camera (EHD Imaging GmbH) and originally recorded with EE2000, Omicron's pre-packaged software. Future orders from EHD, or for that matter any European company, should ensure that the correct DC voltage power source is supplied. After a computer overhaul in the fall semester of 2007, we began using RoboRealm, a free visual imaging software available online, to capture LEED images from the camera. However, RoboReal distorts the dimensions of the image, e.g., the circular viewpoint becomes an ellipse elongated vertically, and therefore images were corrected with software before analysis. The mass spec could be used in conjunction with a temperature/heater feedback loop controlling the crystal temperature such that thermal programmed desorption (TPD) spectra were easily acquired. The temperature feedback loop utilizes a proportional-integrative-derivative (PID) controller,

Photo-electron kinetic energy was measured through time-of-flight analysis. The flight path of the photo-electron was shielded by a μ -metal flight tube to limit stray fields, and the flight tube was coated with colloidal graphite to prevent secondary electron emission. A colloidal graphite spray used in 2004 to re-coat the flight tube resulted in the unintended consequence that excess graphite desorbed from the flight tube and created graphite flakes on any horizontal surface within the chamber. This can be avoided in the future provided

that the flight tube is never wiped down completely; handling the flight tube with bare hands should be avoided and handling with gloves should be minimized. The detector was a matched pair of multi-channel plates (Burle Electro-Optics) in a chevron configuration preceded by a graphite-coated μ -metal cover with a narrow opening. The cover limited the photoelectron angular acceptance range. Further information about the construction of the detector may be found in Walt Merry's thesis [30]. Replacing the MCPs should only be accomplished with Walt Merry's 'jig,' which substantially reduces the peril of breaking these fragile wafers. A calibrated bias voltage was applied to the substrate to negate the potential difference between the sample and the detector due to mismatched Fermi levels; this negated stray electric fields inside the chamber, which affect time-of-flight measurements [31,32].

A molecular layer was dosed onto the Ag(111) substrate by one of two methods. If the vapor pressure of a compound was greater than ~ 100 mTorr at room temperature, e.g., monothiophene, then the chamber was controllably backfilled with the compound using a variable leak valve (Varian). The backfilling pressure and exposure time were measured in units of Langmuir, one micro-torr-second ($1 \text{ Langmuir} = 10^{-6} \text{ torr} \cdot \text{sec}$). Molecular beam epitaxy (MBE) could be used to dose compounds with vapor pressures less than 10^{-5} torr, such as quaterthiophene, α -sexithiophene, and PTCDA. The MBE chamber was attached to the main chamber by a gate valve (VAT valves) and pumped with a BOC Edwards turbomolecular pump (Ext-255H). Within the MBE chamber resided a finger-sized pyrolytical boron nitride (PBN) crucible (Applied EPI) which was loaded with the compound of interest. The crucible was controlled with a PID loop also supplied by Applied EPI; the control box essentially consisted of a Eurotherm PID box along with a current source and digital read-outs, although the read-outs were eventually disabled by the electronics shop while fixing the current source. The PBN crucible was then heated to the necessary temperatures to achieve optimal film growth, and the exposure time of the substrate was controlled both with the gate valve and with a mechanical shutter in front of the crucible that provided finer control. A bakeout was necessary to achieve low base pressures (10^{-9} torr), and the bakeout temperature was dependent on the material loaded in the cell. Unlike a main chamber bakeout, heating the filament was necessary during an effusion cell bakeout to avoid contamination from outgassing during the first few

experimental runs. Further information about construction of the MBE chamber can be found in the thesis of Sean Garrett-Roe, who designed it [33].

One attempt to load PTCDA resulted in a burst of PTCDA out of the crucible during the initial effusion cell pumpdown sequence. Possibly an air bubble was trapped behind the powder, and subsequent loads were carefully tamped to avoid another incident. The jet of PTCDA contaminated the blades of the turbo pump underneath, and cleaning the turbo pump involved immersing it in solvent. In addition, PTCDA had landed on the blades of the turbopump, which necessitated submerging the turbopump blades in solvent to remove any large particles that might damage the blades.

2.2 Detection electronics

While the most authoritative treatments of the detection electronics remain Walt Merry's and Jason McNeill's theses [30, 34], the unsettling spate of troubleshooting that has occurred in 2007 merits a closer look at the electronics involved in counting electrons. A photo-electron travels through the flight tube and hits the MCPs. This event initiates an electron cascade ($> 10^6$) that is accelerated by the applied voltages and creates a spike in a copper plate and, via capacitive coupling, the anode. The MCPs are available from Burle Electro-Optics as a matched pair within 10% by bias current and are specified as Detection Quality Long-LifeTM Microchannel Plate Set MCP 25/12/12 D 40:1 MS. A higher channel density is more expensive, but would allow higher voltages to be applied and presumably more signal to be collected. The MCPs are advertised as suitable for mass spectrometry at high vacuum, but several factors will degrade their performance. Accumulation of organic residues and therefore carbon; a (mono)layer of oil; and halogenated solvents and compounds all will degrade MCP performance. The applied voltage should be turned down whenever dosing gases into the chamber. The anode and first multichannel plate are held with zener diodes at +200 V relative to the rear plate and grid, respectively; a spike in current, such as one created by an arc across contaminated MCPs or by exceeding 2.4 kV, will damage the zener diodes and cause them to short. A gradual desensitization of the copper plate as it oxidized and accrued contamination warranted an attempt to re-anodize

it using an electrochemical cell. This attempt failed due to a negligent reversal of anode and cathode and resulted in the voltage-supplying copper strip detaching from the copper plate. The copper strip was re-attached using an epoxy manufactured by EPO-TEK. The epoxy was NASA-approved, conductive, and safe-for-UHV, and as of this writing NASA maintains a website of low outgassing materials [35].

Outside the chamber, the signal from the anode passes through a 10X attenuator (Tektronix) and a 100X pre-amplifier (Phillips Scientific 6954 B 100). In troubleshooting the MCPs, a signal should be readable straight from the anode into an oscilloscope, and the attenuator and pre-amplifier may be tested with a wave generator. The amplified spike passes into a Tennelec Quad Constant Fraction Discriminator (TC 455); Ortec delay gate (425 A); and into a Canberra 2043 time-to-amplitude converter (TAC). Meanwhile, the photodiode sends a signal to a constant fraction differential discriminator (Ortec 593), although part of the signal is also sent to an oscilloscope. The photodiode signal output from the CFD is passed to the TAC, and the photo-electron's time-of-flight is measured with the photodiode signal as the start and the MCP signal as the stop. The TAC passes the time-of-flight to the analog-to-digital converter (Ortec 918A Adcam Multichannel Buffer), which then adds a count to its appropriate time-of-flight bin. Finally, the photo-electron counts are sent to the data computer, and time-of-flight is converted into kinetic energy by simple classical mechanics. The entire system was calibrated using a literature value of -0.77 eV for the binding energy of the $n = 1$ image potential state on a clean Ag(111) surface, and by comparing the known probe photon energy with the measured difference between a uv-probed and vis-probed $n = 1$ image potential state to establish a multiplicative factor for the data. The raw counts were also scaled with a Jacobian so that the number of counts in a time bin were equal to the counts in the corresponding kinetic energy bin. In light of occasional problems interfacing the computer to the electronics rack, newer electronics are available from Ortec that negate the need for an entire electronics rack and can be inserted directly into a computer's card slot.

2.3 Lasers

Detailed descriptions of the lasers have been published in references [15] and [36]. Generating femtosecond pulses was accomplished with a commercial ultrafast laser system purchased from Coherent, Inc. A Coherent Mira 900 Ti:Sapphire oscillator and a Coherent RegA 9000 Ti:Sapphire regenerative amplifier were pumped, respectively, with a Coherent Verdi V10 Nd:YVO₄ pump laser and a Coherent Verdi V5 Nd:YVO₄. The output of the oscillator was a 76 MHz pulse train centered at 800 nm with ~ 12 nm bandwidth. The pulses were regeneratively amplified by the RegA operating at 225 kHz with cavity output powers of approximately 1.3 W. The RegA pumped a Coherent optical parametric amplifier (OPA) which generated tunable visible light from 500 nm – 700 nm. The OPA visible output was compressed via prism pairs to 70 fs – 140 fs, depending on the wavelength. The pulses were frequency-doubled with a type I BBO crystal to generate uv light, after which a dichroic mirror separated the beam into a uv path and a visible path. Time-dependent spectra were acquired by delaying the visible pulse with respect to the uv pulse; this was accomplished by changing the path length of the visible pulse with a Klinger translation stage in increments of one micron, at minimum. The *p*-polarized laser pulses hit the sample 60° from the surface normal with an average pulse energy of 1 nJ per uv pulse (250 nm – 270 nm) and 12 nJ per visible pulse (500 nm – 540 nm). The lasers were usually functional for an experiment after an hour of tuning on a daily basis, although laser days devoted to large-scale maintenance were occasionally required. Only major issues, such as the replacement of key components, necessitated calling the Coherent technicians; however, it is advised to call the Coherent technicians to replace the more expensive components. An attempt to replace a cavity dumper with a significantly cheaper one purchased from Coherent's supplier (Harris, Inc.) resulted in a long layoff upon discovering that another issue existed, namely, that the malfunctioning RegA control box was supplying too much RF power to the cavity dumper which destroyed the cavity dumper electrical leads.

2.4 Materials

PTCDA, 3,4,9,10-perylene tetracarboxylic dianhydride, was obtained from both Fluka (purum, $\geq 98.0\%$) and TCI America ($> 98\%$). After loading a crucible into the effusion cell described above, the material was outgassed at 380 K for at least 24 hours while the effusion cell was also baked out at ~ 80 C. Each source yielded identical results. Initially, the PTCDA in the Knudsen cell was regularly refreshed, as it had a tendency to crystallize in the crucible and thus reduce the flux when dosing. Later I discovered the crystallization was due to ramping the PID at excessive maximum currents (> 5 A), and lowering the maximum current prevented crystallization. For the majority of my PTCDA experiments, the crucible was maintained at 638 K during dosing, while the substrate temperature was varied from 130 – 540 K in order to control growth morphology. Obtaining mass spectra of the source material proved beyond the means of our mass spectrometer, which only ranged to 300 amu, and also beyond the means of the mass spec facility located in the Chemistry Department. Therefore, the content of a film was monitored only with LEED and Auger, and the purity could not be quantified. Quaterthiophene and α -sexithiophene were purchased from Sigma-Aldrich and treated similarly to PTCDA.

Monothiophene (Alfa Aesar, 99%; Sigma-Aldrich, puriss p.a., GC standard, $\geq 99.5\%$) was loaded into 5 mL glass sample bulbs and attached to the sample line. Freeze-pump-thaw cycles using liquid nitrogen were commenced and continued until no residual contaminant gases could be detected as air bubbles and the vapor pressure above the frozen liquid remained stable and negligible (< 0.5 mTorr) while the bulb was open to the sample line vacuum. The sample line was then baked out around 70 °C until the pressure dropped to below 10^{-6} torr. The sample line could be roughed with a mechanical pump to ≤ 20 mTorr, and then switched to an oil diffusion pump (BOC Edwards DiffStak) to obtain pressures below 10^{-6} torr. A liquid nitrogen trap also helped pump the sample line, especially in the case of volatile organic molecules.

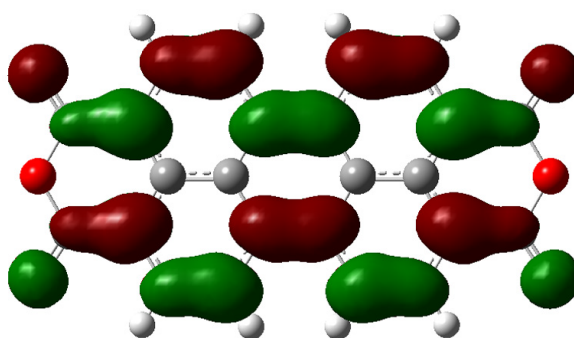
Chapter 3

PTCDA

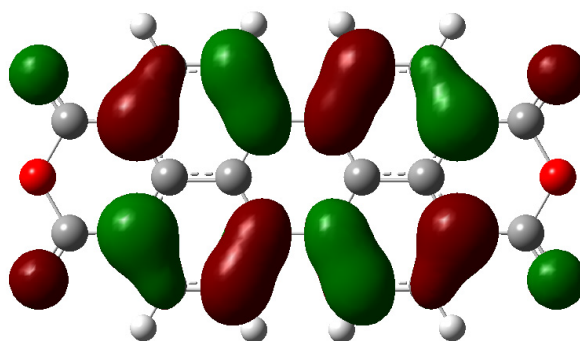
Semiconducting planar aromatic hydrocarbons show promise for use in field-effect transistors, light emitting diodes, and photovoltaic cells [37]. A prototype for this class of hydrocarbons is 3,4,9,10-perylene-tetracarboxylic dianhydride (PTCDA) (figure 3.1). This molecule is cheap to produce, absorbs in the visible spectrum, and resists photo-degradation.

3.1 Background

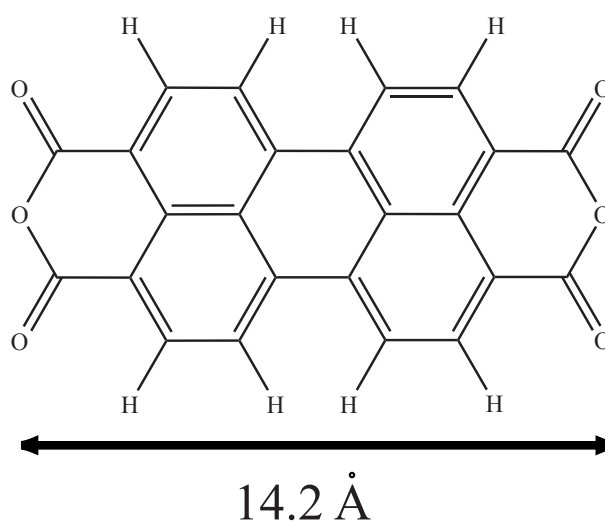
Quasi-epitaxial growth of PTCDA by molecular beam deposition was demonstrated with x-ray diffraction and birefringence [38] and further characterized with RHEED, STM, XRD, and other optical and electronic techniques [39]. The herringbone structure and quasi-epitaxial growth of PTCDA on a Ag(111) substrate has been characterized at length with XRD and AFM [40]; HREELS [18, 41]; STM and LEED [42]; and more detailed SPA-LEED [43]. The electronic structure of PTCDA has been studied in the bulk phase and at various metal interfaces [44–47], and measurements of charge transport properties are reported in the literature [37, 48]. Interestingly, PTCDA exhibits different semiconductor properties in its planar direction (n-type) than in its perpendicular direction (p-type). A hole effective mass of $m_h^* = 5.28 m_e$ was reported, with a mobility greater than $3.8 \frac{cm^2}{V \cdot s}$ [49]. The electron mobility is discussed below. Optical anisotropies of bulk PTCDA have also been reported, with excitons observed in-plane and a narrow absorption peak out-of-plane [50].



(a)



(b)



(c)

Figure 3.1: (a) The PTCDA LUMO. (b) The PTCDA HOMO. (c) PTCDA skeleton.

While the greatest optical spectra is visible in the normal direction, at least some of the spectra should be polarization independent [44].

Several studies have examined interfacial electronic states of PTCDA specific to the Ag(111) surface that are hybrid states of PTCDA bulk electronic states mixing with the Ag 5sp band, which imparts metallicity to the PTCDA monolayer [41, 51]. Tautz et al. [51] make an analogy between potassium-doped PTCDA and PTCDA on Ag(111). In the latter case, metallicity is imparted by contact between partially filled molecular orbitals and an electron reservoir from the metal surface. As a consequence, effective mass measurements were reported at the interface of $0.47 m_e$ using STM and STS (scanning tunnelling spectroscopy) [52]. Conversely, a study of interfacial energies of metals on PTCDA, including Ag, found that Ag formed abrupt, unreacted surface, although the film thicknesses chosen were 400 Å– 800 Å [53]. A physical picture for the substantial electronic interfacial mixing is given by Eremitchenko et al. [54], who proposed that the commensurate growth of large π -conjugated molecules on crystalline substrates resulted from local molecular centers finding epitaxial growth sites. In the case of PTCDA, the extended π -electron perylene core of PTCDA tethers to the Ag(111) surface. Hauschild et al. report that the binding mechanisms of PTCDA to the surface are twofold: edges of PTCDA and carboxylic oxygen atoms curl down to the surface, and the PTCDA LUMO, extended over the perylene skeleton (figure 3.1c), is partially filled from the metal surface [55, 56]. In contrast, PTCDA on semiconductor surfaces exhibits little chemical interaction [57].

3.2 Materials

3.2.1 Dosing calibration

The source material was maintained at 638 K during dosing, while the substrate temperature was varied from 130 K – 540 K in order to control growth morphology. The morphologies are referred to by the substrate temperature while dosing, e.g., $T_D = 200$ K indicates the layer-by-layer growth exhibited at a substrate dosing temperature of 200 K. Note that the temperature at which the substrate was held while 2PPE was collected may be different from T_D . Experiments were concentrated on four substrate dosing temperatures

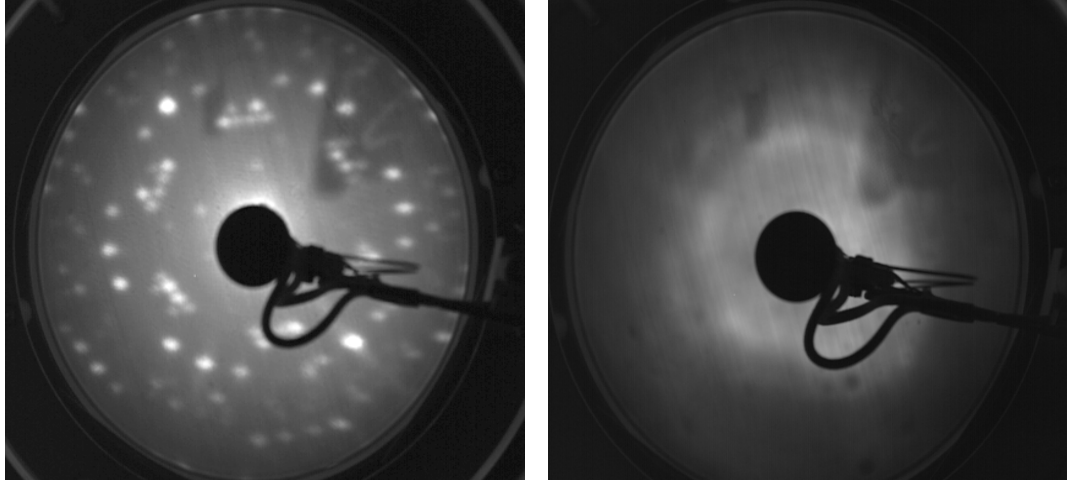
(a) $T_D = 540$ K(b) $T_D = 140$ K

Figure 3.2: (a) LEED of 1ML at beam energy of 17.7 eV, $T_D = 540$ K. (b) LEED of 1 ML at beam energy of 16.1 eV, $T_D = 200$ K. Both samples were at 140 K when LEED was taken.

that represented different morphologies: $T_D = 140$ K, $T_D = 200$ K, $T_D = 300$ K, and $T_D = 450$ K. Adsorption and desorption temperatures for the first few monolayers were determined by the appearance or quenching of peaks in the 2PPE spectrum, which also provided dosing calibration. We refer to layer thicknesses in units of overall monolayers (ML) dosed, with the recognition that the “monolayer” unit – a complete layer of one molecule thickness – is a misleading label for the actual thickness at the surface in the case of three-dimensional morphologies.

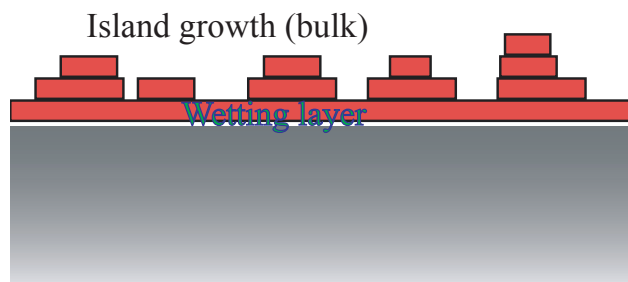
3.2.2 Growth modes

PTCDA layers exhibit different growth modes on Ag(111), depending on the substrate temperature during dosing (T_D). Krause et al. [40] have published AFM studies of temperature-dependent morphologies of PTCDA on Ag(111), with average thicknesses of 50 Å. The morphological regimes include a mesa-like structure at $T_D = 135$ K with small islands arranged along the silver substrate steps; a smooth surface at room temperature; and a faceted surface at 333 K leading to a transition at 343 K to islands growing on top of a

complete ‘wetting layer,’ i.e., Stranski-Krastanov growth (figure 3.3). The wetting layer in this morphology is two monolayers thick. Islands range in size from $0.1 \mu\text{m}^2$ at 343 K to $5 \mu\text{m}^2$ at 413 K, and island densities range from $12 \mu\text{m}^{-2}$ at 343 K to $0.001 \mu\text{m}^{-2}$ at 413 K. The crystallinity of the layer also increases with higher substrate temperatures (figure 3.2). Attempts to model the temperature dependence of the 2D-3D transition in the growth of PTCDA on Ag(111) with kinetic Monte Carlo simulations suggest that the growth modes are dependent on interlayer transport and lattice strain [58]. Soubiron et al. [59] have reported covalent linkage between PTCDA and Si atoms for submonolayer coverages on Si(110), which leads to a disordered and passivating initial layer followed by island growth. Ferguson and Jones have studied the effects of growth temperature and morphology on optical properties of bulk films (>100 nm thickness), with the results that increased low-energy absorption, enhanced blue-shifted emission, and longer fluorescence decays correspond to increases in the dosing temperature [60]. For the research in this chapter, different morphologies of ultrathin films of PTCDA at the Ag(111) surface were probed with angle-resolved two-photon photo-emission (2PPE) to study the effects of morphology on lifetimes and effective masses of unoccupied states [61].

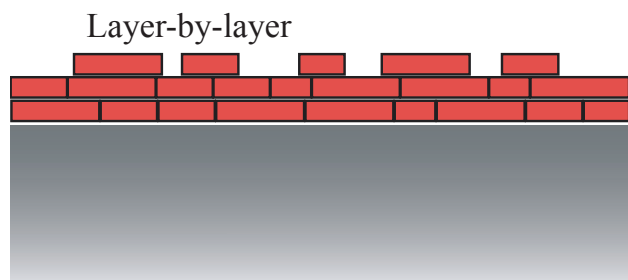
3.2.3 Morphology control

Desorption temperatures of PTCDA layers were determined using 2PPE spectra to track electronic changes in the layer. Four monolayers were dosed at 300 K, and 2PPE spectra were taken around 340 – 370 K after holding the sample at incremental steps in temperature (figure 3.4). Annealing at 470 K for 300 seconds resulted in recovery of 2 ML data equivalent to dosing 2 ML at high temperatures. At 485 K, the 1 ML $n = 1$ peak re-appears and rapidly increases at higher temperatures and longer annealing times while the 2 ML $n = 1$ peak disappears. Clean Ag spectra were never recovered despite ramping the substrate temperature up to 600 K, from which we conclude that the chemisorbed 1 ML coverage desorbs in fragments and leaves behind carbon residue on the surface; a quenched $n = 1$ peak is indicative of a dirty Ag(111) surface. Qualitatively, this behavior matches the thermal desorption data of Kilian et al. [43], who assign a multilayer desorption peak at 520 ± 20 K and a 2 ML desorption peak at 540 K, with no desorption peak for 1 ML. The onset



Stranski-Krastanov

(a) Stranski-Krastanov



Frank-van der Merve

(b) Layer by layer

Figure 3.3: PTCDA exhibits different growth modes, depending on substrate temperature. At low temperature, layer-by-layer (± 1 ML) growth dominates, while higher substrate temperatures leads to Stranski-Krastanov growth.

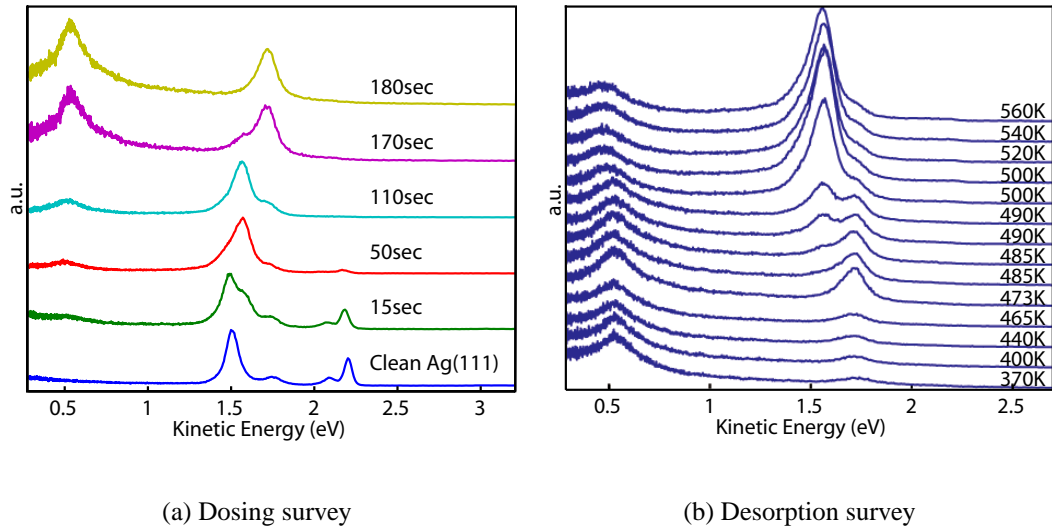


Figure 3.4: (a) PTCDA spectra grows in after 100 sec dosing, with a room temperature substrate for both the dosing temperature and spectra collection temperature. (b) Desorbing bulk coverages results in the same signal as dosing at similar temperatures. In both cases shown, the visible photon energy was 2.25 eV.

of the multilayer desorption peak in Kilian's Figure 4 begins around 480 K, and the onset of 2 ML desorption is roughly extrapolated to be 500 K.

3.3 Workfunction and Vacuum Level Shifts

The kinetic energy spectrum for 1.5 ML, dosed at $T_D = 300$ K, is presented in figure 3.5. Peak A is identified as derived from a molecular state, peak B as the $n = 1$ IPS for 1 ML, and peak C is the $n = 1$ IPS for 2 ML. The appearance of peaks at separate energies is a distinguishing feature of layer-by-layer growth. Knowledge of the proper workfunction (Φ) of each layer is necessary to assign an accurate binding energy to each intermediate state. The shift in workfunction results from several factors. Hill et al. [62] report a surface dipole shift as a PTCDA layer is adsorbed on the surface, which creates a negative charge barrier at the surface. Similar results using an *ab initio* calculation have been obtained by Vazquez et al [63]. In addition, when PTCDA is dosed on a surface, the electronic levels of PTCDA may mix with the Ag 5sp band at the interface [51]. The shift in the vacuum level

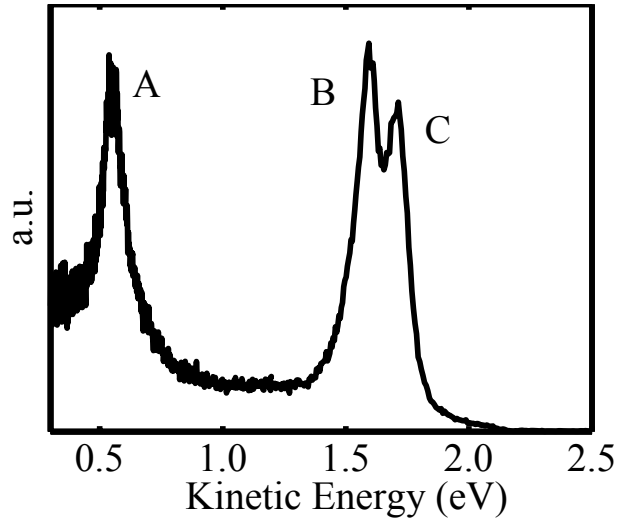


Figure 3.5: Peak A denotes a PTCDA molecular state. Peaks B and C are the $n = 1$ image potential state energies for 1 and 2 ML, which are both seen here as a result of incomplete layer-by-layer growth at $T_D = 300$ K and the crystal at 140 K for data collection.

was determined for PTCDA by fitting the $n = 1$ and $n = 2$ image state binding energies to a hydrogenic progression:

$$E_{\text{IPS}} = \frac{-0.85}{(n+a)^2} \text{eV}, \quad (3.1)$$

where a is a quantum defect parameter [16]. For PTCDA, a is 0.11. The shift in the vacuum level is the amount by which the experimental IPS energies must be shifted so that they fit a hydrogenic progression, since the convergence of higher-order IPS energies is pinned to the vacuum level.

The shifts in vacuum level (figure 3.6) for $T_D = 300$ K and $T_D = 450$ K indicate that the first monolayer experiences negative charge transfer into the underlying Ag(111) surface, which creates a surface dipole that increases the vacuum level. The lesser binding energies at 1 ML are due to the Ag surface sharing electron density with PTCDA electronic levels, mainly through the perylene core being tethered to the Ag surface [54]. Although the peak binding energies remained the same for equivalent doses of various morphologies, the linewidths for the LUMO increased drastically for low temperature growth, from 0.1 eV at annealed coverages to 0.7 eV for PTCDA dosed at 140 K. The broadening of the linewidth correlates with a disordered surface and is therefore attributed to inhomogeneous broadening. Uneven coverages were also evident at $T_D < 300$ K from the simultaneous

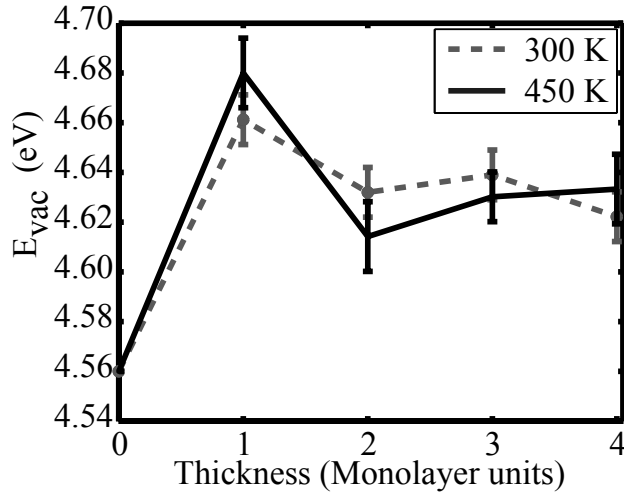


Figure 3.6: The layer-by-layer evolution of the vacuum level from Eqn. 3.1 for $T_D = 300$ K and $T_D = 450$ K, referenced to the clean silver value.

existence of both 1- and 2-ML peaks. However, annealing the layer at 470 K and 500 K resulted in recovery of data equivalent to dosing at those temperatures. Lower dosing temperatures resulted in spectra where the IPS were difficult to resolve and fit. By using equation 3.1, the vacuum level shift $\Delta\Phi$ for 1 ML is 0.11 eV with respect to the bare surface, and for 2 ML the total shift is 0.06 eV. The $n = 1$ IPS binding energy stays constant for thicker coverages, which suggests that the vacuum level has stopped shifting, but the $n = 2$ IPS is quenched by 3–4 ML in all coverages which precluded using Eq. 3.1 as a method of confirming this. The $n = 2$ IPS is theoretically at a greater distance from the surface than $n = 1$, and thus harder to populate from the metal if thicker coverages have been applied. The shift in vacuum level is similar to vacuum level shifts for naphthalene [12] and benzene [10].

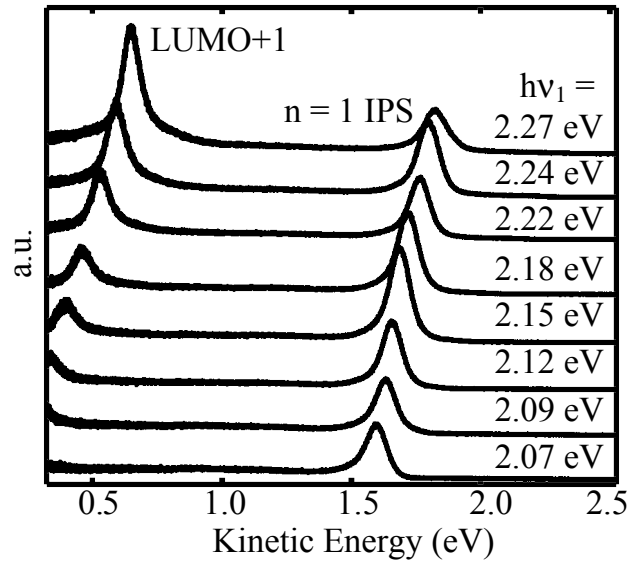
For cases where the necessary image potential states were not visible, the workfunction shift can be determined through the high-energy and low-energy cutoffs in 2PPE kinetic energy spectra. The width of the kinetic energy spectra subtracted from the energy of two UV photons is equivalent to the width of the unoccupied states. At the interface, this is the distance from the Fermi level to the vacuum level, i.e., the workfunction. The changing unoccupied state width was used to track the evolution of the valence band as the PTCDA coverage was increased. An accelerating bias voltage can be applied to the sample such that

E_{VB} (eV)							
1 ML	2 ML	3 ML	4 ML	5 ML	6 ML	7 ML	8 ML
$T_D = 450$ K							
4.7 ± 0.1	5.0 ± 0.1	4.8 ± 0.4	5.0 ± 0.1	5.0 ± 0.4	5.0 ± 0.1	4.8 ± 0.1	4.9 ± 0.1
$T_D = 300$ K							
4.6 ± 0.1	4.7 ± 0.2	5.2 ± 0.6	5.4 ± 0.7	5.5 ± 0.7	5.8 ± 0.2	6.1 ± 0.1	6.2 ± 0.1
$T_D = 200$ K							
4.8 ± 0.1	4.9 ± 0.1	4.9 ± 0.1	4.9 ± 0.1	5.0 ± 0.2	5.2 ± 0.2	5.7 ± 0.2	6.2 ± 0.2
$T_D = 140$ K							
4.6 ± 0.1	4.6 ± 0.1	4.8 ± 0.1	4.8 ± 0.2	5.8 ± 0.5	5.8 ± 0.2	6.2 ± 0.1	6.3 ± 0.1

Table 3.1: The evolution of the unoccupied states E_{VB} as more PTCDA is dosed. The rise in E_{VB} occurs more rapidly for low T_D amorphous layers than for high T_D crystalline layers.

both a low- and high-energy cutoff are present in 2PPE kinetic energy spectra. The width of the unoccupied states for each layer is initially close to the workfunction determined by IPS and is followed by a transition to the value for bulk PTCDA, except for the layer grown at $T_D = 450$ K (Table 3.1). As expected, thicker, layer-by-layer coverages converge to the bulk PTCDA workfunction value of 6.4 eV. The three-dimensional nature of high dosing temperature, Stranski-Krastanov growth can leave the wetting layer exposed, and the utility of measuring the scattering width of 2PPE kinetic energy spectra will be limited by the exposed wetting layer.

A wavelength survey was taken to help determine the proper binding energy of each peak. In figure 3.7(a), the 2PPE spectra at various wavelengths is presented, where the higher energy peak is the $n = 1$ IPS and lower energy peak is the LUMO+1, consistent with the results of Temirov et al. [52]; the peak assignment is discussed further below. By plotting the peak kinetic energies vs. the visible photon energies (figure 3.7(b)), a slope of two is obtained for the LUMO+1, and a slope of unity for the IPS. The LUMO+1 is therefore photo-emitted by $h\nu_2$, and the IPS by $h\nu_1$. The binding energies of the $n = 1$ IPS are 0.82 eV (referenced to the vacuum energy E_{vac}) at 1 ML and 0.68 eV for subsequent layers, across all morphologies. An IPS electron is sensitive to a dielectric layer between the electron and the metal substrate, and the uniformity of IPS binding energies indicates that the first two layers for all morphologies have negligible differences in dielectric constants due to morphology. However, the quenching of image potential states occurs at different



(a) Wavelength Survey

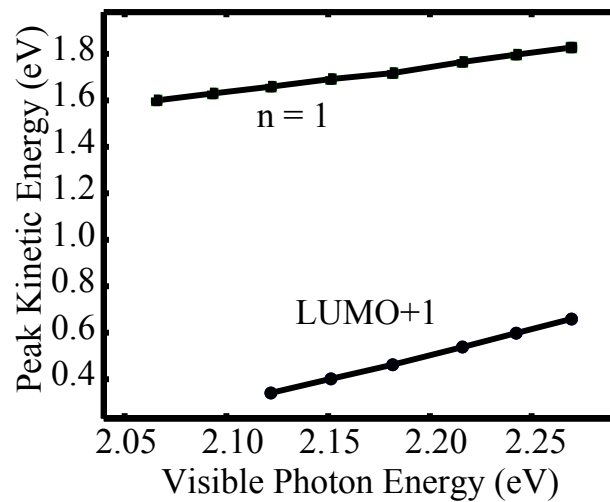
(b) Peak Energy vs. $h\nu_1$

Figure 3.7: (a) 2PPE spectra were obtained for a range of wavelengths, labeled by $h\nu_1$. (b) Using the slope of the peak kinetic energies vs. visible photon energies, we can determine if the state is probed by $h\nu_1$ or $h\nu_2$. The substrate was held $> 470\text{K}$ to dose PTCDA, and the wavelength survey was collected at a substrate temperature of 150 K.

layer thicknesses for each morphology.

For 1–2 ML dosed at temperatures less than 400 K, PTCDA lacks the energy to completely re-organize into a smooth wetting layer. Patches of 1 ML are left exposed in the wetting layer, and the $n = 1$ IPS at the 1 ML energy value is still visible after 2 ML has been dosed at $T_D < 400$ K. In a 2 ML thick layer in which both image states are visible, the 1 ML $n = 1$ state at 0.82 eV disappear if the layer is annealed above 450 K, and the population of $n = 1$ at 0.68 eV increases. LEED images corroborate that low T_D layers are initially amorphous, but align into a crystalline surface after annealing at higher temperatures. The $n = 1$ IPS is completely quenched by 20 ML at $T_D = 450$ K; 10 ML for $T_D = 300$ K; 4 ML for $T_D = 200$ K; and 3 ML for $T_D = 140$ K.

The electronic structure derived from molecular states varies more significantly with morphology. Peak A in figure 3.5, the LUMO+1 state, is present in crystalline layers, from which binding energies of 4.1 eV for 1 ML and 4.0 eV for 2 ML and thicker were obtained. Increasing the photon energy results in one-photon photo-emission, without the appearance of a new peak, but we label Peak A as the LUMO+1 in agreement with the energy levels in ref. [52] and consistent with Tautz et al. [51], who identify the lowest unoccupied state at the interface as a hybrid Ag-PTCDA state. That the peak is never quenched corroborates the result that, beyond the wetting layer, the growth mode is not layer-by-layer. Several references also suggest that the LUMO has shifted below the Fermi edge as it hybridizes with the silver surface at the first monolayer coverage [51, 64]. Identification of the peak, then, necessitates examining the shifts of the workfunction. For low T_D morphologies, a broadened electronic structure dominates the spectra at low kinetic energy, in lieu of a sharp peak (figure 3.8). The broad structure disappears while a sharp peak grows in if the layer is annealed, with annealed spectra similar to spectra of a layer which had been dosed at the annealing temperature. The origin of this manifold is unclear from 2PPE experiments; the simplest explanation is that it represents an inhomogeneously broadened peak resulting from scattering in an amorphous layer. More specifically, in a layer frozen in place, a distribution of aggregates will form which create traps due to molecules packing differently from bulk crystals and incommensurate with the surface. Interestingly, this manifold exhibits long time dynamics, as discussed below.

Interestingly, no strong absorption peaks from true molecular states were readily ap-

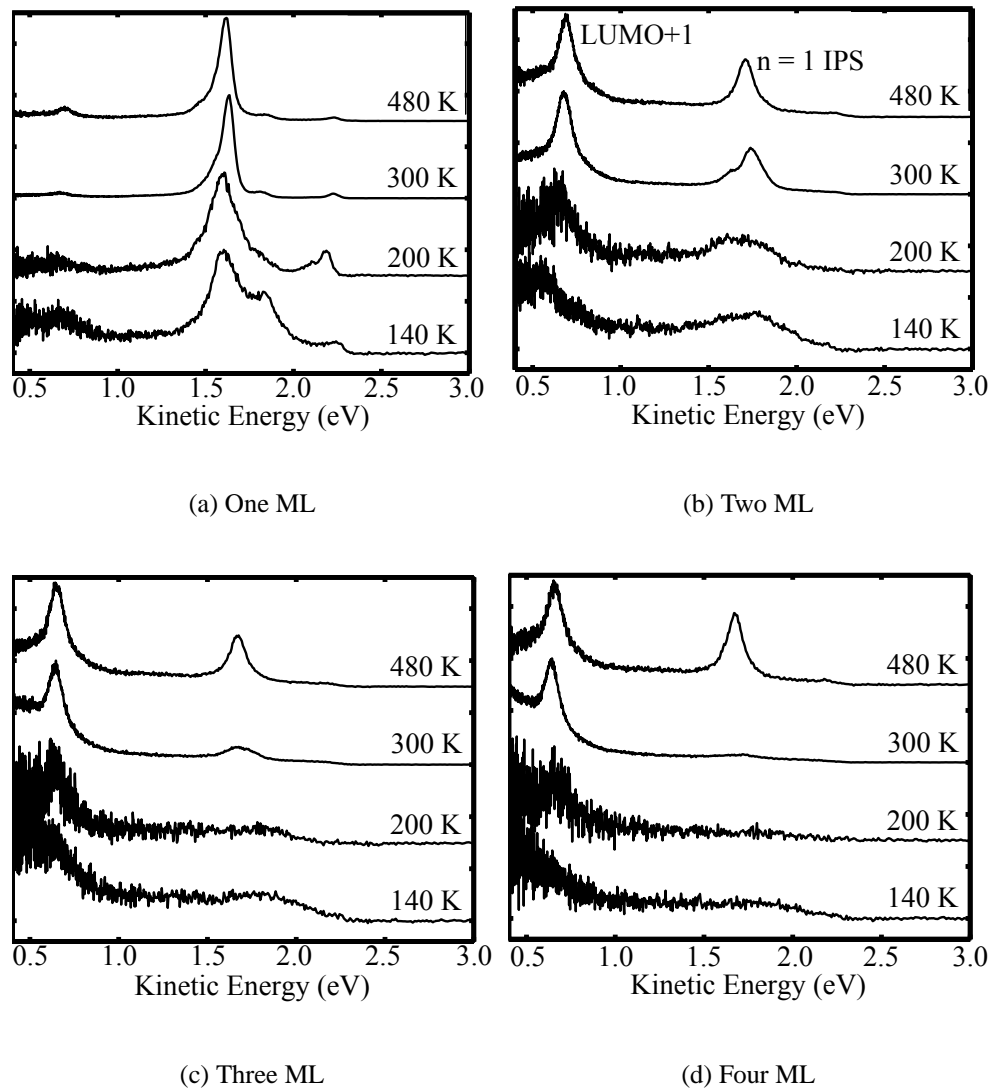


Figure 3.8: A stackplot comparison of 2PPE data for 1–4 ML of different PTCDA morphologies. The data have been normalized so that the maximum of each spectrum is unity. The $n = 1$ IPS is quickly extinguished in layer-by-layer growth at low T_D , and the LUMO+1 in crystalline layers is well-defined. The temperatures given are for the dosing temperatures, and data were collected at a substrate temperature of 140 K.

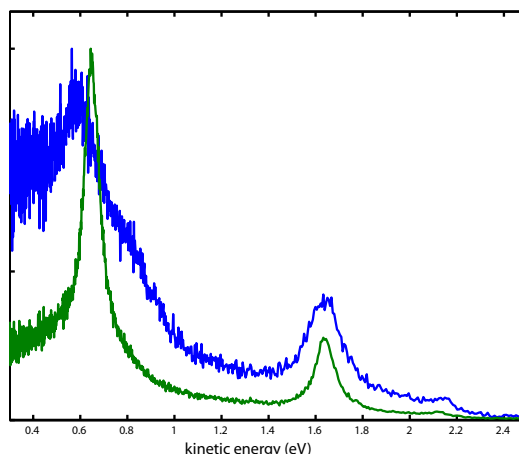


Figure 3.9: Room temperature vs. 140 K spectra.

parent, despite the rich absorption and fluorescence spectra in thin films [65]. At room temperature, the spectra more closely resemble bulk absorption spectra of PTCDA films (figure 3.9), but not definitively. Certainly the room temperature spectrum in figure 3.9 resembles published one-color 2PPE data of 50 nm PTCDA on HOPG [66], especially long-lived states at low kinetic energy; perhaps the density of exciton energy levels precludes any sharp peak collection. Credibly deconvoluting the various peaks at high spectral collection temperatures, especially for the purposes of following population dynamics, taking wavelength surveys, or fitting effective masses, generally proved unreliable, and so only the low temperature spectra were fit. That the photo-electron peak intensity blue-shifted when taking spectra while lowering temperatures suggests that the population shifted from lower-energy charge-transfer excitons, which require thermal energy for a charge to cross from one molecule to the next, and instead excited electrons populated excitons with mainly an on-molecule Frenkel character. Lowering the temperature also possibly froze out the higher-order vibronic progression characteristic of a Frenkel exciton manifold, so that the dominant peak is related to the lowest-order peak and not higher energy bands. The photo-electron signal intensity of the exciton manifold increases at thicker coverages, which suggests that the manifold is a feature of PTCDA thin films as opposed to arising from surface or interfacial states.

Attempts at changing the polarization of the pump and probe peaks to excite different

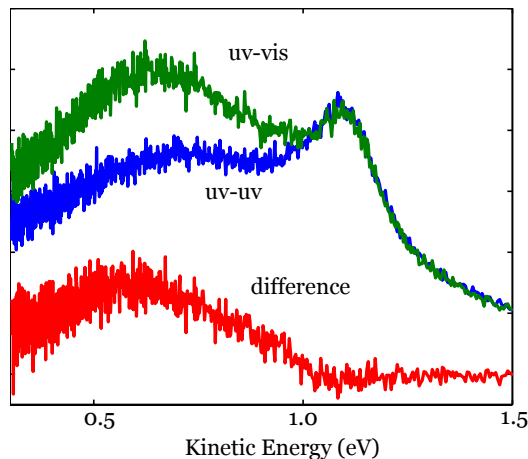


Figure 3.10: Spectra of 3 ML, $T_D = 300$ K, and a visible photon energy of 1.94 eV. By lowering the photon energy to avoid photoemitting the LUMO+1 peak, electronic structure with a molecular orbital basis is visible.

electronic modes proved unsuccessful, but the limitation was that both polarizations were changed to *s*-polarized, instead of just the probe. If it were easily possible in the current experimental set-up, changing just the probe might lead to observing planar excitonic states. I also tried to vary photon energies to find resonances. Perhaps not surprisingly, the greatest increase in signal when integrating total counts over the LUMO+1 state, while maintaining a constant incident pulse power, occurred at a uv photon energy of 4.6 eV. Mapping out signal vs. much higher energy photon energies was not possible because of 1PPE from the metal surface. Finally, I reduced the photon energies ($h\nu_1 < 600$ nm) so that the LUMO+1 state would not be photoemitted, in case it was swamping signal from true molecular states. Structure is apparent in both uv-uv and uv-vis spectra, with at least some dynamical information (the difference spectra) in figure 3.10. However, deconvoluting these peaks to take a wavelength survey so that I could determine binding energies was not possible. Therefore, mapping these energies exactly to absorption spectra was not possible. Using liquid helium to cool the crystal to lower temperatures might give more positive results.

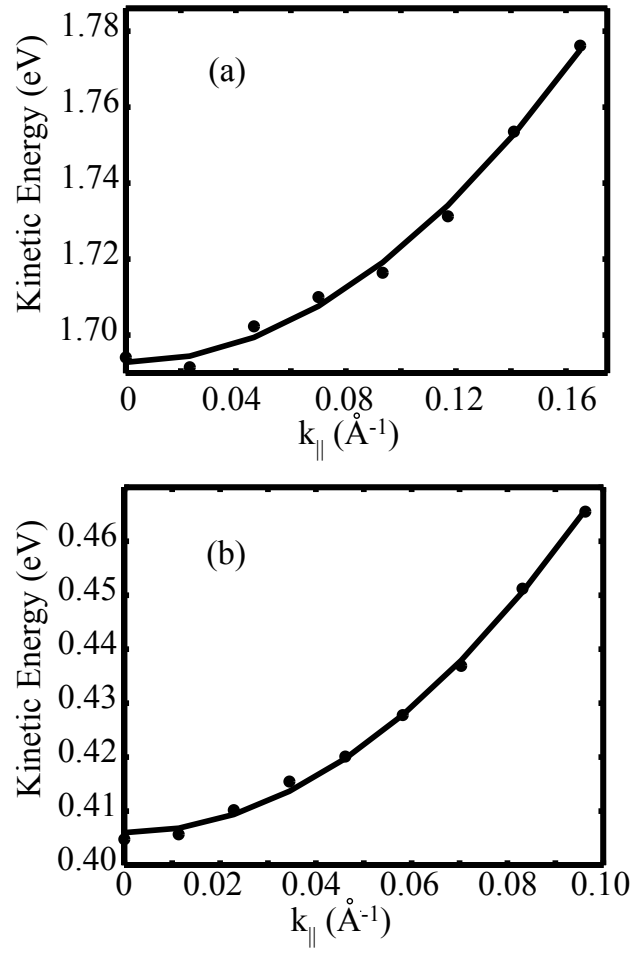


Figure 3.11: (a) The effective mass of the LUMO+1 at 2 ML is $0.58 m_e$ for $T_D = 300$ K. (b) The effective mass of $n = 1$ is $1.3 m_e$ for the same system.

3.4 Effective Masses

The effective masses of each intermediate state were dependent on layer morphology. Generally, the intermediate states in crystalline layers were more dispersive than in amorphous layers. The 2PPE spectra were collected at 140 K – 150 K, to minimize the possibility of temperature-dependent band effects. The effective mass for the conduction band is lowest when the layer is most crystalline, which can be achieved with a high T_D or by annealing at elevated temperatures (> 400 K). The effective mass at 2 ML ranges from $0.74 m_e$ for $T_D = 200$ K to $0.52 m_e$ for $T_D = 450$ K. Molecular overlap should decrease with increasingly thick layers due to epitaxial strain; this is reflected in the increasing LUMO+1 effective mass with thicker layers. For the LUMO+1 state at $T_D = 300$ K, at 2 ML thickness the effective mass is $0.58 m_e$ (figure 3.11a); $0.85 m_e$ at 4 ML; and $0.96 m_e$ at 6 ML thickness. The increase in effective mass matches expectations of lattice strain as bulk PTCDA begins to form on top of the initially commensurate layers. At lower temperatures, the effective mass is difficult to fit given the broadening at higher angles, but an estimate of the LUMO+1 is $3 m_e$ for $T_D = 140$ K at a 2 ML thickness.

The $n = 1$ IPS effective mass for 1 and 2 ML is $1.1 m_e$ for $T_D = 450$ K and increases slightly to $1.3 m_e$ at 4 ML. The $n = 1$ effective mass is nearly a free electron mass and does not interact significantly with a crystalline layer. This is also inferred from the constant binding energies, as discussed previously. An amorphous 1 ML surface at $T_D = 140$ K increases the effective mass of the $n = 1$ IPS to $2.4 m_e$ due to surface roughening; similarly, the $n = 1$ effective mass for $T_D = 300$ K is $1.3 m_e$ (figure 3.11b).

3.5 Lifetimes

A time delay between pump and probe pulses enabled the acquisition of dynamical information for each intermediate state. The decay times of each state were determined by finding the amplitude of each peak at each time delay and then fitting the peak amplitudes vs. time delay. The amplitudes of the IPS and LUMO+1 were fit to an exponential rise and decay, whereas the dynamics of the low kinetic energy scattering at low T_D could also be fit to a bi-exponential decay or a stretched exponential decay. The dynamical fits were

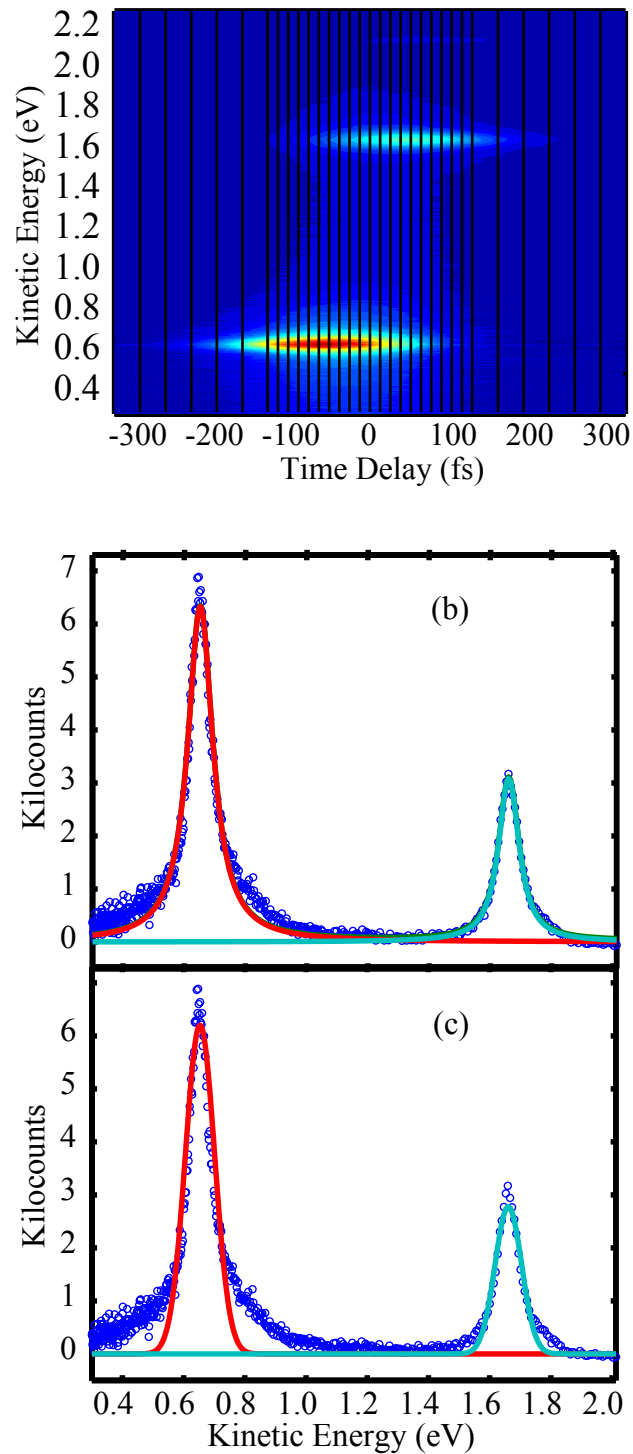


Figure 3.12: Each vertical line in the contour plot is a time slice corresponding to a 2PPE spectrum at a given time delay. The time delay is plotted with positive time indicating the probe pulse ($h\nu_2$) at a positive delay with respect to the pump pulse ($h\nu_1$). For 2 ML annealed at $T_D = 450$ K, the LUMO+1 is best fit to a Lorentzian (b) with a full width at half maximum of 90 meV, which can be converted to a lifetime or scattering time of 46 fs. The fit is better as a Lorentzian than a Gaussian lineshape (c), which suggests that the lifetime broadening is homogeneous.

T_D		2 ML	3 ML	4 ML	5 ML	6 ML	7 ML	8 ML
450 K	τ_R (fs)	31 ± 9	35 ± 14	50 ± 14	41 ± 10	40 ± 12	34 ± 17	38 ± 11
	τ_D (fs)	44 ± 10	43 ± 14	50 ± 14	41 ± 10	47 ± 10	48 ± 10	46 ± 10
300 K	τ_R (fs)	< 30	< 30	< 30	< 30	< 30	< 30	< 30
	τ_D (fs)	72 ± 39	73 ± 23	110 ± 22	131 ± 37	131 ± 43	143 ± 27	140 ± 43
200 K	τ_R (fs)	43 ± 18	< 30	< 30	< 30			
	τ_D (fs)	63 ± 16	89 ± 10	135 ± 51	194 ± 56			
140 K	τ_R (fs)	< 30	< 30					
	τ_D (fs)	37 ± 33	120 ± 59					

Table 3.2: Rise and decay constants for the LUMO+1 in a Stranski-Krastanov morphology were dominated by interaction with the wetting layer and stayed constant, but the decay constants for amorphous layer-by-layer growth increased dramatically. For all coverages, one monolayer dynamics could not be fit reliably due to weak dynamical signal.

convoluted with a Gaussian instrument function, typically on the order of 150 fs, which renders precise time constants for less than about 30 fs as physically meaningless.

The decay constants for the IPS were consistently less than the time resolution of our experiment. If an IPS electron is pushed away from the surface by increasing the layer thickness, the lifetime will increase because of the decreased overlap between the $n = 1$ IPS wavefunction and the silver surface. In *p*-xylene/Ag(111) layers, for example, the IPS decay constants for 1, 2, and 3 ML are 10, 40, and 1000 fs [9]. The short decay constant for the $n = 1$ IPS in coverages of crystalline PTCDA layers beyond 2 ML suggests decay predominantly influenced by interaction with the exposed 2 ML wetting layer, instead of decay through thicker PTCDA islands.

Comparing across morphologies, LUMO+1 lifetimes at thicker coverages were strongly anti-correlated with crystallinity. While crystalline systems exhibited little change in lifetimes with increasing coverage, decay constants for layers with lower T_D and rough surface morphology sharply increased (Table 3.2). For spectra for which the low kinetic energy manifold was present, the LUMO+1 was fit to a Lorentzian, and the manifold was fit to the tail end of a Lorentzian (figure 4.17). At thicker, amorphous coverages, however, separating the LUMO+1 from the low kinetic energy scattering proved intractable.

At $T_D = 200$ K, the decay constants of the low kinetic energy scattering exhibit bi-exponential behavior beginning at 4 ML (Table 3.3). For $T_D = 140$ K, the low kinetic

	4 ML	5 ML	6 ML	7 ML	8 ML
τ_{D_1} (fs)	86 ± 64	79 ± 32	158 ± 65	148 ± 49	203 ± 41
τ_{D_2} (ps)	2.5 ± 0.6	2.7 ± 1.2	10 ± 4	44 ± 4	30 ± 14

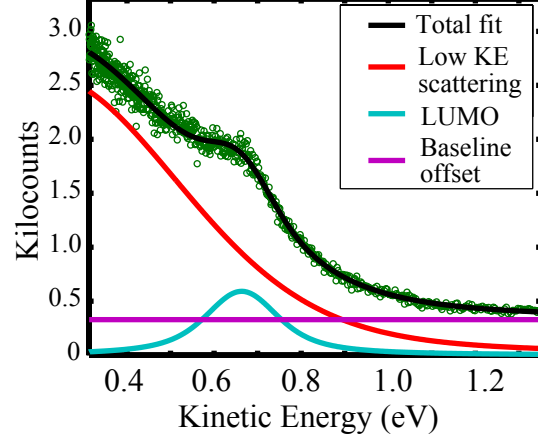
Table 3.3: The lifetimes of the low kinetic energy manifold at $T_D = 200$ K exhibit bi-exponential behavior from 4 – 8 ML.

energy scattering also exhibits bi-exponential decay beginning at 4 ML with an initial decay constant of 103 fs and a secondary decay constant of 1.6 ps (figure 3.13b). At 5 ML, the primary decay constant is 112 ± 55 fs, but the secondary decay constant increases to 5.6 ± 0.9 ps (figure 3.13c). For 6, 7, and 8 ML, the decay dynamics at $T_D = 140$ K are best fit to a stretched exponential, i.e., the Williams-Watts function, of the form:

$$A = A_0 e^{-\left(\frac{t}{\tau_W}\right)^\beta}, \quad (3.2)$$

where $0 < \beta \leq 1$ and τ_W is analogous (but not equivalent) to τ_D . A stretched exponential can be interpreted as a superposition of exponential decays, in which case a lower β suggests an increasingly broad range of decay constants [67]. For 6, 7, and 8 ML, β is 0.17, 0.16, and 0.12, respectively. In an amorphous layer with many local environments, a broad distribution is to be expected, and the observed trend in β is toward a wider distribution as the layer thickness increases, although I hesitate to place any greater physical significance on β .

For ultrathin films, shorter lifetimes result from proximity to the metal and high carrier mobility leading into the metal through the stacking direction. At low dosing temperatures, lattice mismatch reduces the conductivity back to the surface, and the layer-by-layer growth quickly increases the distance from the surface as well. Photoluminescence studies of bulk coverages report fluorescence decays for PTCDA bulk states on the order of 10 ns [60]. In the normal direction, anisotropy due to the herringbone structure leads to two different decay behaviors in time-resolved luminescence studies, on femtosecond and picosecond time scales [68]. For Stranski-Krastanov growth, crystallite growth leaves the 2 ML wetting layer exposed, which accounts for the similarity in lifetimes beyond 2 ML for high temperature growth modes. Gebauer et al. reported luminescence quenching of PTCDA on Ag(111) below two monolayers, after which photoluminescence increases quickly. The quenching is attributed to effective non-radiative processes including charge delocalization



(a) Low kinetic energy manifold.

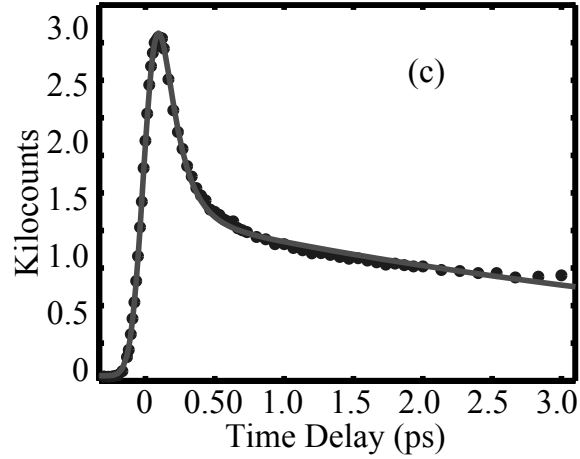
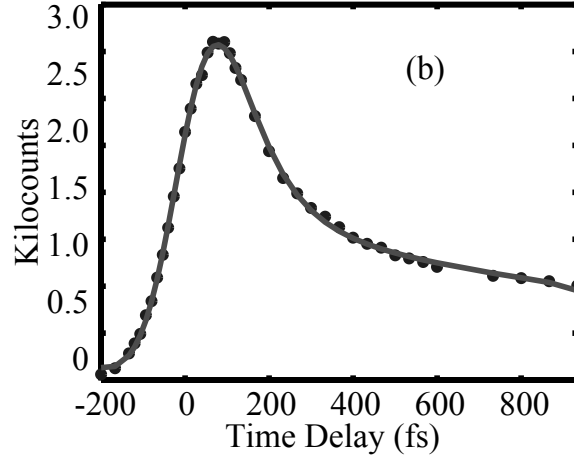


Figure 3.13: (a) The long-lived time dynamics of the low kinetic energy manifold could be calculated by fitting the manifold to the tail end of a Lorentzian, in addition to fitting the LUMO+1 peak to a Lorentzian. (b) For 4 ML at $T_D = 140$ K, the manifold exhibited bi-exponential decay dynamics, with $\tau_1 = 103$ fs and $\tau_2 = 1.6$ ps. (c) For 5 ML, the manifold decay increased to $\tau_1 = 1212 \pm 55$ fs and $\tau_2 = 5.6 \pm 0.9$ ps.

and tunnelling [47].

At $T_D = 440$ K, by 20 ML PTCDA crystallites are sufficiently large and dense enough to cover the wetting layer, or at least to suppress signal from the wetting layer, and the LUMO state is essentially constant on the femtosecond time scale, i.e., its decay constant must be at least tens of picoseconds. Not surprisingly, layers grown at low T_D reach unmeasurable dynamics (> 100 ps) much sooner, by 12 ML for a 140 K layer. To test the validity of lattice mismatch reducing decay pathways to the surface, PTCDA films were dosed for 7 ML at 440 K and followed by 3 ML at 300 K, and also 4 ML at 400 K followed by 3 ML at 300 K. The rise times were negligible, and the decay constants for the LUMO-derived peak for each layer were 79 fs for the 10 ML total and 218 fs for the 7 ML total.

3.6 Implications for Charge Transport Measurements

As shown above, both the band structure and dynamics of organic ultrathin films can depend critically on their morphological properties. To demonstrate the importance of this, consider the transport properties of PTCDA. Since the electronic structure of PTCDA strongly retains its intramolecular character, a nearest neighbor tight-binding approximation provides insight into its steady state transport properties. In a tight-binding model, the dispersion relation is given by:

$$E(k_{\parallel}) = E_0 - 2t \cos(k_{\parallel}a), \quad (3.3)$$

where t is the transfer integral and a is the lattice-spacing. Re-writing the effective mass as

$$\frac{1}{m^*} = \frac{1}{\hbar^2} \frac{d^2 E}{dk^2}, \quad (3.4)$$

in the limit of small k_{\parallel} it can be shown that [69]:

$$t = \frac{\hbar^2}{2a^2 m^*}. \quad (3.5)$$

This assumes that the surface band structure can be modelled with a cosine band and has a minimum at the $\bar{\Gamma}$ point, which is true for the rectangular lattice of PTCDA on Ag(111) [40]. Equation 3.3 has been used successfully in previous organic electronics systems including pentacene [70] and bis(1,2,5-thiadiazolo)-p-quinobis(1,3-dithiole) (BTQBT) [69],

as well as k_{\perp} for PTCDA layers on MoS₂ [49]. As a measure of orbital overlap in crystalline layers, the transfer integral t from Eq.(3.5) is 25 meV using an effective mass of $0.52 m_e$ and 14 meV using an effective mass of $0.96 m_e$. We use an averaged lattice constant of 17 Å since our experiment measures several orientations of the rectangular lattice.

Measurements of decay time and effective mass also affect estimates of charge mobility μ , where

$$\mu = \frac{e\tau}{m^*}. \quad (3.6)$$

The time constant τ reflects the momentum relaxation time of charge carriers through scattering processes including phonon, surface, and defect interactions, as well as non-radiative decay back into the metal. Intraband relaxation has been observed for image potential states in a variety of systems via 2PPE [9, 71], but in PTCDA, electrons decay into the metal too quickly to measure intraband relaxation (figure 3.14). To estimate τ , the LUMO+1 at 2 ML was fit to a Lorentzian (figure 3.12) which resulted in a FWHM of 90 meV, corresponding to a time constant of 46 fs. In combination with equation 3.6 and an effective mass of $0.52 m_e$, a mobility value of $160 \frac{cm^2}{V \cdot s}$ is obtained at the interface. Generally, a linewidth is additive of all the scattering processes in a system, and so this mobility should be considered a lower bound since decay into the metal should dominate the linewidth. Ostrick et al. [48] measured electronic transport using a FET geometry along the planar direction of thin films of PTCDA, with values of carrier mobilities in the range from $10^{-5} - 10^{-4} \frac{cm^2}{V \cdot s}$. The FET experiments were composed of PTCDA layers with thicknesses of 150 nm, which is roughly 50 monolayers, and the layers were measured and therefore annealed at temperatures up to 340 K. At this coverage, the charge transport is expected to be that of a bulk molecular crystal, and the carriers are strongly coupled to the lattice, e.g., polaronic hopping transport, which contrasts sharply with the free charge carrier we observe in interfacial layers. Transport through the normal direction is p-type, and as a point of comparison, hole mobility in the perpendicular direction is $> 3.8 \frac{cm^2}{V \cdot s}$ with an effective mass of $m_h = 5.28 m_e$ [49]. This corresponds to a carrier relaxation time of 11 fs.

In accordance with a localized carrier picture, Ostrick et al. observed temperature-dependent mobilities. Hopping mechanisms are generally attributed to polarons, but we see no evidence for lattice polaron formation in ultrathin layers of PTCDA. Ge et al. mea-

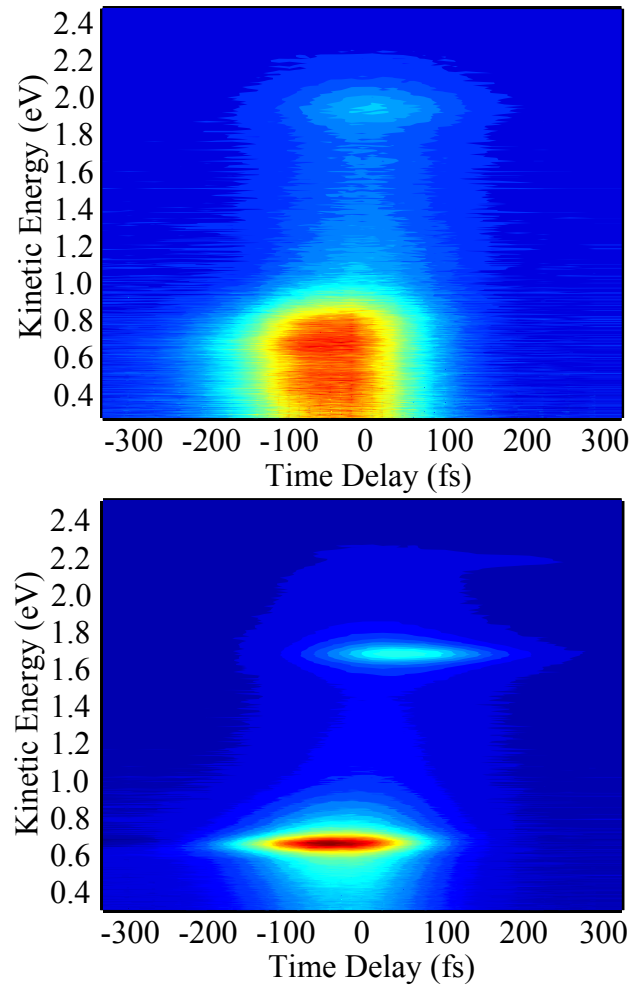


Figure 3.14: The contour plots compare the time dynamics of 3 ML of PTCDA with $T_D = 450$ K. The bottom figure was obtained at 0° , and the top was obtained at 24° . The similarity in dynamics for both the LUMO+1 and the higher energy $n = 1$ IPS indicate that intraband relaxation is not observable at this time scale.

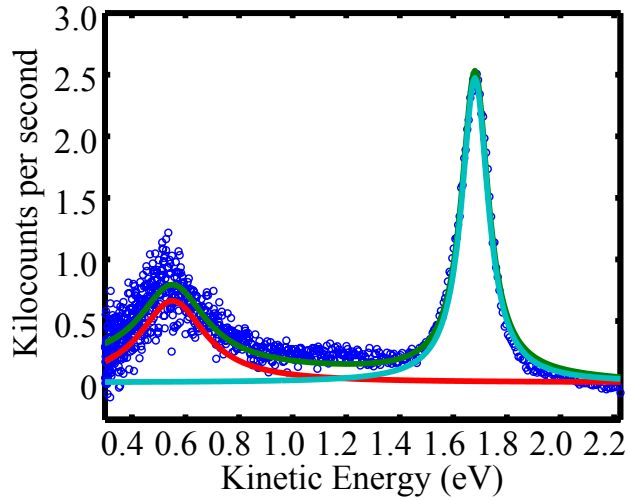


Figure 3.15: At 320 K, the LUMO+1 of a layer dosed at 450 K has a FWHM of 290 meV.

sured the formation within a few hundred femtoseconds of localized polarons in alkane layers on Ag(111) [7]. Additionally, Miller observes a shift in energy as the polar layer solvates and localizes an excited electron [72], as do Gahl et al. for H₂O and D₂O layers [73]. No solvation or dynamic localization is observed in PTCDA from 0 fs – 4 ps, nor a shift in effective mass over time (figure 3.14) or over a range of temperatures from 140 K – 450 K. Therefore a transport mechanism based on lattice or molecular polarons, at least within the planar direction, is precluded at this interface in favor of free charge carrier transport. Free charge carriers decrease mobility at higher temperatures due to higher rates of phonon scattering; an attempt to fit a 2 ML, $T_D = 450$ K spectrum taken at 320 K to a Lorentzian lineshape resulted in a FWHM of 290 meV, which corresponds to a 14 fs relaxation time and a mobility of $24 \frac{\text{cm}^2}{\text{V}\cdot\text{s}}$ (figure 3.15). No solvation or dynamic localization exist for the image potential states as well.

3.7 Future work

An interesting project would be modelling the energetic barriers to decay back into the model. For example, in an amorphous $T_D = 200$ K layer, we can assume that a scattering event in the perpendicular direction is caused by the adjacent layer. Using a simple model

where all electrons begin in the fifth monolayer and have equal chances of moving toward the metal or moving away from the metal, a decay time of 194 fs corresponds roughly to a layer-by-layer scattering time of 8 fs. This simplistic model assumes constant barrier heights, and so it would be instructive to vary barrier heights and electronic distribution to re-create charge transfer back to the metal on the order of 30 ps.

3.8 Conclusion

Angle-resolved 2PPE spectra were collected of different morphologies and thicknesses of PTCDA on Ag(111). The morphology of the layer was found to affect the workfunction of each thin film interface and subsequent convergence to bulk PTCDA values, while the vacuum level was a function of thickness only. An initial increase in the vacuum level with the first monolayer was attributed to negative charge transfer into the metal, which was partly mitigated by the second monolayer. Effective masses were also dependent on morphology, with higher effective masses reflecting lower crystallinity. Finally, 2PPE enabled the study of electron dynamics at the PTCDA interface. Exposure to a wetting layer limited the lifetimes of electrons in crystalline layers despite high coverages of PTCDA, while amorphous layer-by-layer growth increased electron lifetimes from femtoseconds to picoseconds within a few layers. The aforementioned differences in electronic properties due to morphology emphasize the necessity of understanding interfacial structure, and attempts to build molecular devices should properly include morphological considerations in thin film engineering.

Chapter 4

Oligothiophenes

4.1 Overview

Oligothiophenes have emerged as one of the largest classes of organic molecules studied for device applications. Polythiophenes and functionalized thiophenes have been used to create devices with increasing efficiency and offer the promise of flexible and printed circuits [74–76]. Like most organic semiconductors, oligothiophenes and their functionalized derivatives are p-type semiconductors with hole transport perpendicular to the long axis, although some functionalized thiophenes show n-type behavior with mobilities of $0.02 \frac{\text{cm}^2}{\text{Vs}}$ [77]. Oligothiophenes can be functionalized to improve their solubility, so that they may be processed in solution [78]. Useful as models of longer polymers, oligothiophenes are easier to grow in crystalline structures than their parent polymers.

A comprehensive array of research is devoted to thiophenes. A few representative examples are included herein. Tuning morphologies of sexithiophene with different functional groups and on different substrates has been studied both in theory and experiment [79]. Thiophenes mixed with n-type organic semiconductors have been used to make organic solar cells. Yang et al. studied PCBM ([6,6]-phenyl-C61-butyric acid methyl ester) and P3HT (poly-3-hexylthiophene) heterojunctions, where thermal annealing causes nanowires to penetrate crystalline PCBM film [80]. Mixing with a solvent can increase mobility and charge absorption as well [81]. Semiconductor nanorod and P3HT-based solar cells have also been fabricated [82].

The interest in studying interfaces and ultrathin films is motivated by studies of hole mobility as function of coverage, with the result that mobility saturates by 2 ML in α -6T [22]. While 2PPE is an electron injecting process, the point still holds that an interface is the most crucial region for charge accumulation. Higher layers have negligible carrier density or smaller domains [83]. In addition, the local interfacial structure has been shown to affect charge mobility at oligomer-insulator interfaces [84]. Polymorphism in oligothiophenes with either 2 or 4 molecules per unit cell has been observed in quaterthiophene (4T) and sexithiophene (6T), and is based on growth conditions including substrate temperature and Knudsen cell temperature [85]. Higher structural order in conjugated oligothiophenes has been tied to improved measurements in opto-electronic devices [78]. In fact, ionization energies of (functionalized) sexithiophenes can be changed by as much as 0.6 eV depending on whether it lies flat on the Ag(111) surface or stands upright. A physical picture for this is given by a surface dipole effect created by a negatively charged π -orbital plane above a positively charged molecular plane [86].

Oligothiophenes with 2, 3, and 4 monomer units have decreasing transition energies of triplet and singlet states with increasing chain length [87]. Fichou et al. have reported low temperature optical absorption of polycrystalline thin films of 4T, 6T, and 8T with a fundamental π - π^* absorption band ranging from 300 nm – 500 nm. The saturation in oscillator strength by 6T for this band is attributed to polyene behavior, i.e., full conjugation over the oligomer [88]. EELS was used to study optically allowed and forbidden electronic excitations of 6T thin films; a spatial size (mean radius) was estimated around 8 Å, i.e., spread out over finite length of oligomer. This evidence bolsters the argument for localized states being caused by structural relaxation, such as polarons or defect trap sites [89]. Charge transport in polymers can take the form of solitons, polarons, or bipolarons, depending on the chain structure and molecular ordering [90]; in thiophenes a polaron hopping mechanism is probably accurate [91], with localized charge carriers [92]. Exciton polarons are formed in polythiophene within 300 fs and decay in the nanosecond time domain; afterward, dominant excitations are charged polarons and bipolarons [93]. Size-dependent dynamics of oligothiophene were found using subpicosecond pump-probe spectroscopy, including triplet decay from fs to ps timescales [94]. Lanzani et al. [95] observe a photoinduced absorption state at 1.6 eV in thicker films, which they attribute to a charge-transfer

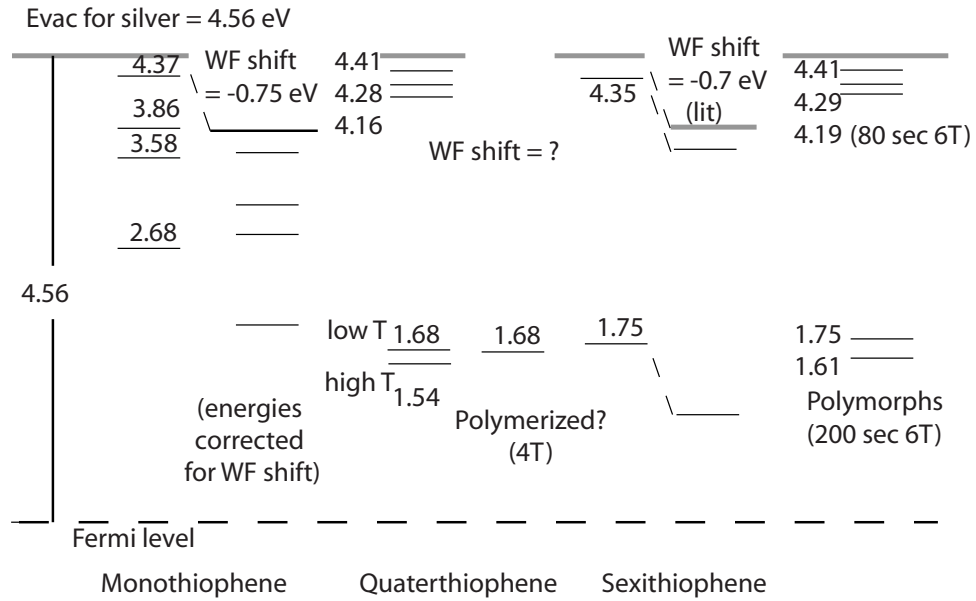


Figure 4.1: Energy level diagram of values for different thiophene interfaces. Energies are in eV and referenced to the Fermi level, $E - E_f$.

exciton and which is formed within 300 fs [95]. When a field is applied, field-dependent release times from localized states can affect field-dependent mobility [96].

4.2 Monothiophene

Monothiophene was dosed on the Ag(111) substrate via a variable leak valve. 1.5 Langmuir (15 seconds, 10^{-7} torr) was sufficient to dose the planar monolayer as long as the crystal was below 170 K, and the dense monolayer was grown by dosing for 40 seconds at 10^{-7} torr followed by annealing at 138 K. Degradation in MCP detector performance may have been tied to monothiophene exposure, which was therefore minimized as much as possible. The first monolayer of thiophene undergoes a phase transition around 150 K from a planar geometry at higher temperatures to a tilted geometry at colder temperatures, with an average tilt angle from 41–45° [97]. On Pt(111), NEXAFS shows a thiophene phase change at 180 K, and the compressed phase is present at 150 K [98]. In the same report, the thiophene ring plane is given as about 40° from surface, and C-S bond cleavage begins at 290 K and is completed by 470 K. Using TPD, the compressed monolayer desorbs

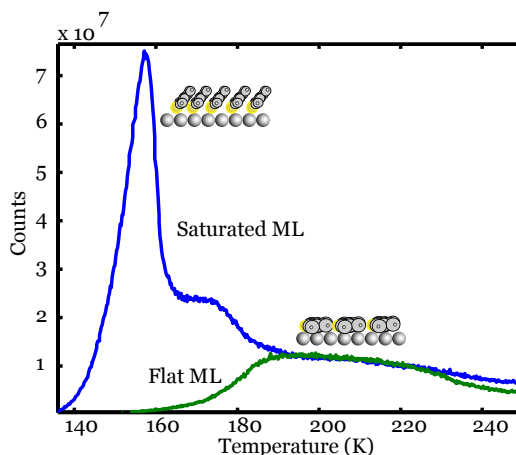
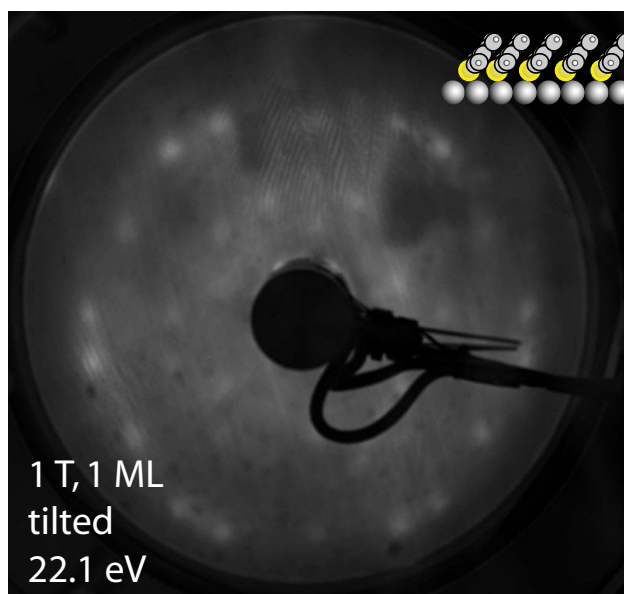


Figure 4.2: TPD spectra of 1 ML thiophene. The saturated monolayer was dosed at 133 K, while the planar monolayer was dosed at 160 K.

around 157 K, and the planar monolayer at 180 K (figure 4.2); qualitatively, this matches literature TPD spectra [97, 99]. The shoulder from 160 K – 170 K is attributed to a mixed phase coverage. Both the planar and dense geometries exhibit surface order, as evidenced by LEED (figure 4.3), and the planar geometry appears more ordered and with a larger unit cell. Chen et al. observe an ordered $c(2\sqrt{3} \times 4)$ rect structure in their lowest coverage of monothiophene on Ag(111), followed by a complex $(2\sqrt{7} \times 2\sqrt{7})$ ordered overlayer. In their saturated coverage, they observe a herringbone structure [100]. However, their reported exposure times of <40 L, 90 L, and 150 L, resp., are far greater than what I used experimentally and also significantly greater than what one would expect from a molecule with near unit sticking probability at cold temperatures (120 K in the reference). Due to a lack of liquid helium, I was unable to dose the multilayer.

The 2PPE spectra for each phase are presented in figure 4.4, and an energy level diagram organizes the peak energies in figure 4.1. The wavelength I used was 632 nm, below which I saw one-photon photoemission. The planar monolayer exhibits the $n = 1$ and $n = 2$ image states, and also a vis-probed molecular state and a uv-probed molecular state. The binding energies of the image states are 0.69 ± 0.10 eV and 0.19 ± 0.10 eV for the $n = 1$ and $n = 2$ states, respectively, which corresponds to a quantum defect of 0.11. This value of the quantum defect is similar to other planar aromatic hydrocarbons [12]. The low kinetic energy shoulder has a binding energy of 0.98 eV, and the small feature present in both uv-

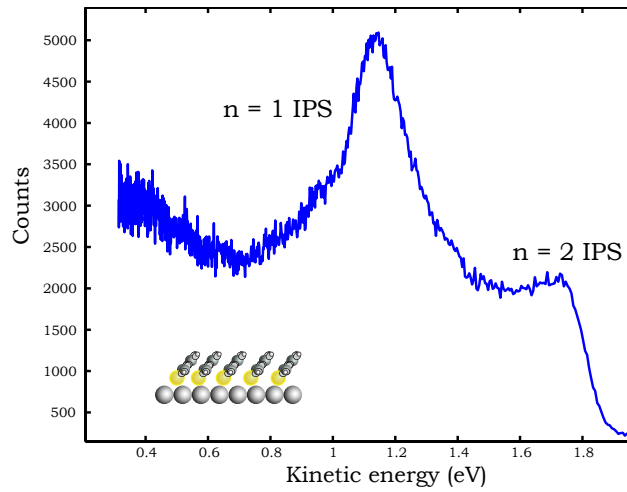


(a) Tilted monolayer LEED

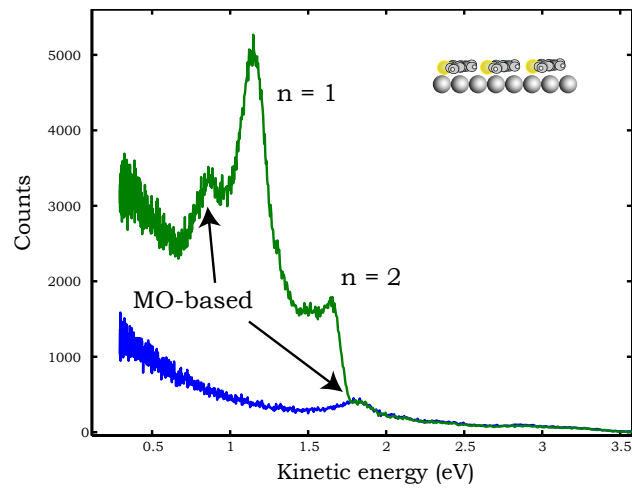


(b) Planar monolayer LEED

Figure 4.3: (a) LEED of the tilted monolayer of monothiophene, at 22.1 eV, and (b) of the planar monolayer, at 16.2 eV.



(a) Tilted monolayer 2PPE



(b) Planar monolayer 2PPE

Figure 4.4: (a) 2PPE spectrum of 1 ML thiophene in its dense phase. The planar phase (b) exhibits what are probably the $n = 1$ and $n = 2$ IPS and two molecular-orbital based states.

uv and uv-vis spectra has a binding energy of 1.88 ± 0.10 eV. The effective mass for $n = 1$ is $1.0 m_e$ and for the LUMO+1 is $0.95 m_e$. From the vacuum level shift obtained by fitting the image states, the workfunction shift is -0.75 eV, so that the workfunction is 3.81 eV, using 4.56 eV as the clean silver workfunction. The difference in workfunction from optical determination via 1PPE can be attributed to uncertainty in the clean silver workfunction. Referenced to the Fermi level E_F using:

$$E - E_F = \Phi - h\nu + KE, \quad (4.1)$$

the energies of the $n = 1$ and $n = 2$ IPS and the molecular states are 3.86 eV, 4.37 eV, 3.58 eV, and 2.68 eV, resp. The effective mass is $0.9 m_e$ for the molecular state at 3.58 eV and 1.1 for the $n = 1$ IPS. If the lowest lying transition energies are 3.7 eV and 4.6 eV, from $\pi - \pi^*$ transitions, then the molecular orbitals could originate from the same valence band around 7.28 eV, close to one of the valence bands (~ 7 eV) in the work of Palmer et al [101]. Identifying the states with no uncertainty, however, is still a work in progress.

In the tilted monolayer, a peak at 0.78 eV binding energy is present, with an effective mass of $1.4 m_e$. This peak is assigned to the $n = 1$ IPS. The difference in spectra between the planar and dense monolayers is attributed to the planar geometry and surface normal orientation of the $\pi - \pi^*$ transition, and subsequent (mis)alignment of the thiophene transition dipole.

4.3 Quaterthiophene

4.3.1 Material properties

α -4T was obtained from Sigma-Aldrich. Literature diagrams of α -4T, not to mention Sigma's website itself, are inconsistent with isomer geometries, in that the molecule may be linear or curved (figure 4.5). The linear oligomer is possible to synthesize, while the curved isomer is what Sigma-Aldrich makes commercially available, according to the structure on Sigma-Aldrich's main quaterthiophene webpage. The linear structure is visible on a webpage for conductive thiophene oligomers; while quaterthiophene is linear on that page, the link leads back to the main quaterthiophene page and therefore the curved structure. My

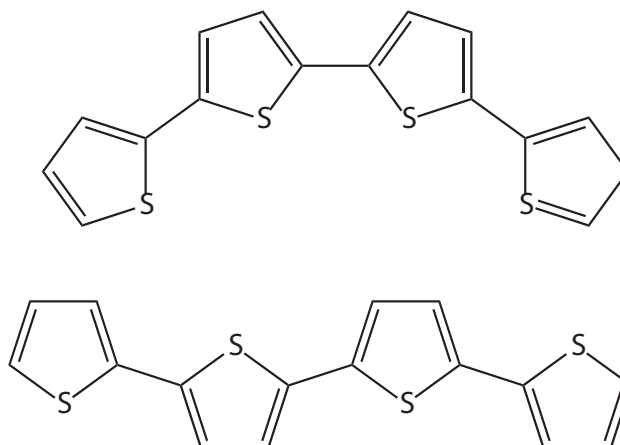
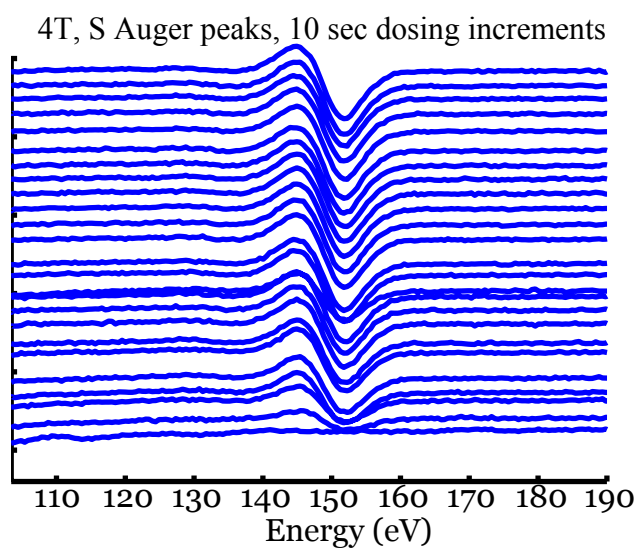


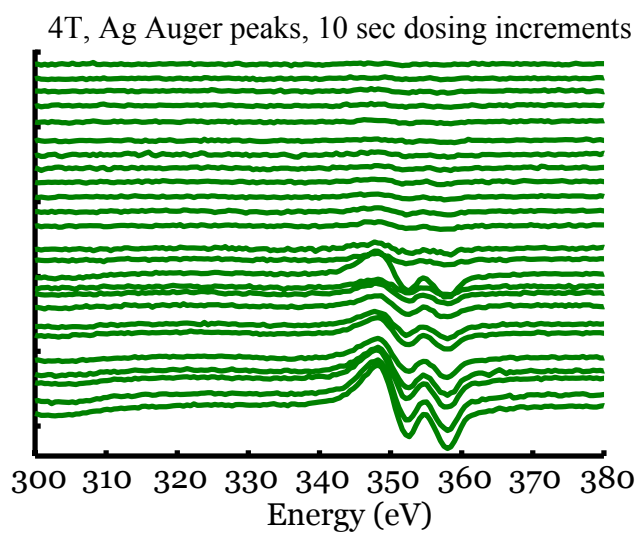
Figure 4.5: The conformer of quaterthiophene that was dosed on the surface is unclear.

source for the quaterthiophene was Sigma-Aldrich, and the rotational barrier around the C-C bond is estimated to be 40 meV – 150 meV, depending on the basis set used in DFT calculations [102]. The temperatures for the effusion cell were 150 °C and 160 °C, and the possibility that the conformation changed while dosing cannot be ruled out. Presumably, any changes in conformation would lead to the thermodynamically most stable, i.e., the linear conformer. In addition, changing the effusion cell temperature and therefore the rate at which quaterthiophene is dosed also changes the domains on the substrate [103].

Using TPD results, Soukopp et al. find a multilayer stage that grows in below 360 K, a bilayer or 2nd monolayer below 380 K, and atomic desorption above 550 K. The flat-lying, first monolayer is commensurate and ordered, and further multilayers become more strained and lose their epitaxial growth [104]. Later studies from Li et al. found multilayer desorption above 345 K but no bilayer desorption or molecular degradation [105]. According to Li, the planar molecule remains predominantly parallel even in crystalline bulk structure (> 30 ML), although the molecules undergo some twisting. Nucleation rates and island densities were studied with AFM and Reflectance Anisotropy Spectroscopy (RAS) by Sassella et al., with the results that high deposition rates and/or low substrate temperatures increased the nucleation rate and island density [106]. Seidel et al. also observed long-range order using LEED and STM of end-capped quaterthiophene (EC4T) on Ag(111) due to two different monolayer phases [107].



(a) Sulfur growing in.



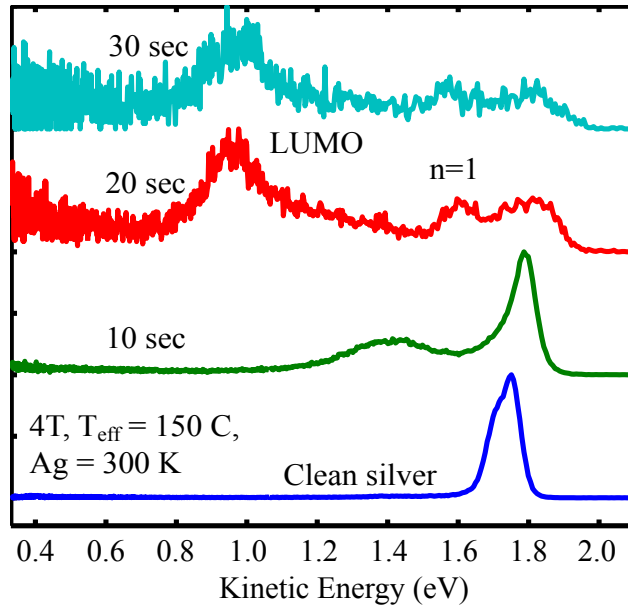
(b) Extinguished silver peaks.

Figure 4.6: Auger dosing survey of quaterthiophene. Each dosing increment was 10 seconds of quaterthiophene, with the substrate held at room temperature and the Knudsen cell at 150 °C.

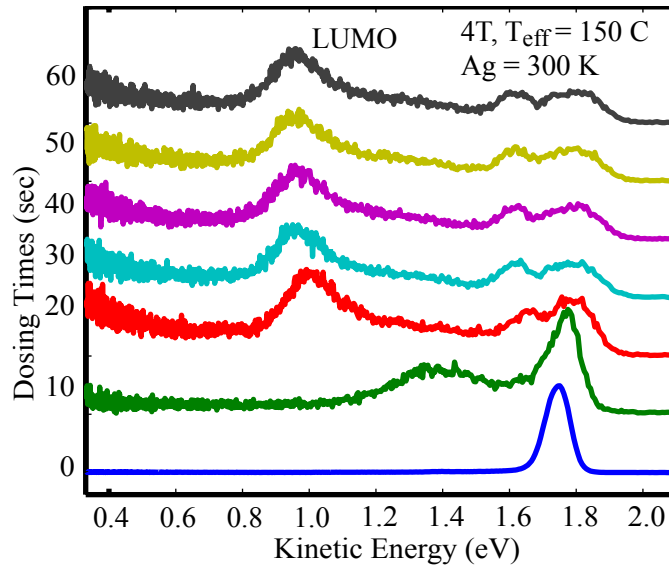
Dosing with 2PPE can often be calibrated by following the layer-by-layer evolution of the electronic structure, such as for PTCDA. Since this behavior was not present for quaterthiophene, a combination of 2PPE and Auger Electron Spectroscopy was used to estimate monolayer coverages. In figure 4.6, Auger of sulfur and silver Auger peaks were taken after ten second increments, with a room temperature substrate for both dosing and data collection and the crucible at 150 °C. Silver Auger peaks disappear after eighty seconds of dosing, or 2 ML, which corresponds to an electron escape depth of 7 Å. The appearance of sulfur Auger peaks and concomitant disappearance of silver peaks were correlated with a 2PPE dosing survey. According to the 2PPE dosing survey, a full monolayer, judged by no further change in the spectra, is evident by four, ten-second doses with the crucible held at 150 °C (figure 4.7). In figure 4.7a, 2PPE electronic structure saturates after 30 – 40 seconds, at the same growth conditions as the Auger spectra. Saturation of electronic structure is not enough to identify film thicknesses, but using literature values for known 1 ML sticking temperatures I could calibrate the dosing survey further. In figure 4.7b, 2PPE structure saturates after 40 seconds, but here the substrate temperature is held at 400 K. At this temperature, only 1 ML should stick to the surface, and therefore the saturation of electronic structure can be calibrated to the formation of one monolayer.

Quaterthiophene was dosed at two different crucible temperatures and several substrate temperatures. With the substrate at room temperature, crucible temperatures of 150 °C and 160 °C showed little difference in 2PPE spectra. Probably the crucible should be at 140 °C to grow the low-temperature polymorph with complete certainty. Varying the substrate temperature, and presumably the thin film morphology, while dosing led to more interesting results; substrate dosing temperatures of 210 K, room temperature, and 400 K exhibited markedly different behavior with changes in energies (figure 4.11) and effective masses.

Temperatures above 380 K should lead to a flat one monolayer coverage (figure 4.7). No changes in spectra occurred for further dosing after 40 seconds of quaterthiophene on a substrate held at 400 K. An experiment to try in the future would be to hold the substrate between 360 – 380 K to grow the bilayer, which could correlate the electronic behavior in the bilayer with the dense monolayer in monothiophene. In figure 4.9, dispersions of a 200 K domain layer and of a 400 K domain layer are presented. The binding energies are



(a) 2PPE dosing stackplot.



(b) One monolayer growing in.

Figure 4.7: (a) 2PPE stackplot of 10 second increments of 4T, with an effusion cell temperature of 150 °C and substrate dosing temperature of 300 K. (b) Comparison of 10 second increments of 4T, with same conditions as above except a substrate dosing temperature of 400 K. After 40 seconds or so, which is about 1 ML, no more 4T should stick to the surface. The spectra were collected at room temperature.

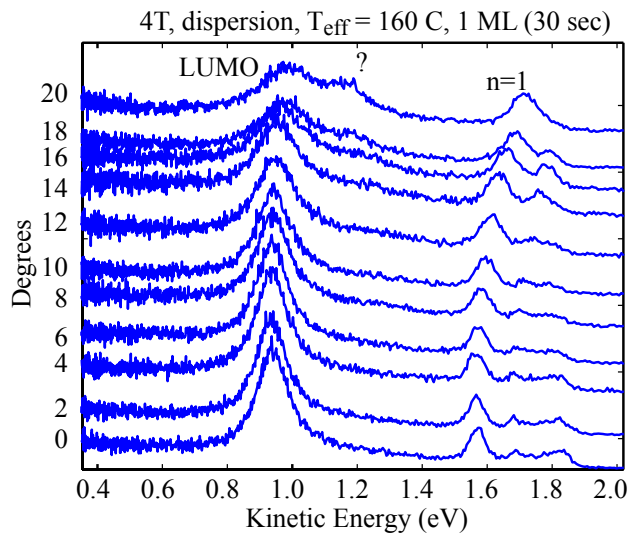
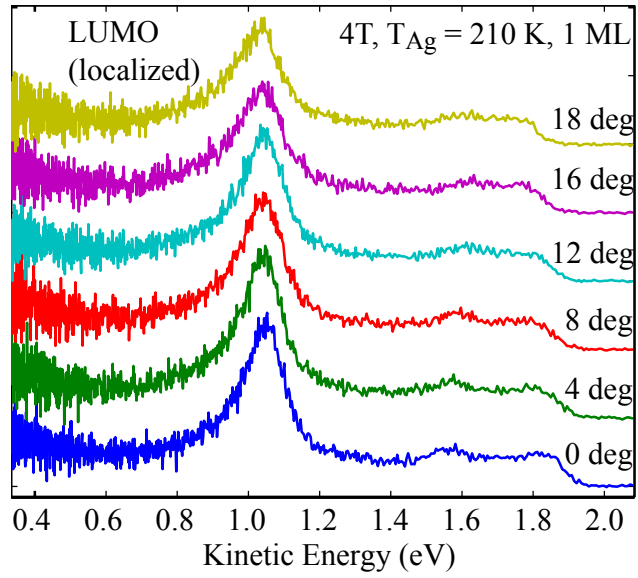


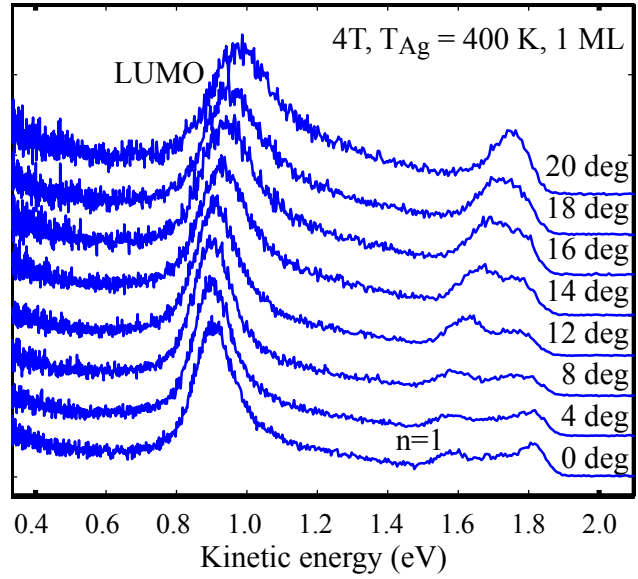
Figure 4.8: Dispersion of layer with $T_{eff} = 160\text{ }^{\circ}\text{C}$, 30 seconds of 4T.

unclear due to a lack of a wavelength survey, but the uv-uv data indicate that the first, low kinetic energy peak is uv-probed (figure 4.10). In the uv-uv data, a lack of a uv-uv peak corresponding to the uv-vis peak with an additional unit of photon energy suggests that the localized peak is (only) uv-probed. Also, a peak is visible at the same energy as in the uv-vis spectra, albeit with lower amplitude. Such behavior can be explained by a resonant visible photon pump energy that increases the population of the intermediate state in the uv-vis spectra. However, lacking a wavelength survey, both uv-vis and uv-uv energies are reported.

A comparison of 2PPE spectra of several polymorphs is presented in figure 4.11. In the polymorph grown with a crucible temperature of $150\text{ }^{\circ}\text{C}$ and a substrate dosing temperature of 300 K, the binding energies are 1.03 eV, 0.40 eV, 0.28 eV, and 0.15 eV. Referenced to the Fermi level, the binding energies are 3.53 eV, 4.16 eV, 4.28 eV, and 4.41 eV. If the largest peak is uv-probed, as the uv-uv background suggests, then its binding energy is 1.57 eV referenced to the Fermi level (or 2.99 eV with respect to the vacuum). In the 1 ML film grown at 400 K, peak A of figure 4.10 is at 1.06 eV binding energy, or 3.02 eV if uv-pumped, with respect to the vacuum level and 3.50 eV or 1.54 eV with respect to the Fermi level. In the film grown at 210 K, peak A is shifted to higher energies and has binding energies of 0.92 eV (uv-vis) or 2.88 (uv-uv) eV with respect to the vacuum level



(a) 210 K dispersion

Figure 4.9: Dispersions of a layer grown at $T_{Ag} = 210$ K and at $T_{Ag} = 400$ K.

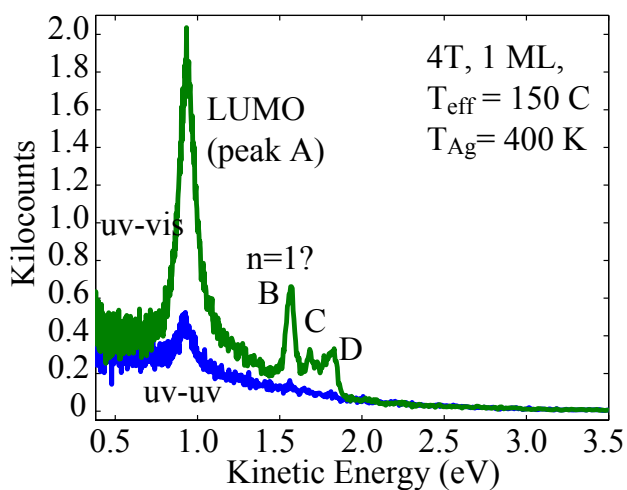


Figure 4.10: In a comparison of uv-uv and uv-vis spectra, peak A has no analogue in the uv-uv spectrum that might result from a uv-probe if it were vis-probed in the uv-vis spectra. This suggests that peak A is always uv-probed. The visible photon energy was 1.96 eV.

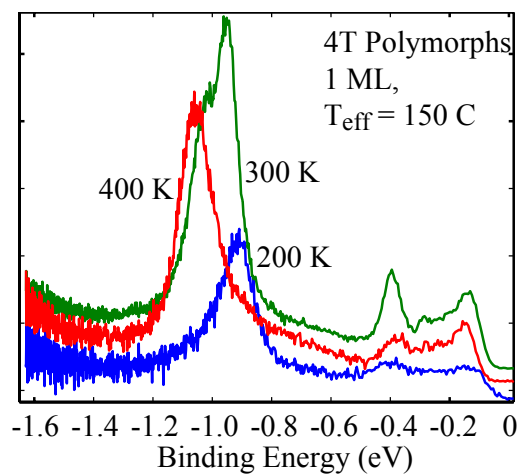
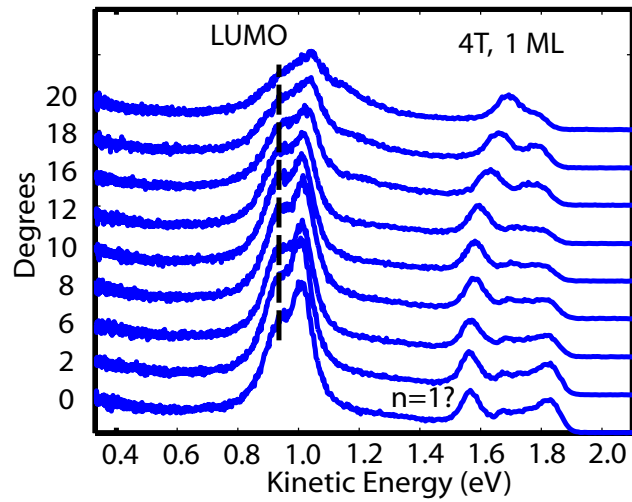


Figure 4.11: Comparison of 2PPE spectra for different polymorphs; all spectra were collected at 140 K.

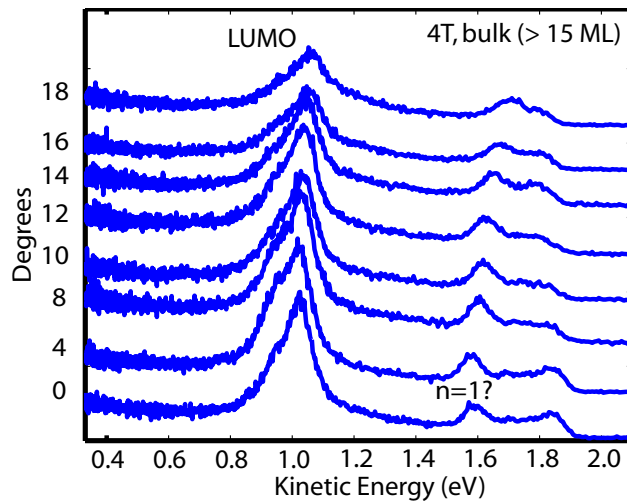
and 3.64 eV or 1.68 eV referenced to the Fermi level. HREELS data indicate an energy gap of around 2.6 eV [108]. Typical absorption spectra of 4T films deposited on two different substrates show the same main absorption peak at about 3.67 eV which can be attributed to the first $\pi - \pi^*$ transition whose dipole is aligned along the long molecular axis [109].

The fine structure at higher energies may be due to misaligned molecules or small islands of molecules [110]. While these peaks are in the appropriate energy range for image potential states, what remains problematic is that the peaks do not disappear after dosing for what should be bulk film measurements (figure 4.12). However, if they are not image states, then the question remains why image states are not visible. Possibly the peaks are image states, and they persist because of islanding effects which leave thinner layers exposed. Another hypothesis is that the image states might be screened due to high polarizability in thiophene layers, or a positive electron affinity captures injected electrons into molecular states. Regardless, a high degree of uncertainty is associated with the origin of these peaks. In figure 4.11, the 2PPE spectra for 210 K, 300 K, and 400 K are overlaid. The energy alignments indicate that at room temperature, two phases of quaterthiophene are present. The amplitudes do not match, but this is probably due to different laser powers and other experimental conditions.

Photoluminescence measurements of temperature-dependent exciton dispersion in α -4T films on highly oriented pyrolytic graphite and Ag(111) suggest an upward-bending exciton band [47]. Siegrist et al. modelled unoccupied and occupied band structure for quaterthiophene, using extended Hückel calculations (EHT) [103]. Mapping the band structure from 2PPE to Siegrist's work would be possible with better energy resolution, e.g., if the spectra were taken at colder temperatures. The effective masses are given in table 4.1. The LUMO state is localized at low temperature coverages, and dispersive in one monolayer of higher temperature coverages. This could be caused by local defects within the layer, which matches the observation of static localization. Nevertheless, from the LEED images, the low temperature layer is overall fairly crystalline. In figure 4.16, data fits to 0, 12 and 20 degree scans of a layer grown at room temperature and where the data were collected at 140 K reinforce that the LUMO in a layer grown at room temperature can be fit to offset peaks. The origin of the higher energy shoulder of the LUMO at 20 degrees is unclear (figure 4.17).



(a) One ML dispersion



(b) Bulk dispersion

Figure 4.12: Dispersion of 150 °C layer, 30 seconds (top) and 630 seconds (bulk). The dashed line is a guide to the eye indicating the position of the localized shoulder.

Layer	Peak			
	A	B	C	D
1 ML, 400 K	0.90	1.5	1.1	?
bulk, 300 K	2.5	1.3	1.4	?
1 ML, 300 K	5.7 (low T)	1.5	?	?
	4.4 (high T)			
1 ML, 210 K	localized	1.6	?	?

Table 4.1: Effective masses in units of m_e for quaterthiophene.

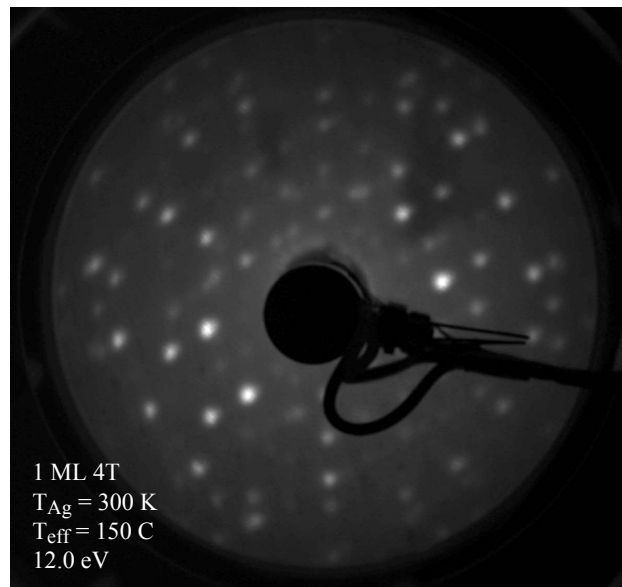


Figure 4.13: LEED, 4T, 12.0 eV, $T_D = 300$ K.

4.3.2 LEED

A comparison of LEED images indicates that the 400 K layer is most ordered and the 210 K layer is the least ordered. All three layers exhibit a fair amount of crystallinity. The room temperature layer is a combination of two domains, which probably correspond to the high-temperature and low-temperature polymorphs (with the understanding that the literature ascribes polymorphism to the effusion cell temperature and not substrate temperatures). In theory, if the room temperature layer is composed of mixed domains of LT and HT growth, it should be possible to deconvolute the LEED image. An added complication is the multiple orientations of each domain.

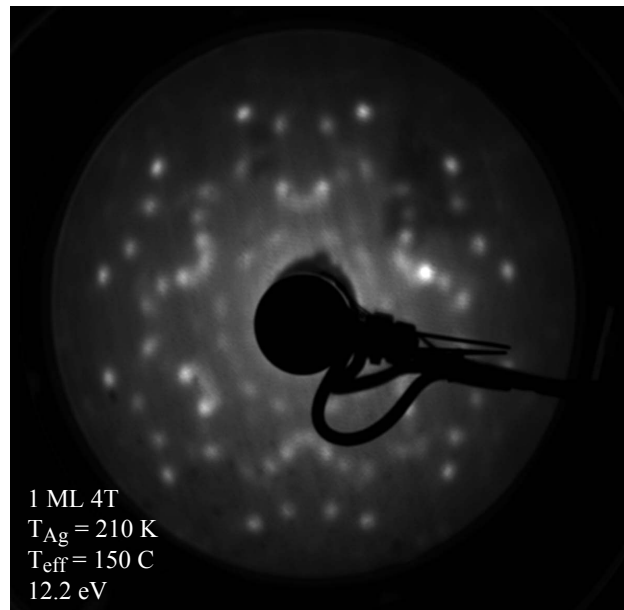


Figure 4.14: LEED, 4T, 12.2 eV, $T_D = 210\text{ K}$.

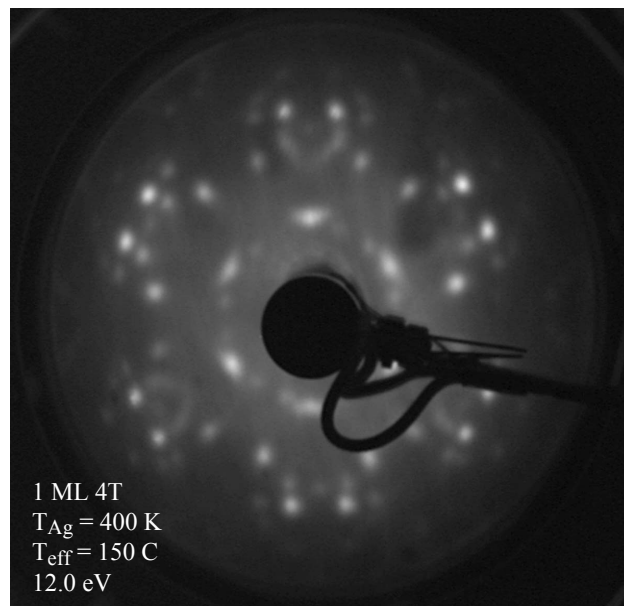


Figure 4.15: LEED, 4T, 12.4 eV, $T_D = 400\text{ K}$.

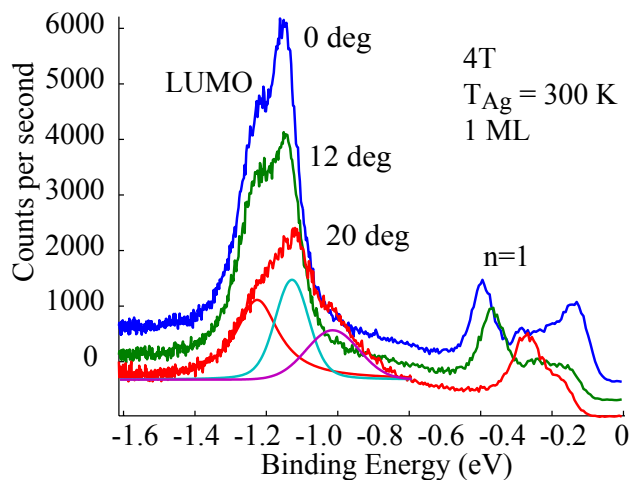


Figure 4.16: Comparison of 0, 12, and 20 deg 2PPE scans, with data fits for the 20 deg spectrum, for the morphology of a room temperature-grown layer.

4.3.3 Laser instability

After a few experiments, I was able to attribute inconsistent data to laser-induced changes in the layer (figure 4.18). As a result, before each scan I moved the laser spot a millimeter or so using the manipulator arm controls. The changes in the layer are attributed to polymerization and discussed further below.

4.3.4 Short lifetimes

Because of the instability of quaterthiophene under laser power, each dynamics scan had to be split into several sets of time steps (window sampling), and the laser was repositioned on the silver crystal after each set. The contour plots are shown as is, i.e., the data were not normalized for laser power fluctuations between sets (figure 4.3.4). Lifetimes are < 30 fs, and no intraband relaxation exists. The short lifetimes indicate that the barrier to decay back into the metal are negligible, and the decay occurs on a time scale greater than tens of femtoseconds. Further experiments are necessary to explore thickness-dependent lifetimes.

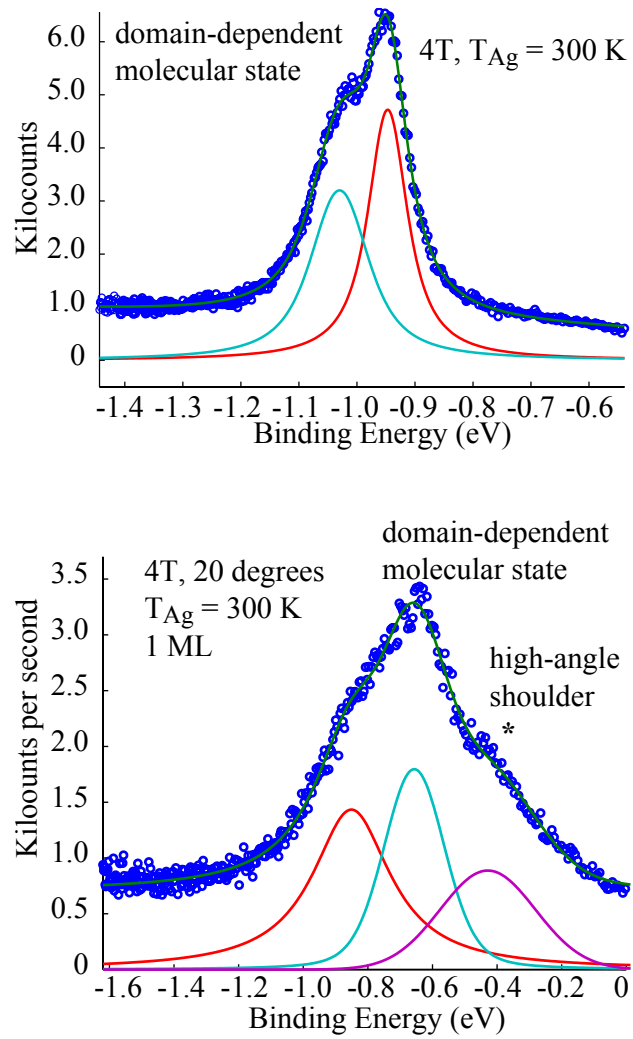


Figure 4.17: Fit of 2PPE spectrum at 0 degrees (top) and 20 degrees (bottom). The shoulder marked with (*) is consistently visible at high angles.

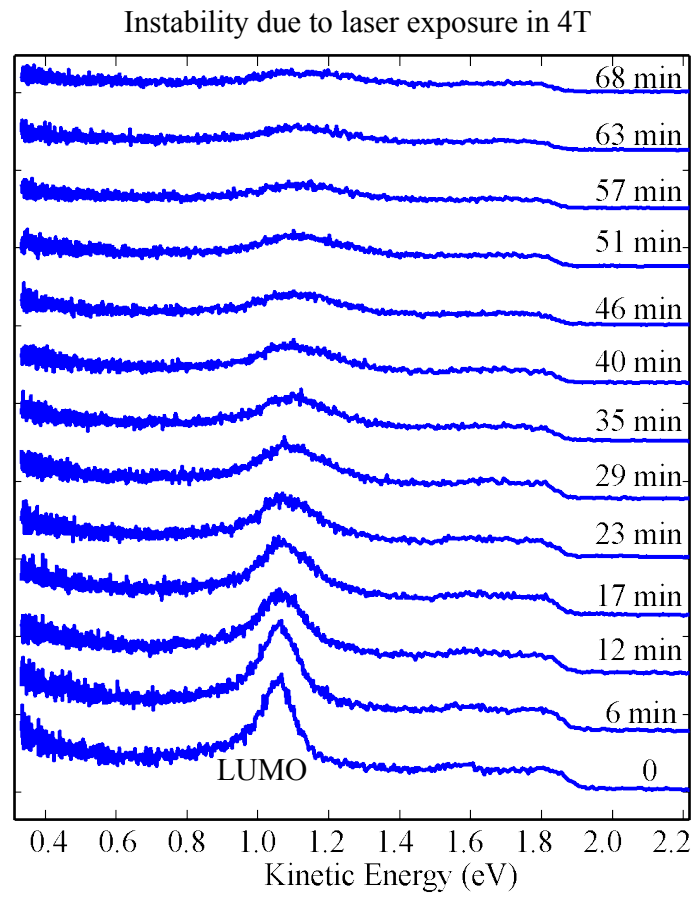


Figure 4.18: Over tens of minutes, exposure to laser light causes changes in the electronic structure of the layer.

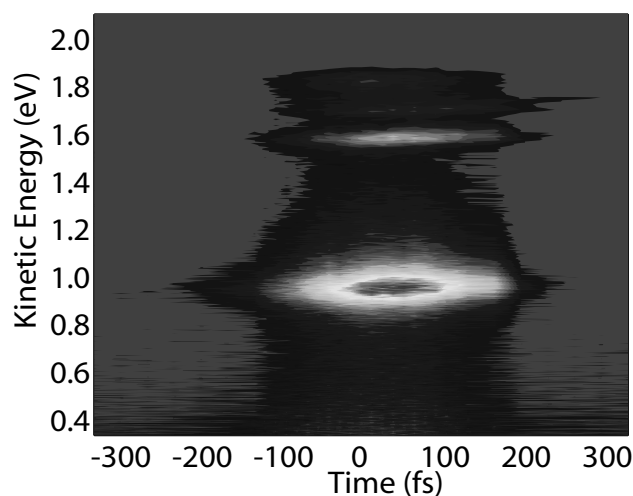


Figure 4.19: Contour plot of 1 ML quaterthiophene, at zero degrees.

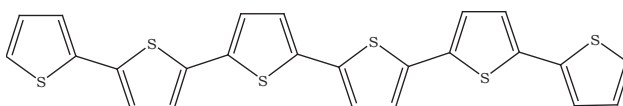


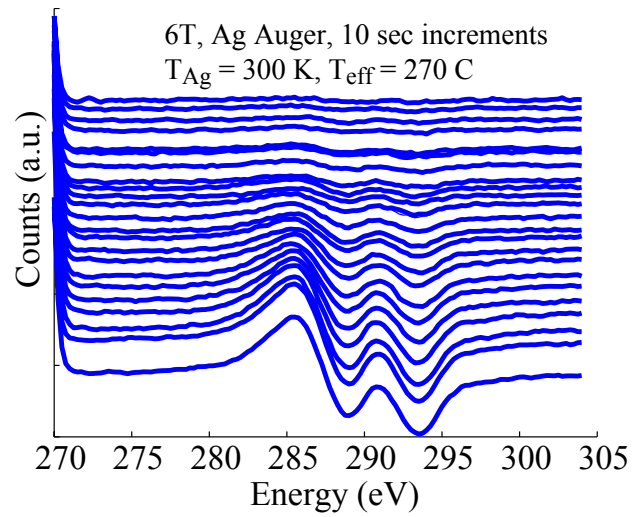
Figure 4.20: α -6T.

4.4 Sexithiophene

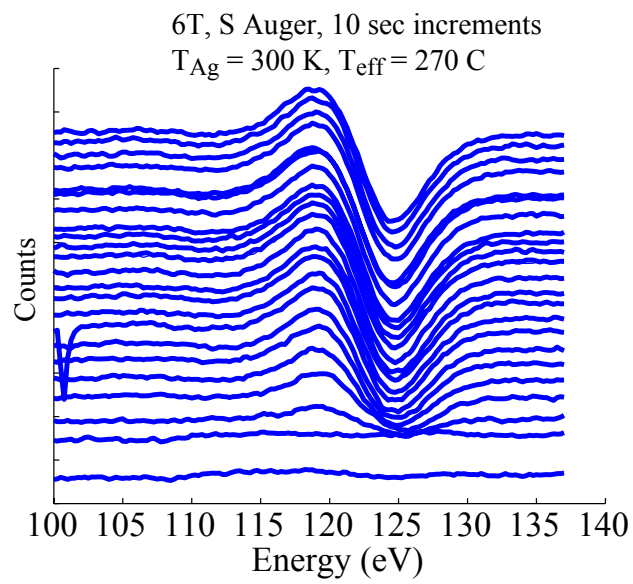
Chronologically, I studied sexithiophene before quaterthiophene. In retrospect, ambiguous results from sexithiophene data were due to laser-induced changes in the layer, which were much easier to see in quaterthiophene. Since sexithiophene is linear and already in its most thermodynamically stable state, the changes in the layers should not result from conformational changes as the molecule rotates around a barrier. Instead they are indicative of laser-induced polymerization. The similarity in 2PPE between quaterthiophene and sexithiophene exposed to laser light for a lengthy amount of time supports this argument.

4.4.1 Dosing survey

Sexithiophene was dosed at 260 °C, 270 °C and 280 °C. A dosing survey is presented in figure 4.22. The change in electronic structure after 40 – 50 seconds was possibly due



(a) Silver Auger



(b) Sulfur Auger

Figure 4.21: Auger peaks for Sulfur and Ag in a sexithiophene dosing survey with 10 second time steps, an effusion cell temperature of 270 °C, and at room temperature.

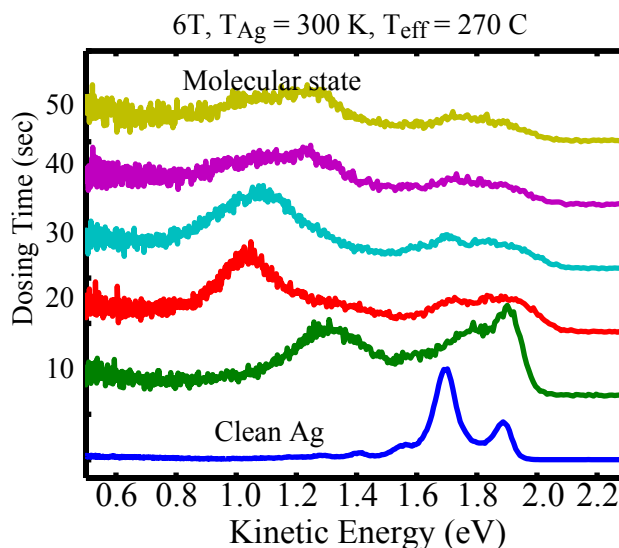


Figure 4.22: A dosing survey with 10 second increments; Ag crystal at 300 K; and effusion cell = 270 °C. The visible wavelength was 611 nm.

to laser-induced layer changes. Figure 4.23 overlays a 20-second layer with a 50-second layer, for which the 50-second layer was continuously exposed to the laser. The elapsed time between the two spectra was 12 minutes, which is similar to quaterthiophene data for layer changes. An Auger dosing survey corroborated my assignment of monolayer growth (figure 4.21). However, I noticed an increase in 2PPE signal when annealing at 380 K that did not correspond with any desorption via Auger when the layer was annealed to as high as 543 K. Campione et al. note homoepitaxial growth of α -6T using organic molecular beam epitaxy with islanding as a function of kinetic parameters; their growth temp is 563 K [111]. Horowitz reported the highest grain size in 6T at a substrate temp of 175 °C with a grain size = 330 nm; in this system, mobility was $0.28 \frac{\text{cm}^2}{\text{Vs}}$. In comparison, at room temperature the grain size was 60 nm and mobility was $0.11 \frac{\text{cm}^2}{\text{Vs}}$ [24].

4.4.2 LEED

LEED of the high temperature polymorph is presented in figure 4.24. After annealing to 500 K, no crystalline order exists. According to Horowitz et al., in the low temperature growth the sexithiophene lattice is in the monoclinic space group $P2_1/n$ with unit cell

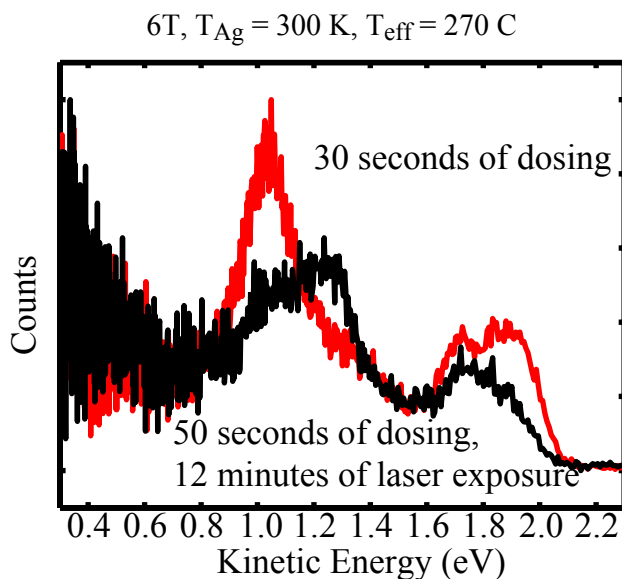


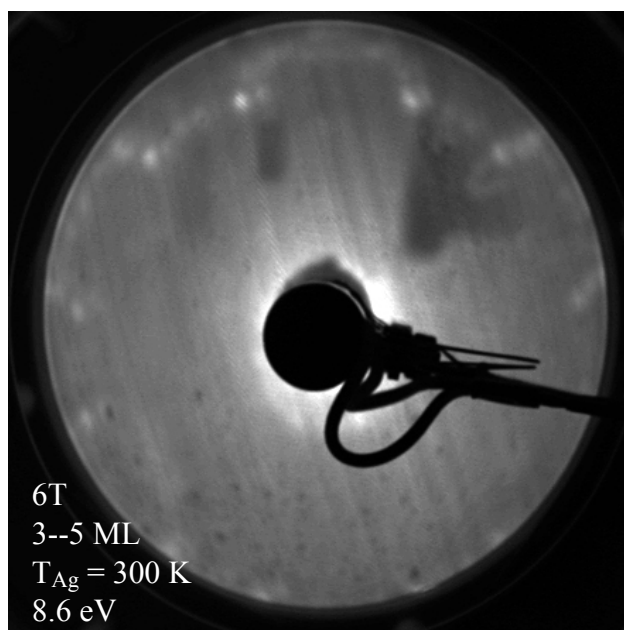
Figure 4.23: A comparison of the 20 second and 50 second films, where the elapsed time between the two was about 12 minutes.

parameters $a = 44.708\text{ \AA}$, $b = 7.841\text{ \AA}$, $c = 6.029\text{ \AA}$. $\beta = 90.76^\circ$, and, similar to other oligothiophenes' low temperature growth crystallinity, there are four molecules per unit cell in a herringbone geometry [112]. In the high temperature polymorph, the unit cell has two molecules and should still be crystalline. The source of the discrepancy is unclear.

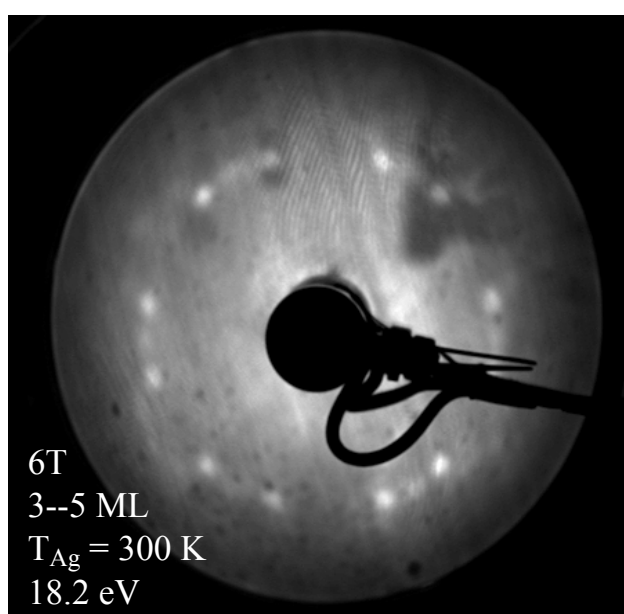
4.4.3 2PPE measurements

Sexithiophene is perhaps the most-studied of the oligothiophenes. It exhibits characteristics representative of oligothiophenes and of aromatic semiconductors. For example, Grobosch et al. have used XPS to measure a chemisorptive interaction between flat-lying sexithiophene and polycrystalline silver foils within the first monolayer. The dipole is -0.7 eV , determined by the shift in the vacuum level, and an electron injection barrier is given as 0.8 eV . Similar to PTCDA, an occupied interfacial state with binding energy of 1.4 eV below the Fermi level is measured [113]. With respect to spectral temperatures, it should be noted that the fine structure in photoluminescence studies disappears above 100 K , such that only a broad band with minimal peaks is observed [114].

A dispersion of bulk layers of sexithiophene, grown at an effusion cell temperature of



(a) 8.6 eV



(b) 18.2 eV

Figure 4.24: LEED of 3–5 ML sexithiophene, at 8.6 eV (top) and 18.2 eV (bottom).

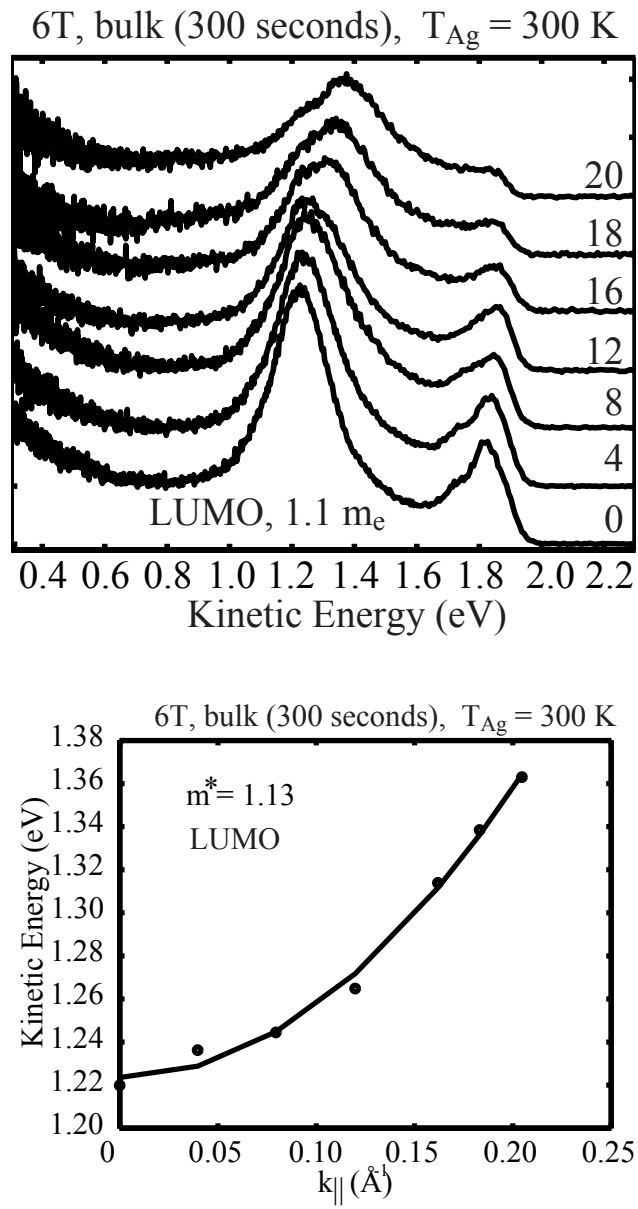


Figure 4.25: Dispersion of a bulk (300 second) layer, with a wavelength of 611 nm. The effective mass of the uv-probed peak is $1.1 m_e$.

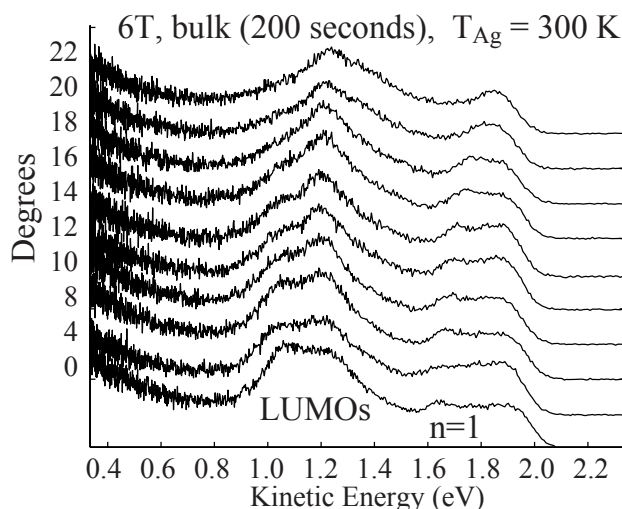
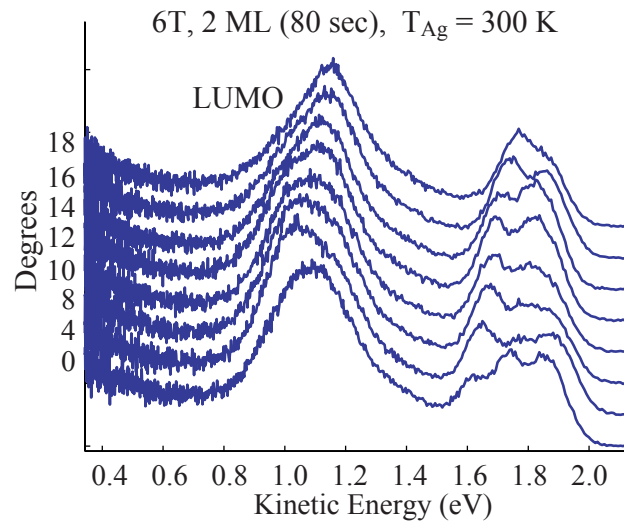


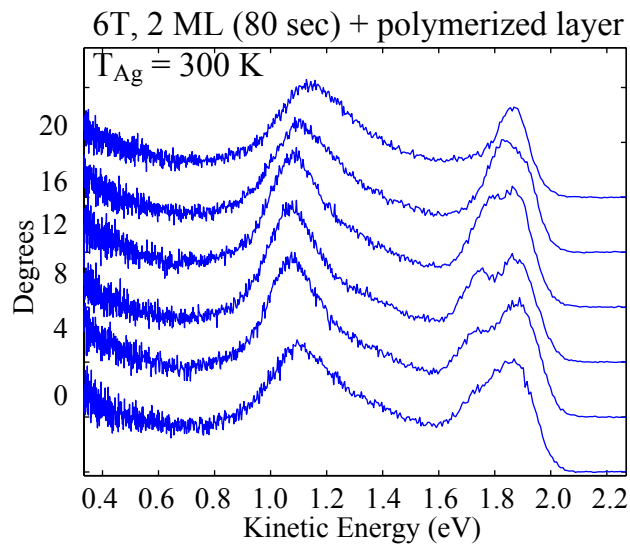
Figure 4.26: 200 seconds of 6T, with clear domain-separated energies.

270 °C, is presented in figure 4.25. The data look similar to ‘polymerized’ quaterthiophene data. Regardless, the effective mass of the peak at 1.2 eV kinetic energy is $1.1 m_e$. The peak has a binding energy of 2.82 eV, assuming that it is uv-probed, and referenced to the Fermi level its energy is 1.74 eV. The higher energy peak, at a kinetic energy of about 1.8 eV, is vis-probed and has a binding energy of 0.21 eV, which is 4.35 eV with respect to the Fermi level. The peak at 1.63 eV kinetic energy has an effective mass of $1.3 m_e$, and the lower energy polymorph peak has an effective mass of $1.1 m_e$ while the higher energy polymorph peak has an effective mass of $1.57 m_e$.

One-photon photoemission was visible at a photon energy of 4.2 eV. The 2PPE spectra are different for an effusion cell temperature at 260 °, although part of this difference may be due to reduced laser exposure. Part of the difference in spectra may be attributable to differences in the geometry at the interface; molecules lie flat in a submonolayer, and then start standing up with increased coverage on SiO_2 [115]. The transition dipole is along the long axis.



(a) 80sec6T



(b) 80sec6Tpolymer

Figure 4.27: Dispersion of 80 sec 6T (a), and of 80 sec 6T (b) grown on top of a polymerized surface.

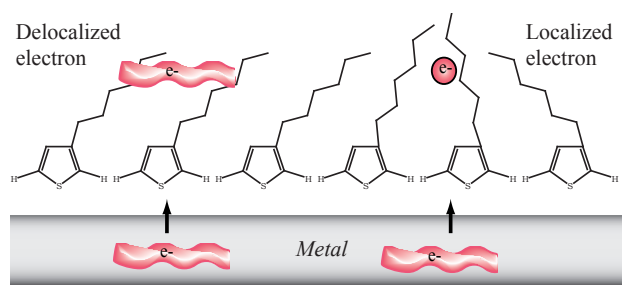


Figure 4.28: Observing static and dynamic localization due to side chains would be an interesting project.

4.5 Current status

4.5.1 Experimental difficulties

Certainly the laser-induced layer changes made these experiments unexpectedly more complicated. While I knew that polymerization occurred with electron-beam exposure or under x-ray illumination, I was caught by surprise to see the layer changes in uv energy ranges. Conversely, this may lead to new opportunities for studying time-resolved polymerization for different members of the thiophene family.

Bithiophene would be a welcome addition to the span between monothiophene and quaterthiophene. Unfortunately, bithiophene lies in the gap of vapor pressures too high for the effusion cell and too low for the sample line. Thiophenes have been functionalized to increase their solubility, so that they may be spin-coated as part of a device processing procedure. Studying interfaces of soluble, functionalized thiophenes is clearly relevant to technological uses of thiophenes, and doing so would entail specialized, liquid crucibles for our effusion cell, which have seen use already for ionic liquids. The possibility also exists that sulfur, which passivates many metals, has negative consequences for multi-channel plates and the LaB₆ LEED filament.

4.5.2 Trends and future work

The trend in increasing chain length is toward a smaller energy gap. The change in energy of the lowest energy molecular states – the LUMO states – seems to take place over

the first few oligomer lengths, since the energies are fairly similar for quaterthiophene and sexithiophene. This makes sense since octithiophene tends to replicate polymer behavior, in that by $n = 8$ the electronic properties of the polymer have been established. There appears to be both static localization and free-electron dispersions in quaterthiophene, which could be reproduced in sexithiophene if similar morphological control were exercised. By adding functional chains, observing static and dynamic localization may be possible, as dynamic localization has been observed already with 2PPE in alkyl groups on Ag(111) (figure 4.28). The increase in charge carrier might also lead to similar increases in device performance parameters.

Chapter 5

Conclusions

PTCDA spectra were found to have fundamentally different electronic behavior at the Ag(111) interface depending on morphology. Electron charge density transfer from the Ag(111) interface resulted in a semi-metallic state for crystalline layers, which also exhibited Stranski-Krastanov growth modes. Excited electrons in the semi-metallic LUMO+1 had effective masses less than a free electron mass and lifetimes less than 50 fs up to eight monolayers. For the crystalline morphology, the presence of image states despite the amount of PTCDA on the surface indicated that the wetting layer has a real and dominant effect on electronic behavior. Amorphous layers, which grew in layer-by-layer fashion, created trap sites that caused electron decay times to increase exponentially. The distribution of geometries and aggregates in an amorphous layer led to inhomogeneous distributions of energy and increased image potential state effective masses.

2PPE measurements were tied to charge mobility through estimates of carrier relaxation times from Lorentzian linewidths. The rectangular lattice of PTCDA also enabled a value for the transfer integral to be calculated, with energies on the same order of magnitude as other n-type, crystalline, and organic semiconductors such as C_{60} . While my original intent was to study a pure device interface, absent of anything unique like the semi-metallic LUMO+1, the existence of a surface-specific electronic state has only driven home that studying the fundamental science of molecules with technological applications can lead to new discoveries interesting in their own right.

My study of thiophenes is still ongoing, and will hopefully survive my graduation

from the Harris group. I have accomplished as much as I could reasonably ask for on this project, and I strongly believe in the vast amount of new and interesting research that this project can generate. Thiophenes and their derivatives will be a solid multi-year project for whomever continues it. Looking at oligomers with no functional groups, to finish the first phase of thiophene oligomers, I would like to focus on domain-dependent info for quaterthiophene and possibly sexithiophene. Extracting a localization size could link charge transport measured with 2PPE to charge localization measurements that place charges on individual oligomers until $n = 8$ or so.

Since thiophenes can lie flat on the surface or stick up along the surface normal, identifying exciton states by making transition dipole arguments could be an interesting application of 2PPE. Judging from monothiophene and quaterthiophene layer-dependent spectra, not much more data would be required to accomplish this. Looking at monothiophene bulk coverages would also fill out a missing picture of whether the spectra visible in planar monothiophene is due to surface interactions, or to the planar geometry. Further in the future, functionalized thiophenes and heterogeneous films will be an interesting avenue of research, and it appears that the Harris group will follow this path.

My research project began as a foray into device interfaces to understand surface chemistry and physics, and their putative relationship to relevant parameters for charge transport and charge injection. Having devoted my dissertation to these systems, I remain convinced that 2PPE is a useful tool in investigating electronic behavior in ultrathin films. The caveat, however, is that the choice of system matters significantly. The Achilles' heel of these experiments is surface characterization, and therefore model systems prevalent in the literature are the best candidates for 2PPE experiments. The future is promising for continued 2PPE studies of organic semiconductor materials, and I hope that at least some of this dissertation will prove to be helpful to anyone follows this line of research.

Bibliography

- [1] H. E. Landsberg. Man-made climatic changes. *Science*, 170:1265, 1970.
- [2] S. Schneider and S. Rasool. Atmospheric carbon dioxide and aerosols: Effects of large increases on global climate. *Science*, 173:138, 1971.
- [3] A. P. Alivisatos. Semiconductor clusters, nanocrystals, and quantum dots. *Science*, 271:933, 1996.
- [4] X.Y. Zhu. Electronic structure and electron dynamics at molecule-metal interfaces: implications for molecule-based electronics. *Surface Science Reports*, 56(1):1, 2004.
- [5] P. Szymanski, S. Garrett-Roe, and C.B. Harris. Time- and angle-resolved two-photon photoemission studies of electron localization and solvation at interfaces. *Progress in Surface Science*, 78(1):1, 2005.
- [6] J.D. McNeill, R.L. Lingle, N.H. Ge, C.M. Wong, R.E. Jordan, and C.B. Harris. Dynamics and spatial distribution of electrons in quantum wells at interfaces determined by femtosecond photoemission spectroscopy. *Physical Review Letters*, 29(23):4645, 1997.
- [7] N.H. Ge, C.M. Wong, R.L. Lingle Jr., J.D. McNeill, K.J. Gaffney, and C.B. Harris. Femtosecond dynamics of electron localization at interfaces. *Science*, 279(5348):202, 1998.
- [8] H. Petek, M.J. Weida, H. Nagano, and S. Ogawa. Real-time observation of adsorbate atom motion above a metal surface. *Science*, 288:1402, 2000.

- [9] S. Garrett-Roe, S. Shipman, P. Szymanski, M. Strader, A. Yang, and C.B. Harris. Ultrafast electron dynamics at metal interfaces: Interband relaxation of image state electrons as friction. *Journal of Physical Chemistry B*, 109:20370, 2005.
- [10] K.J. Gaffney, C.M. Wong, S.H. Liu, A.D. Miller, J.D. McNeill, and C.B. Harris. Femtosecond electron dynamics at the benzene/ag(111) interface. *Chemical Physics*, 251(1):99, 2000.
- [11] J.D. McNeill, Jr. R. L. Lingle, R. E. Jordan, D. F. Padowitz, and C. B. Harris. Interfacial quantum well states of xe and kr adsorbed on ag(111). *Journal of Chemical Physics*, 105(9):3883, 1996.
- [12] K. J. Gaffney, A.D. Miller, S.H. Liu, and C.B. Harris. Femtosecond dynamics of electrons photoinjected into organic semiconductors at aromatic-metal interfaces. *Journal of Physical Chemistry B*, 105:9031, 2001.
- [13] A. D. Miller, K. J. Gaffney, S. H. Liu, P. Szymanski, S. Garrett-Roe, C. M. Wong, and C. B. Harris. Evolution of a two-dimensional band structure at a self-assembling interface. *Journal of Physical Chemistry A*, 106:7636, 2002.
- [14] G. Dutton and X.Y. Zhu. Distance-dependent electronic coupling at molecule-metal interfaces: C-60/cu(111). *Journal of Physical Chemistry B*, 108(23), 2004.
- [15] S. Shipman, S. Garrett-Roe, P. Szymanski, A. Yang, M. Strader, and C.B. Harris. Determination of band curvatures by angle-resolved two-photon photoemission in thin films of C₆₀ on Ag(111). *Journal of Physical Chemistry B*, 110, 2006.
- [16] T. Fauster and W. Steinmann. Two-photon photoemission spectroscopy of image states. In P. Halevi, editor, *Photonic probes of surfaces*, volume 2 of *Electromagnetic waves*. Elsevier, 1995.
- [17] C.B. Harris, N.-H. Ge, R.L. Lingle Jr., J.D. McNeill, and C.M. Wong. Femtosecond dynamics of electrons on surfaces and at interfaces. *Annual Review of Physical Chemistry*, 48:711, 1997.

- [18] I.G. Hill, A. Kahn, Z.G. Soos, and R.A. Pascal Jr. Charge-separation energy in films of π -conjugated organic molecules. *Chemical Physics Letters*, 327:181, 2000.
- [19] M. Pope. *Electronic Processes in Organic Crystals*. Oxford University Press, New York, 1982.
- [20] J. Stähler, M. Mehlhorn, U. Bovensiepen, M. Meyer, D. O. Kusmirek, K. Morganstern, and M. Wolf. Impact of ice structure on ultrafast electron dynamics in d₂O clusters on cu(111). *PRL*, 98(206105), 2007.
- [21] J. Campbell Scott. Metal-organic interface and charge injection in organic electronic devices. *J. Vac. Sci. Technol. A*, 21(3), 2003.
- [22] A. Dodabalapur, L. Torsi, and H.E. Katz. Organic transistors: Two-dimensional transport and improved electrical characteristics. *Science*, 268:270, 1995.
- [23] J. Locklin, M. E. Roberts, S. Mannsfeld, and Z. Bao. Optimizing the thin film morphology of organic field-effect transistors: The influence of molecular structure and vacuum deposition parameters on device performance. *Polymer Reviews*, 46:79, 2006.
- [24] G. Horowitz and M. Hajlaoui. Mobility in polycrystalline oligothiophene field-effect transistors dependent on grain size. *Advanced Materials*, 12:1046, 2000.
- [25] D. Knipp, R. A. Street, A. Völkel, and J. Ho. Pentacene thin film transistors on inorganic dielectrics: Morphology, structural properties, and electronic transport. *Journal of Applied Physics*, 93(1), 2003.
- [26] T. N. Ng, W. R. Silveira, and J. A. Marohn. Dependence of charge injection on temperature, electric field, and energetic disorder in an organic semiconductor. *Physical Review Letters*, 98(066101), 2007.
- [27] P. Avouris and I. Lyo. Observation of quantum-size effects at room temperature on metal surfaces with stm. *Science*, 264:942, 1994.

- [28] J. Li, W.-D. Schneider, R. Brendt, and S. Crampin. Electron Confinement to Nanoscale Ag Islands on Ag(111): A Quantitative Study. *Physical Review Letters*, 80(15), 1998.
- [29] J. Huang and M. Kertesz. Electronic structures and charge transport properties of the organic semiconductor bis[1,2,5]thiadiazolo-p-quinobis(1,3-dithiole), btqbt, and its derivatives. *Journal of Physical Chemistry B*, 109:12891, 2005.
- [30] Jr. W. R. Merry. *Image Potential States at Metal-Dielectric Interfaces*. PhD thesis, University of California, Berkeley, 1992.
- [31] W.R. Merry, R.E. Jordan, D.F. Padowitz, and C.B. Harris. Electrons at metal-insulator interfaces. I. The effect of Xe monolayers on the image potential states of Ag(111). *Surface Science*, 295:393, 1993.
- [32] H. Petek and S. Ogawa. Femtosecond time-resolved two-photon photoemission studies of electron dynamics in metals. *Progress in Surface Science*, 56(4):239, 1997.
- [33] S. Garrett-Roe. *Ultrafast Electron Dynamics at Dielectric/Metal Interfaces: Intra-band Relaxation of Image Potential State Electrons as Friction and Disorder Induced Electron Localization*. PhD thesis, University of California, Berkeley, 2005.
- [34] J. McNeill. *Ultrafast Dynamics of Electrons at Interfaces*. PhD thesis, University of California, Berkeley, 1999.
- [35] <http://outgassing.nasa.gov>.
- [36] R.L. Lingle, N.H. Ge, R.E. Jordan, J.D. McNeill, and C.B. Harris. Femtosecond studies of electron tunneling at metal-dielectric interfaces. *Chemical Physics*, 208:297, 1996.
- [37] S.R. Forrest. Ultrathin organic films grown by organic molecular beam deposition and related techniques. *Chemical Reviews*, 97(6):1793, 1997.

- [38] F.F. So, S.R. Forrest, Y.Q. Shi, and W.H. Steier. Quasi-epitaxial growth of organic multiple quantum well structures by organic molecular beam deposition. *Applied Physics Letters*, 56(7):674, 1999.
- [39] S.R. Forrest, P.E. Burrows, E.I. Haskal, and F.F. So. Ultrahigh-vacuum quasiepitaxial growth of model van der waals thin films. ii. experiment. *Physical Review B*, 49(16), 1994.
- [40] B. Krause, A.C. Dürr, K. Ritley, F. Schreiber, H. Dosch, and D. Smilgies. Structure and growth morphology of an archetypal system for organic epitaxy: PTCDA on Ag(111). *Physical Review B*, 66(235404), 2002.
- [41] F.S. Tautz, M. Eremtchenko, J.A. Schaefer, M. Sokolowski, V. Shklover, K. Glöckler, and E. Umbach. A comparison of the chemisorption behaviour of PTCDA on different Ag surfaces. *Surface Science*, 502:176, 2002.
- [42] K. Glöckler, C. Seidel, A. Soukopp, M. Sokolowski, E. Umbach, M. Bohringer, R. Berndt, and W.D. Schneider. Highly ordered structures and submolecular scanning tunnelling microscopy contrast of ptcda and dm-pbdci monolayers on ag(111) and ag(110). *Surface Science*, 405:1, 1998.
- [43] L. Kilian, E. Umbach, and M. Sokolowski. Molecular beam epitaxy of organic films investigated by high resolution low energy electron diffraction (SPA-LEED): 3,4,9,10-perylenetetracarboxylic acid-dianhydride (PTCDA) on Ag(111). *Surface Science*, 573:359, 2004.
- [44] M. Hoffmann, K. Schmidt, T. Fritz, T. Hasche, V.M. Agranovich, and K. Leo. The lowest energy Frenkel and charge-transfer excitons in quasi-one-dimensional structures: application to MePTCDI and PTCDA crystals. *Chemical Physics*, 258:73, 2000.
- [45] H. Proehl, T. Dienel, R. Nitsche, and T. Fritz. Formation of solid-state excitations in ultrathin crystalline films of PTCDA: from single molecules to molecular stacks. *Physical Review Letters*, 93(9), 2004.

- [46] U. Gomez, M. Leonhardt, H. Port, and H.C. Wolf. Optical properties of amorphous ultrathin films of perylene derivatives. *Chemical Physics Letters*, 268:1, 1997.
- [47] W. Gebauer, A. Langner, M. Schneider, M. Sokolowski, , and E. Umbach. Exciton dispersion in a p-conjugated oligomer film: a-quaterthiophene on highly oriented pyrolytic graphite and ag(111). *Physical Review B*, 69(125420), 2004.
- [48] J.R. Ostrick, A. Dodabalapur, L. Torsi, A.J. Lovinger, E.W. Kwock, T.M. Miller, M. Galvin, M. Berggren, and H.E. Katz. Conductivity-type anisotropy in molecular solids. *Journal of Applied Physics*, 81(10):6804, 1997.
- [49] H. Yamane, S. Kera, K. Okudaira, D. Yoshimura, K. Seki, and N. Ueno. Intermolecular energy-band dispersion in ptcda multilayers. *Physical Review B*, 68(033102), 2003.
- [50] M.I. Alonso, M. Garriga, N. Karl, J.O. Ossò, and F. Schreiber. Anisotropic optical properties of single crystalline ptcda studied by spectroscopic ellipsometry. *Organic electronics*, 3:23, 2002.
- [51] F.S. Tautz, M. Eremtchenko, J.A. Schaefer, M.Sokolowski, V. Shklover, and E. Umbach. Strong electron-phonon coupling at a metal/organic interface: Ptcda/ag(111). *Physical Review B*, 65(125405), 2002.
- [52] R. Temirov, S. Soubatch, A. Luican, and F. S. Tautz. Free-electron-like dispersion in an organic monolayer film on a metal substrate. *Nature*, 444:350, 2006.
- [53] Y. Hirose, A. Kahn, V. Aristov, P. Soukiassian, V. Bulovic, and S.R. Forrest. Chemistry and electronic properties of metal-organic semiconductor interfaces: Al, ti, in, sn, ag, and au on PTCDA. *Physical Review B*, 54(19):13748, 1996.
- [54] M. Eremtchenko, J.A. Schaefer, and F.S. Tautz. Understanding and tuning the epitaxy of large aromatic adsorbates by molecular design. *Nature*, 425(6598):602, 2003.

- [55] A. Hauschild, K. Karki, B.C.C. Cowie, M. Rohlfing, F.S. Tautz, , and M. Sokolowski. Molecular distortions and chemical bonding of a large π -conjugated molecule on a metal surface. *Physical Review Letters*, 94(036106), 2005.
- [56] A. Hauschild, K. Karki, B.C.C. Cowie, M. Rohlfing, F.S. Tautz, , and M. Sokolowski. Comment on “molecular distortions and chemical bonding of a large pi-conjugated molecule on a metal surface” - reply. *Physical Review Letters*, 95(209602), 2005.
- [57] T.U. Kampen, G. Gavrilă, H. Mendez, D.R.T. Zahn, A.R. Veary-Roberts, D.A. Evans, J. Wells, I. McGovern, and W. Braun. Electronic properties of interfaces between perylene derivatives and gaas(001) surfaces. *Journal of Physics-Condensed Matter*, 15(38):2679, 2003.
- [58] B. Krause, F. Schreiber, H. Dosch, A. Pimpinelli, and O.H. Seeck. Temperature dependence of the 2d-3d transition in the growth of ptcda on ag(111): A real-time X-ray and kinetic monte carlo study. *Europhysics Letters*, 65:372, 2004.
- [59] T. Soubiron, F. Vaurette, J.P. Nys, B. Brandidier, X. Wallart, and D. Stiévenard. Molecular interactions of ptcda on si(100). *Surface Science*, 581:178, 2005.
- [60] A.J. Ferguson and T.S. Jones. Photophysics of ptcda and me-ptcdi thin films: Effects of growth temperature. *Journal of Physical Chemistry B*, 110:6891, 2006.
- [61] A. Yang, S.T. Shipman, S. Garrett-Roe, J. Johns, M. Strader, P. Szymanski, E. Muller, and C.B. Harris. Two-photon photoemission of ultrathin film ptcda morphologies on ag(111). *Journal of Physical Chemistry C*, 112:2506, 2008.
- [62] I.G. Hill, A. Rajagopal, A. Kahn, and Y. Hu. Molecular level alignment at organic semiconductor-metal interfaces. *Applied Physics Letters*, 73(5):662, 1998.
- [63] H. Vázquez, R. Oszwaldowski, P. Pou, J. Ortega, R. Pérez, F. Flores, and A. Kahn. Dipole formation at metal/PTCDA interfaces: Role of the charge neutrality level. *Europhysics Letters*, 65:802, 2004.

- [64] A. Kraft, R. Temirov, S.K.M. Henze, S. Soubatch, M. Rohlfing, and F.S. Tautz. Lateral adsorption geometry and site-specific electronic structure of a large organic chemisorbate on a metal surface. *Physical Review B*, 74(041402), 2006.
- [65] V. Bulović, P.E. Burrows, S.R. Forrest, J.A. Cronin, and M.E. Thompson. Study of localized and extended excitons in 3,4,9,10-perylenetetracarboxylic acid dianhydride (PTCDA) I. Spectroscopic properties of thin films and solutions. *Chemical Physics*, 210:1, 1996.
- [66] D. Ino, K. Watanabe, N. Takagi, and Y. Matsumoto. Ultrafast excited state dynamics in 3,4,9,10-perylene tetracarboxylic dianhydride (ptcda) thin films. *Chemical Physics Letters*, 383:261, 2004.
- [67] C. P. Lindsey and G. D. Patterson. Detailed comparison of the williams-watts and cole-davidson functions. *Journal of Chemical Physics*, 73(7):3348, 1980.
- [68] E. Engel, M. Koschorreck, K. Leo, and M. Hoffman. Excitonic intraband relaxation and polarization anisotropies in ptcda on femtosecond and picosecond timescales. *Journal of Luminescence*, 112:299, 2005.
- [69] S. Hasegawa, T. Mori, K. Imaeda, S. Tanaka, Y. Yamashita, H. Inokuchi, H. Fujimoto, K. Seki, and N. Ueno. Intermolecular energy-band dispersion in oriented thin films of bis(1,2,5-thiadiazolo)-p-quinobis(1,3-dithiole) by angle-resolved photoemission. *Journal of Chemical Physics*, 100(9):6969, 1994.
- [70] N. Koch, A. Vollmer, I. Salzmann, B. Nickel, H. Weiss, and J. P. Rabe. Evidence for temperature-dependent electron band dispersion in pentacene. *Physical Review Letters*, 96(156803), 2006.
- [71] E.V. Chulkov, A.G. Borisov, and J.P. Gauyacq. Electronic excitations in metals and at metal surfaces. *Chemical Reviews*, 106, 2006.
- [72] A. D. Miller, I. Bezel, K. J. Gaffney, S. Garrett-Roe, S. H. Liu, P. Szymanski, and C. B. Harris. Electron solvation in two dimensions. *Science*, 297(5584):1163, 2002.

- [73] C. Gahl, U. Bovensiepen, C. Frischkorn, and M. Wolf. Ultrafast dynamics of electron localization and solvation in ice layers on cu(111). *Physical Review Letters*, 89(107402), 2002.
- [74] G. Horowitz. Organic field-effect transistors. *Advanced Materials*, 10:365, 1998.
- [75] G. Horowitz, F. Garnier, A. Yassar, R. Hajlaoui, and F. Kouki. Field-effect transistor made with a sexithiophene single crystal. *Advanced Materials*, 8:52, 1996.
- [76] F. Garnier, R. Hajlaoui, A. Yassar, and P. Srivastata. All-polymer field-effect transistor realized by printing techniques. *Science*, 265:1684, 265.
- [77] A. Facchetti, Y. Deng, A. Wang, Y. Koide, H. Sirringhaus, T. Marks, and R. Friend. Tuning the semiconducting properties of sexithiophene by alpha, omega-substitution – alpha, omega-diperfluorohexylsexithiophene: The first n-type sexithiophene for thin-film transistors. *Angewandte Chemie-International Edition*, 39:4547, 2000.
- [78] D. Fichou. Structural order in conjugated oligothiophenes and its implications on opto-electronic devices. *Journal of Materials Chemistry*, 10:571, 2000.
- [79] M. Surin, P. Leclère, S. De Feyter, M. Abdel-Mottaleb, F. De Schryber, O. Henze, W. James Feast, and R. Lazzaroni. Molecule-molecule versus molecule-substrate interactions in the assembly of oligothiophenes at surfaces. *Journal of Physical Chemistry B*, 110:7898, 2006.
- [80] X. Yang, J. Loos, S.C. Veenstra, W. Verhees, M. Wienk, J. Kroon, M. Michels, and R. Janssen. Nanoscale morphology of high-performance polymer solar cells. *Nano Letters*, 5(4):579, 2005.
- [81] A. Saeki, S. Seki, Y. Koizumi, T. Sunagawa, K. Ushida, and S. Tagawa. Increase in the mobility of photogenerated positive charge carriers in polythiophene. *Journal of Physical chemistry B*, 109:10015, 2005.
- [82] W. Huynh, J. Dittmer, and A. P. Alivisatos. Hybrid nanorod-polymer solar cells. *Science*, 295(5564):2425, 2002.

- [83] F. Dinelli, M. Murgia, P. Levy, M. Cavallini, and F. Biscarini. "spatially correlated charge transport in organic thin film transistors". *Physical Review Letters*, 92(11), 2004.
- [84] G. Horowitz, X.-Z. Peng, D. Fichou, and F. Garnier. Role of the semiconductor/insulator interface in the characteristics of π -conjugated-oligomer-based thin-film transistors. *Synthetic Metals*, 51:419, 1992.
- [85] L. Antolini, G. Horowitz, F. Kouki, and F. Garnier. Polymorphism in oligothiophenes with an even number of thiophene subunits. *Advanced Materials*, 10(5):382, 1998.
- [86] S. Duhm, G. Heimel, I. Salzmann, H. Glowatzki, R. Johnson, A. Vollmer, J. Rabe, and N. Koch. Orientation-dependent ionization energies and interface dipoles in ordered molecular assemblies. *Nature Materials*, 7:326, 2008.
- [87] S. Rentsch, J.P. Yang, W. Paa, E. Birckner, J. Schiedt, and R. Weinkauff. Size dependence of triplet and singlet states of α -oligothiophenes. *Physical Chemistry Chemistry Physics*, 1:1707, 1999.
- [88] D. Fichou, G. Horowitz, B. Xu, and F. Garnier. Low temperature optical absorption of polycrystalline thin films of α -quaterthiophene, α -sexithiophene and α -octithiophene, three model oligomers of polythiophene. *Synthetic Metals*, 48:167, 1992.
- [89] M. Knupfer, T. Pichler, M.S. Golden, J. Fink, M. Murgia, R.H. Michel, R. Zamboni, and C. Taliani. Size of electron-hole pairs in π -conjugated systems. *Physical Review Letters*, 83(7):1443, 1999.
- [90] A. Heeger. Solitons in conducting polymers. *Reviews of Modern Physics*, 60:781, 1988.
- [91] H.E. Katz and Z. Bao. The physical chemistry of organic field-effect transistors. *Journal of Physical Chemistry B*, 104:671, 2000.

- [92] A. Troisi and G. Orlandi. Dynamics of the intermolecular transfer integral in crystalline organic semiconductors. *Journal of Physical Chemistry A*, 110:4065, 2006.
- [93] G.S. Kanner, X. Wei, B.C. Hess, L.R. Chen, and Z.V. Vardeny. Evolution of excitons and polarons in polythiophene from femtoseconds to milliseconds. *Physical Review Letters*, 69(3):538, 1992.
- [94] J.P. Yang, W. Paa, and S. Rentsch. Size dependent ultrafast dynamics of oligothiophenes with 1 –4 monomer units. *Synthetic Metals*, 101:624, 1999.
- [95] G. Lanzani, S.V. Frolov, P.a. Lane, Z.V. Vardeny, M. Nisoli, and S. De Silvestri. Transient spectroscopy of frenkel and charge transfer excitons in α -sexithienyl films. *Physical Review letters*, 79(16):3066, 1997.
- [96] G. Juška, K. Arlauskas, M. Viliūnas, K. Genevičius, R. Österbacka, and H. Stubb. Charge transport in π -conjugated polymers from extraction current transients. *Physical Review B*, 62(24), 2000.
- [97] P. Väterlein, M. Schmelzer, J. Taborski, T. Krause, F. Viczian, M. Bassler, R. Fink, E. Umbach, and W. Wurth. Orientation and bonding of thiophene and 2,2'-bithiophene on Ag(111): a combined near edge extended X-ray absorption fine structure and X alpha scattered-wave study. *Surface Science*, 452:20, 2000.
- [98] J. Stöhr, J. Gland, E. Kollin, R.J. Koestner, A. Johnson, E. Muettertities, and F. Sette. Desulfurization and structural transformation of thiophene on the pt(111) surface. *Physical Review Letters*, 53(22):2161, 1984.
- [99] K.M. Baumgärtner, M. Volmer-Uebing, J. Taborski, P. Bäuerle, and E. Umbach. Adsorption and polymerization of thiophene on a Ag(111) surface. *Berichte der Bunsen-gesellschaft-physical chemistry chemical physics*, 95:1488, 1991.
- [100] X. Chen, E.R. Frank, and R.J. Hamers. Spatially and rotationally oriented adsorption of molecular adsorbates on ag(111) investigated using cryogenic scanning tunneling microscopy. *Journal of Vacuum Science and Technology B*, 14:1136, 1996.

- [101] M. Palmer, I. Walker, and M. Guest. The electronic states of thiophene studied by optical (vuv) absorption, near-threshold electron energy-loss (eel) spectroscopy and ab initio multi-reference configuration interaction calculations. *Chemical Physics*, 241:275, 1999.
- [102] S. Millefiori, A. Alparone, and A. Millefiori. Conformation properties of thiophene oligomers. *Journal of Heterocyclic Chemistry*, 37, 2000.
- [103] T. Siegrist, C. Kloc, R. Laudise, H. Katz, and R. Haddon. Crystal growth, structure, and electronic band structure of α -4t polymorphs. *Advanced Materials*, 10(5):379, 1998.
- [104] A. Soukopp, C. Seidel, R. Li, M. Btissler, M. Sokolowski, and E. Umbach. Highly-ordered ultrathin films of quaterthiophene on a ag(111) surface. *Thin Solid Films*, 284–285:343, 1996.
- [105] R. Li, Bäuerle, and E. Umbach. Vibrational and geometric structure of quaterthiophene on ag(111). *Surface Science*, 331–335:100, 1995.
- [106] A. Sassella, M. Campione, A. Papagni, C. Goletti, G. Bussetti, P. Chiaradia, V. Marcon, and G. Raos. Strategies for two-dimensional growth of organic molecular films. *Chemical Physics*, 325:193, 2006.
- [107] C. Seidel, A. Soukopp, R. Li, P. Bäuerle, and E. Umbach. Long-range ordered, commensurate superstructures of large organic adsorbates: a leed and stm study of ec4t/ag(111). *Surface Science*, 374:17, 1997.
- [108] H.-J. Egelhaaf, D. Oelkrug, D. Oeter, Ch. ziegler, and W. Göpel. HREELS and UV/VIS spectroscopic studies on the electronic structure of oligothiophene thin films. *Journal of Molecular Structure*, 348:405, 1995.
- [109] A. Sassella, A. Borghesi, R. Tubino, S. Destri, W. Porzio, and G. Barbarella. Quasi-epitaxial growth of quaterthiophene thin films by organic molecular beam deposition. *Synthetic Metals*, 115, 2000.

- [110] A. Sassella, A. Borghesi, F. Meinardi, D. Riva, S. Tavazzi, R. Tubino, W. Porzio, S. Destri, G. Barbarella, and F. Garnier. Optical properties of thin films of oligothiophenes deposited by organic molecular beam deposition. *Synthetic Metals*, 116:213, 2001.
- [111] M. Campione, S. Caprioli, M. Moret, and A. Sassella. Homoepitaxial growth of α -hexathiophene. *Journal of Physical Chemistry C*, 111:12741, 2007.
- [112] G. Horowitz, B. Bachet, A. Yassar, P. Lang, F. Demanze, J.-L. Fave, and F. Garnier. Growth and characterization of sexithiophene single-crystals. *Chemistry of Materials*, 7:1337, 1995.
- [113] M. Grobosch and M. Knupfer. Energy level alignment and interface states at α -sexithiophene/ag interfaces. *Organic Electronics*, 8:625, 2007.
- [114] M. A. Loi, A. Mura, G. Bongiovanni, Q. Cai, C. Martin, H. R. Chandrasekhar, M. Chandrasekhar, W. Graupner, and F. Garnier. Ultrafast formation of nonemissive species via intermolecular interaction in single crystals of conjugated molecules. *Physical Review Letters*, 86:732, 2001.
- [115] M. Loi, E. Da Como, F. Dinelli, M. Murgia, R. Zamboni, F. Biscarini, and M. Mucini. Supramolecular organization in ultra-thin films of α -sexithiophene on silicon dioxide. *Nature Materials*, 4:81, 2005.